Pulse-resolved radiotherapy dosimetry using fiber-coupled organic scintillators

Beierholm, Anders Ravnsborg

Publication date:
2011

Document Version
Publisher's PDF, also known as Version of record

Citation (APA):
Beierholm, A. R. (2011). Pulse-resolved radiotherapy dosimetry using fiber-coupled organic scintillators. Roskilde: Danmarks Tekniske Universitet, Risø Nationallaboratoriet for Bæredygtig Energi. (Risø-PhD; No. 85(EN)).

Pulse-resolved radiotherapy dosimetry using fiber-coupled organic scintillators

Risø-PhD-Report

Anders Ravnsborg Beierholm
Risø-PhD-85 (EN)
May 2011

Risø DTU
National Laboratory for Sustainable Energy

Author: Anders Ravnsborg Beierholm

Title: Pulse-resolved radiotherapy dosimetry using fiber-coupled organic scintillators

Division: Radiation Research Division

Abstract:

This PhD project pertains to the development and adaptation of a dosimetry system that can be used to verify the delivery of radiation in modern radiotherapy modalities involving small radiation fields and dynamic radiation delivery.

The dosimetry system is based on fibre-coupled organic scintillators and can be perceived as a well characterized, independent alternative to the methods that are in clinical use today. The dosimeter itself does not require a voltage supply, and is composed of water equivalent materials. The dosimeter can be fabricated with a sensitive volume smaller than a cubic millimeter, which is small enough to resolve the small radiation fields encountered in modern radiotherapy. The fast readout of the dosimeter enables measurements on the same time scale as the pulsed radiation delivery from the medical linear accelerators used for treatment.

The dosimetry system, comprising fiber-coupled organic scintillators and data acquisition hardware, was developed at the Radiation Research Division at Risø DTU and tested using clinical x-ray beams at hospitals in Denmark and abroad.

Measurements of output factors and percentage depth dose were performed and compared with reference values and Monte Carlo simulations for static square radiation fields for standard (4 cm x 4 cm to 20 cm x 20 cm) and small (down to 0.6 cm x 0.6 cm) field sizes. The accuracy of most of the obtained measurements was good, agreeing with reference and simulated dose values to within 2 % standard deviation for both standard and small fields.

This thesis concludes that the new pulse-resolved dosimetry system holds great potential for modern radiotherapy applications, such as stereotactic radiotherapy and intensity-modulated radiotherapy.

Risø-PhD-85 (EN)

May 2011

ISSN 0106-2840
ISBN 978-87-550-3935-3

Contract no.:

Group's own reg. no.:
10003-01

Sponsorship:

Cover :
Experimental setup during a typical measurement session on a hospital.
Upper panel: Fiber-coupled organic scintillators are placed in a solid water phantom and subject to high energy x-rays from a medical linear accelerator.
Lower panel: The radiation-induced light from the scintillators is transmitted through the optical fibers to the ME04 detector system.

Pages: 168
Tables: 13
References: 130

Information Service Department
Risø National Laboratory for
Sustainable Energy
Technical University of Denmark
P.O.Box 49
DK-4000 Roskilde
Denmark
Telephone +45 46774005
bibl@risoe.dtu.dk
Fax +45 46774013
www.risoe.dtu.dk

Preface

This thesis is written in partial fulfillment of the PhD degree requirements at the PhD school of physics at the Technical University of Denmark (DTU). The work described in this thesis was funded by and carried out at the Radiation Research Division, Risø National Laboratory for Sustainable Energy, DTU. The clinically relevant dose measurements were performed at Copenhagen University Hospital (Rigshospitalet), at Allgemeines Krankenhaus (AKH) in Vienna, and at Copenhagen University Hospital Herlev (Herlev Hospital).

The project was supervised by Lars R. Lindvold and Claus E. Andersen, both senior scientists at the medical dosimetry group at the Radiation Research Division, Risø DTU.

Acknowledgements

First of all, I would like to thank my supervisors Lars R. Lindvold and Claus E. Andersen. Both Lars and Claus have given me much needed guidance and support through the various challenges of this project; Lars with his extensive knowledge about optics and chemistry, Claus with his knowledge about medical dosimetry, S-PLUS, LaTEX and LabVIEW programming, and impressive practical experience with performing dosimetry and data acquisition in a hospital environment.

Rickard Ola Ottosson has also provided significant help in the completion of this work - especially regarding the small-field dosimetry study, by performing extensive Monte Carlo simulations and providing practical assistance during experiments at Herlev Hospital and at AKH in Vienna. I am also greatly indebted to the remaining present and former personnel of the medical dosimetry group for general help and fruitful discussions about science and other things: Sidsel M.S. Damkjær, Gustavo Kertzcher, Anja P. Strauss, Steffen Greilich and Jens Edmund.

Many people at the Radiation Research Division have helped me during this project and must be acknowledged accordingly: Nina Jensen for providing and reading out TLDs; Jakob Helt-Hansen and Arne Miller for help with gamma cells and readout of radiochromic film; Merete Larsen for giv-

ing me a much needed hand with travel expenses, invoices, bills and other paperwork; Bent Lauritzen for keeping me out of bureaucratic problems; Christina Ankjærgaard for being a great colleague and friend, and for good lunch times in the barrack (or Lille Christiania, as Claus would call it); Martin Thalbitzer for good scientific and non-scientific discussions (see you at Copenhell); and last but not least, the research technicians Finn Jørgensen, Søren V. Dalsgaard, Jørgen H. Jakobsen, Lars Pirtzel and Finn Villumsen for providing me with that invaluable 4 mm screw, thermistor or solid water grooving that I needed at numerous occasions.

Many thanks to Kristian Nielsen at DTU Photonics for providing us with microstructured polymer optical fibers. I would also like to thank the physicists at Rigshospitalet and Herlev Hospital for letting us use their linear accelerators for experiments (in as well as out of working hours), and for providing us with much needed technical assistance. I am especially grateful to Claus F. Behrens at Herlev Hospital, who has been a great support during the measurements that have occupied the main workload during the last year of this project.
Åsa Palm and Dietmar Georg have been of great assistance to us during our intensive trip to AKH in Vienna, and we are greatly indebted to them for their contribution.

This thesis is dedicated to the two people that my lack of time have affected the most: My girlfriend Ditte Eklund Nygaard and my baby daughter Aya. Thank you for your patience - you mean the world to me.

Abstract

This PhD project pertains to the development and adaptation of a dosimetry system that can be used to verify the delivery of radiation in modern radiotherapy modalities involving small radiation fields and dynamic radiation delivery.
The dosimetry system is based on fibre-coupled organic scintillators and can be perceived as a well characterized, independent alternative to the methods that are in clinical use today. The dosimeter itself does not require a voltage supply, and is composed of water equivalent materials. The dosimeter can be fabricated with a sensitive volume smaller than a cubic millimeter, which is small enough to resolve the small radiation fields encountered in modern radiotherapy. The fast readout of the dosimeter enables measurements on the same time scale as the pulsed radiation delivery from the medical linear accelerators used for treatment.
The dosimetry system, comprising fiber-coupled organic scintillators and data acquisition hardware, was developed at the Radiation Research Division at Risø DTU and tested using clinical x-ray beams at hospitals in Denmark and abroad.

Pulse-resolved measurements were found to exhibit a precision of 1-4 % standard deviation for dose delivery in static beams, and provided detailed information about transients in the dose per pulse at the beginning of each irradiation. The system was also used to measure a simulated RapidArc® treatment with dose per pulse resolution.
Measurements of output factors and percentage depth dose were performed and compared with reference values and Monte Carlo simulations for static square radiation fields for standard (4 cm x 4 cm to 20 cm x 20 cm) and small (down to 0.6 cm x 0.6 cm) field sizes. The accuracy of most of the obtained measurements was good, agreeing with reference and simulated dose values to within 2 % standard deviation for both standard and small fields.

This thesis concludes that the new pulse-resolved dosimetry system holds great potential for modern radiotherapy applications, such as stereotactic radiotherapy and intensity-modulated radiotherapy.

Resumé (Danish abstract)

Dette ph.d.-projekt har handlet om udviklingen og tilpasningen af et dosimetrisystem til verifikation af moderne former for stråleterapi, der gør brug af små strålingsfelter og dynamiske bestrålinger.
Dosimetrisystemet er baseret på fiberkoblede organiske scintillatorer og kan betragtes som et velkarakteriseret, uafhængigt alternativ til de metoder der benyttes klinisk. Selve dosimeteret kræver ingen spændingstilførsel, og består af vandækvivalente materialer. Dosimeteret kan fremstilles med et strålingsfølsomt volumen mindre end en kubikmillimeter, hvilket er tilstrækkeligt småt til at kunne benyttes i de små strålingsfelter, der benyttes i moderne stråleterapi. Den hurtige udlæsning af dosimeteret muliggør målinger på samme tidsskala som frekvensen af strålingspulser fra de medicinske lineære acceleratorer, der benyttes til behandling.
Dosimetrisystemet, bestående af fiberkoblede organiske scintillatorer og dataopsamlingshardware, er udviklet ved Afdelingen for Strålingsforskning på Risø DTU og testet ved hjælp af kliniske røntgenbestrålinger på hospitaler i Danmark og i udlandet.

Målinger med pulsopløsning kunne foretages med en præcision indenfor 1-4 % standardafvigelse for statiske bestrålinger, og indeholdt detaljeret information om transienter i dosis per puls i begyndelsen af hver bestråling. Systemet blev endvidere brugt til at foretage pulsopløste målinger under en simuleret RapidArc®-behandling.
Målinger af output-faktorer og dybdedosis-kurver blev foretaget og sammenlignet med referencemålinger og Monte Carlo-simuleringer i kvadratiske strålingsfelter for henholdsvis standard (4 cm x 4 cm til 20 cm x 20 cm) og små (ned til 0.6 cm x 0.6 cm) feltstørrelser. Nøjagtigheden var god for de fleste af målingerne, og stemte overens med referencemålinger og simuleringer indenfor 2 % standardafvigelse, for både standardfelter og små felter.

Denne afhandling konkluderer at det nye pulsopløste dosimetrisystem udviser et stort potentiale for anvendelser i moderne strålebehandlinger, såsom stereotaktisk stråleterapi og intensitets-moduleret stråleterapi.

Publications and presentations

The main results, findings and conclusions made during this PhD project have been submitted for publication in peer-reviewed international journals and presented as oral presentations and posters at international conferences. This section lists the various contributions. Papers written with the PhD student as first author are included as the last three chapters of this thesis.

Papers published in peer-reviewed international journals:

- Beierholm, A. R., Lindvold, L. R., and Andersen, C.E. (2011). Organic scintillators with long luminescent lifetimes for radiotherapy dosimetry. *Radiation Measurements*, doi:10.1016/j.radmeas.2011.04.016.
- Beierholm, A. R., Ottosson, R. O., Lindvold, L. R., Behrens, C. F., and Andersen, C. E. (2011). Characterizing a pulse-resolved dosimetry system for complex radiotherapy beams using organic scintillators. *Physics in Medicine and Biology*, 56(10):3033-3045.
- Beierholm, A. R., Andersen, C. E., Lindvold, L. R., and Aznar, M.C. (2010). Investigation of linear accelerator pulse delivery using fast organic scintillator measurements. *Radiation Measurements*, 45(3-6):668-670.
- Lindvold, L. R., Beierholm, A. R., and Andersen, C.E. (2010). An organic dye in a polymer matrix - A search for a scintillator with long luminescent lifetime. *Radiation Measurements* 45(3-6):615-617.

Oral presentations made at national and international conferences:

- Beierholm, A. R., Ottosson, R. O., Lindvold, L. R., and Andersen, C.E. (2010). Time-resolved small field dosimetry using organic scintillators. ESTRO 29, Barcelona. *Radiotherapy and Oncolology*, 96

(Supplement 1), Abstract # 53. A revised edition of the submitted abstract was included in the official ESTRO 29 Congress Report: http://www.estro-events.org/Documents/ESTRO29_report.pdf

- Beierholm, A. R., Andersen, C. E., Lindvold, L.R. (2009). Linear accelerator dose-per-pulse measurements using fiber-coupled organic scintillators. ESTRO 10th biennial, Maastricht. *Radiotherapy and Oncology*, 92 (Supplement 1), Abstract # 138.
- Beierholm, A. R., Andersen, C. E., Lindvold, L. R.(2009). Investigation of linear accelerator pulse delivery using fast organic scintillator measurements. LUMDETR 2009, Krakow.
- Beierholm, A.R. (2009). Using fiber-coupled organic scintillators to examine linear accelerator pulse delivery. DFS Nordic Meeting, Lyngby.

Posters presented at national and international conferences:

- Beierholm, A. R., Lindvold, L. R., Andersen, C.E. (2010). Comparison of custom-made organic scintillators with long luminescent lifetimes for radiotherapy dosimetry. SSD 16, Sydney.
- Beierholm, A. R., Lindvold, L. R., Andersen, C. E., Aznar, M. C. (2010). Time-resolved small field dosimetry using fibre-coupled organic scintillators. DSMF Symposium, Odense.
- Beierholm, A. R., Lindvold, L. R., Andersen, C.E. (2009). A comparison of organic BCF-12 plastic scintillators and Al_2O_3:C crystals for real-time medical dosimetry. DSMF Symposium, Odense.

Table of contents

Chapter 1

The need for medical dosimetry

Treatment of cancer using radiotherapy is always a balance between successfully killing cancerous tissue with lethal doses of ionizing radiation, and minimizing the resulting harmful effects on surrounding healthy tissue. Massive cell death and mutation beyond repair is the inevitable result when high-energy charged particles and photons introduce double-strand breaks in the DNA molecules of living cells. In radiotherapy, the so-called absorbed dose D is a surrogate for clinical response. This ensures traceability to a common standard, meaning that clinical results can be communicated among hospitals. The absorbed dose is defined as the radiation energy deposited in a medium per mass unit; the SI unit for absorbed dose is the gray (Gy), with 1 Gy equal to 1 J/kg. Successful radiotherapy must ensure maximal dose delivered to the tumor volume and minimal dose to healthy tissue and organs at risk. Common types of radiotherapy include i) brachytherapy, which employs internal irradiation of the tumor, and ii) teletherapy or external beam radiotherapy, where the ionizing radiation is delivered externally by a radioactive source or an accelerator.

Brachytherapy is an invasive treatment modality, taking place *in vivo* using radioactive sources inserted either in or close to the tumor volume. The practical handling of radioactive sources is typically achieved using remote after-loading; thin hollow guide tubes are inserted in the patient, and ionizing radiation is delivered by loading a small radioactive source (e.g. Iridium-192) into a guide tube, letting it dwell at a specified position in the tube for a specified amount of time before being loaded into another guide tube. Depending on the dwell time of the source at each specified position in each guide tube, a complex and highly conformal dose deposition profile can be applied to the tumor volume. Brachytherapy is commonly used for treating breast, prostate and cervical cancer.

Teletherapy and external beam radiotherapy are noninvasive treatments involving beams of high energy x-rays, electrons or heavier particles irradiating the patient. Treatments using x-ray beams are the most common for deep-seated tumors. The dose is delivered at various irradiation angles and dose rates, and for various field sizes and field shapes. The research presented in this thesis solely concerns x-ray radiotherapy beams delivered by medical linear accelerators (linacs), and we shall henceforth simply refer to external beam radiotherapy as radiotherapy.

1.1 Radiotherapy in general

The most common forms of radiotherapy involves externally generated beams of high-energy electrons or x-rays delivered by a medical linac to a target of cancerous tissue in the patient. As electrons have a very limited range in tissue, electron beams are only used for treating superficial tumors at 5 cm depth and less, i.e. skin cancer treatments and certain palliative treatments. High-energy x-ray beams are used to treat deeper-situated tumors. Because the intensity of an x-ray beam decays exponentially with depth, irradiating healthy tissue in front of and behind the tumor is inevitable. To minimize the dose delivered to healthy tissue while maximizing the dose delivered to the tumor, several beams are delivered consecutively from different angles.

1.1.1 The medical linear accelerator

An example of a modern medical linac is seen in figure 1.1. Modern linacs can typically deliver electron and x-ray beams of more than one specified energy. Electrons are generated from a filament (the electron gun) and accelerated to megaelectron volt (MeV) energies in an evacuated accelerating waveguide, producing an electron beam. An x-ray beam is, if required, generated from the primary electron beam by bremsstrahlung in a so-called x-ray target made of a material of high atomic number (e.g. tungsten). A large amount of kinetic energy is lost in the bremsstrahlung process and dissipated as heat, and the average energy of the resulting x-ray beam is roughly 1/3 lower than that of the primary electron beam (Johns and Cunningham, 1983).

The maximum required beam energy is governed by the length of the accelerating waveguide, and hereby also the size and overall design of the linac (Podgorsak, 2010). For x-ray beams of 4 to 6 megavolt (MV) energy, the electron gun and accelerating waveguide can be build directly into the linac treatment head; this is known as the "straight through" design, where the accelerator tube is mounted isocentrically and the electron beam is accelerated and directed straight towards the x-ray target and subsequently

Figure 1.1: A Varian Clinac® 2300 iX medical linac at the Division of Radiophysics, Herlev Hospital. The machine can deliver x-rays and electrons of different energies, and is equipped with kilovoltage and megavoltage onboard imaging for image guidance during treatment.

the patient.[1] Electron beams and x-ray beams of higher energies require a longer accelerating waveguide, which is mounted either in the gantry or in the gantry stand, parallel to the gantry rotation axis. In this case, the waveguide is horizontal and the electron beam is bent towards the target using a 270° quadrupole bending magnet (see figure 1.2). Most linacs used at radiotherapy clinics today are required to deliver x-ray beams of high MV energies; therefore, the vast majority of linacs are of the "bent beam" design.

Through the linac treatment head, the electron or x-ray beam diverges from a pencil beam a few mm in diameter to a large square beam of a size defined by primary and secondary collimator jaws. These jaws are made of a material with high atomic number, usually tungsten, which blocks transmission of radiation through them. The primary jaws are fixed while the secondary jaws are movable, defining the square dimensions of the clinically usable radiation field. To flatten the intensity distribution of x-ray

---

[1] The Cyberknife$^{\mathrm{TM}}$ system, developed by Accuray Inc., is a popular example of the "straight through" linac design.

beams, a so-called flattening filter is introduced below the target; for each specified x-ray beam energy, a specific combination of target and flattening filter is used. A clinical electron beam is generated by replacing the target and flattening filter with a scattering foil. Special applicators are needed to collimate the electron beam. A dose monitoring system, consisting of two independent transmission ionization chambers, is imbedded below the flattening filter/scattering foil.

All medical linacs are pulsed, meaning that the radiation is delivered in concentrated burst with a low duty cycle. Typically, the electron or x-ray beam has a duration of a few μs, while the time between subsequent pulses is on the order of a few ms. The pulsed operation of linacs means that the instantaneous dose rates are very high; as such, an average specified dose rate of 100 mGy/s corresponds to an instantaneous dose rate of roughly 60 Gy/s.

Linac calibration

For medical linacs used for radiotherapy, the unit of delivered dose is the monitor unit (MU). The MU is normally defined so that the delivery of 1 MU corresponds to a dose of 1 cGy for specified reference conditions defined by a certain field size, source to surface distance (SSD) and depth in water. For a 6 MV x-ray beam, a beam modality commonly used, the reference conditions for most linacs are: 10 cm x 10 cm field size, 100 cm SSD, and 1.5 cm depth in water (AAPM, 1999; IAEA, 2000). A medical linac is usually calibrated using an ionization chamber which has been subject to a calibration that is traceable to a primary standard (see section 1.3.2).

1.1.2 Treatment planning

Prior to radiotherapy, the volume to be treated - called the clinical target volume (CTV) - is chosen on the basis of imaging data provided by subjecting the patient to computed tomography (CT) scans. To account for uncertainties in patient setup and movement of the CTV during treatment, appropriate margins are added to the CTV to define the planning target volume (PTV). As stated by the International Commission on Radiation Units and Measurements (ICRU), the PTV is a judgement-based geometrical concept used for treatment planning, defined to select appropriate radiation beam data to ensure correct delivery of the prescribed dose to the CTV (ICRU, 1999). The PTV data are loaded into a computerized treatment planning system (TPS) which plans the treatment by adjusting the physical beam parameters, such as energy, field size and shape, irradiation angle, delivered dose and dose rate to create the necessary dose delivery profile to the PTV.

Radiotherapy is in most cases fractionated, normally consisting of 20 to 30

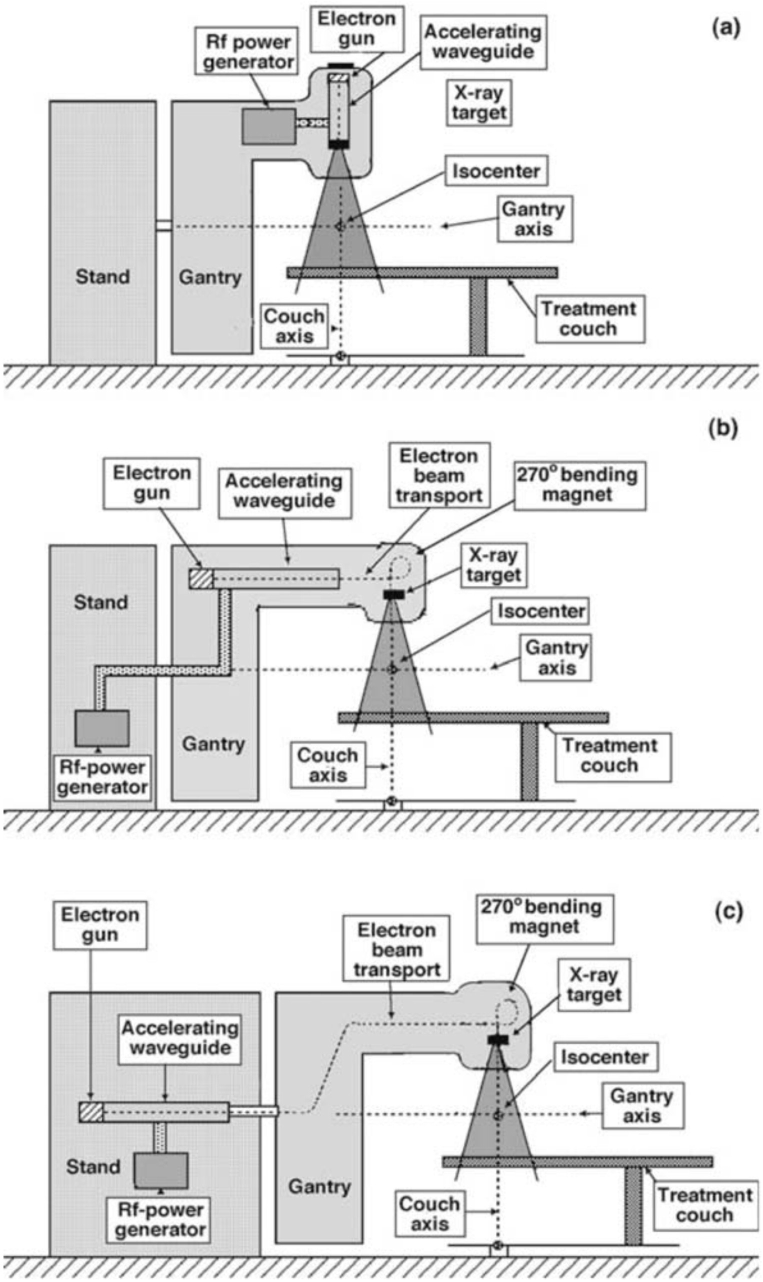

Figure 1.2: Typical medical linac design configurations. (a) "Straight-through" design with electron gun, waveguide and target isocentrically mounted in the linac head. (b) Intermediate-energy "bent beam" design where electron gun and accelerating waveguide are mounted horizontally in the linac gantry; the electron beam is directed towards the target using a bending magnet. (c) High-energy "bent beam" design with electron gun and accelerating waveguide mounted horizontally in the gantry stand; the electron beam is directed towards the target using a beam transport system and a bending magnet. Source: Podgorsak (2010).

fractions delivering 1.8-2.0 Gy each, adding up to a total delivered dose on the order of 50 Gy to the PTV (Mayles et al., 2007). This is done to further spare the irradiated healthy tissue, which in most cases is more efficient than cancerous tissue at repairing radiation-induced damage.

1.1.3 3-dimensional conformal radiotherapy

To conform the individual radiation beam to the PTV, the field size can be varied by the secondary collimator jaws situated in the linac treatment head. However, the secondary collimator jaws only define a rectangular or square field shape - to conform the dose satisfactorily, the field must be further shaped to follow the contours of the tumor volume. This is achieved in 3-dimensional conformal radiotherapy (3DCRT). One way to conform the beam is to position individually moulded lead blocks between the linac treatment head and the patient. Although this procedure can ensure conformity, a treatment involving several individually shaped beams becomes very time-consuming due to the moulding and replacement of each lead block.

A much more efficient way to shape the treatment fields has become available by the introduction of multi-leaf collimators (MLCs). These are build into the linac head, either replacing the secondary collimator jaws or being positioned below them as a tertiary collimator system. The function of the MLCs is similar to that of the jaws, but instead of two perpendicular sets of opposing jaws forming a rectangular field the MLCs consist of an array of parallel, closely spaced individual collimator leafs. Each leaf is typically 5 or 10 mm wide and can be individually positioned from opposing sides to create a field shape that conforms to the desired area. The drawback of MLCs compared with jaws is that they are thinner on the axis parallel to the beam, and therefore suffer from a larger portion of radiation leaking through them. They are therefore used in conjunction with jaws to ensure optimal conformity during treatment. In this way, the shape of the field can be mechanically set within a couple of seconds, and therefore a lot of time and money are saved compared to the use of individually moulded lead blocks. In cases like whole body irradiation, lead blocks are however still used to minimize irradiating sensitive organs like the heart and lungs.

1.1.4 Stereotactic radiotherapy

In the case of very small and well defined tumors, radiotherapy is delivered using small, precisely shaped radiation beams and a small number of fractions, yielding a concentrated and accurate treatment. This is the case in stereotactic radiosurgery (SRS), which is typically employed against tumors in and around the brain and spine, as well as in stereotactic body radiotherapy (SBRT) which is used for treating localized tumors elsewhere in the body, such as in the lungs. In this thesis, stereotactic radiotherapy shall

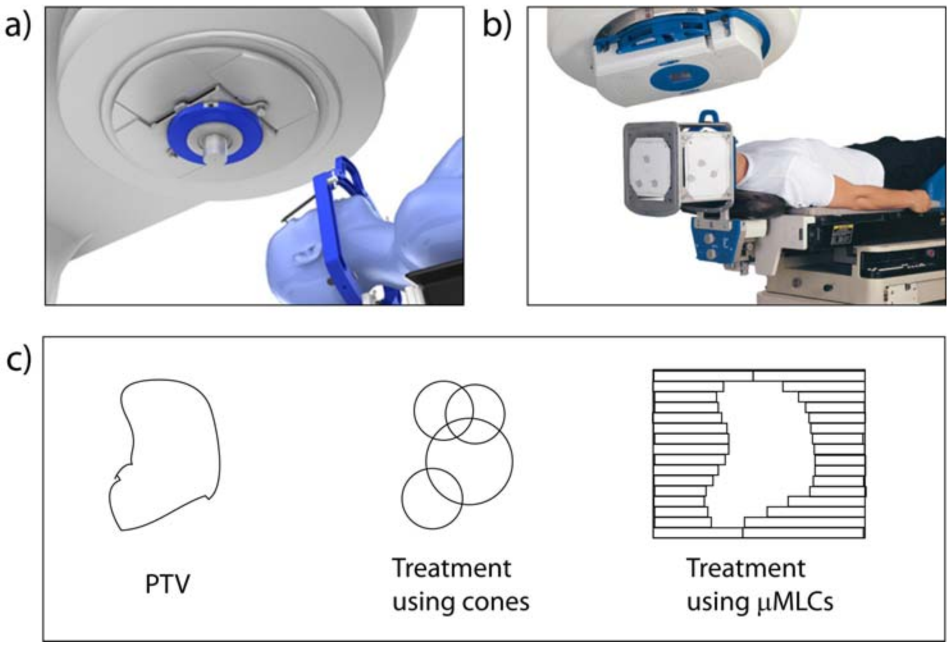

Figure 1.3: Two tertiary beam-shaping solutions used in stereotactic and conformal radiotherapy. a) A Brainlab conical collimator. b) The Brainlab M3$^{\mathrm{TM}}\mu$MLC array. Source: http://www.brainlab.com. c) Schematic view of the conformation to the PTV using either cones or μMLCs.

refer to both SRS and SBRT unless stated otherwise.
Most stereotactic treatments today can in principle be delivered by a standard linac by mounting an external collimator system on the bottom part of the linac treatment head (see figure 1.3). The additional collimator system can either be a series of interchangeable cone-shaped collimators, or an array of μMLCs (special MLCs of 2.5-5.0 mm leaf width instead of the standard 5.0-10.0 mm) to attain required conformity to the small target. Because of the narrow beam geometries used in stereotactic treatments, the dosimetry equipment used for dose verification and quality assurance (QA) must exhibit a high degree of spatial resolution in order to measure the dose deposition in small fields accurately.

1.1.5 Intensity modulated radiotherapy

To further conform the dose distribution to the PTV and spare adjacent sensitive organs, the intensity of each radiation beam can be modulated by moving the MLC leafs during treatment. This is achieved in intensity modulated radiotherapy (IMRT). An IMRT treatment is normally performed in either of two ways: Either step and shoot (static MLCs), where many beams of different shape are used, or sliding window (dynamic MLCs), where the field is shaped dynamically by moving the MLC leafs while the beam is on. By modulating the radiation beams, complex PTVs such as concave tumors enveloping organs at risk can be irradiated while still maintaining a low dose to the healthy tissue.

IMRT mainly differs from 3DCRT in the use of so-called inverse treatment planning. In conventional treatment planning, a dose distribution is calculated based on a choice of beam parameter combinations; the optimal dose distribution is found by trial and error. In inverse treatment planning, the designated dose profile is specified in the TPS by the physicist. A computer program then calculates the required delivery pattern and individual beam parameters to form the treatment plan. When using inverse treatment planning, the beam parameters are to a large degree chosen entirely by the TPS and therefore IMRT is a more advanced, computer-dependent treatment technique than 3DCRT.

Because IMRT treatments make use of composite fields made up of small sub-fields, stringent demands on dosimetry equipment apply to IMRT QA as for stereotactic radiotherapy.

Volumetric arc therapy

Volumetric modulated arc therapy, or simply arc therapy, is a newly developed refinement of IMRT. The most common examples of this treatment is RapidArc® (developed by Varian Medical Systems Inc. USA) and VMAT (developed by Elekta AB, Sweden). In arc therapy, the entire treatment is delivered using one or more rotation arcs of the linac gantry with the radiation beam turned on during the entire arc. During each arc, the shape of the field, the rotation speed of the gantry and the rate of dose delivery can be varied continuously and independently to create the planned dose distribution. It has been shown that an arc therapy treatment can produce dose distributions similar to those produced using any other IMRT treatment, but the treatment time is much faster and the number of delivered monitor units is lower (Otto, 2008).

1.2 Medical dosimetry: Why and how

Because the ionizing radiation deployed in radiotherapy have the ability to kill cancerous as well as healthy cells more or less indiscriminately, great care must be made to concentrate the radiation to the tumor volume in order to spare the healthy tissue as much as possible. This is illustrated in the terms *tumor control probability* (TCP) and *normal tissue complication probability* (NTCP); the goal of successful radiotherapy is to ensure a TCP as high as possible with a minimal increase in NTCP. Because of this demand, the technology and complexity of radiotherapy still evolves, putting a high demand on the need for independent measurements checking and securing the

A Lifesaving Tool Turned Deadly

Radiation Offers Powerful New Cures, and Ways to Do Harm

By WALT BOGDANICH

As Scott Jerome-Parks lay dying, he clung to this wish: that his fatal radiation overdose — which left him deaf, struggling to see, unable to swallow, burned, with his teeth falling out, with ulcers in his mouth and throat, nauseated, in severe pain and finally unable to breathe — be studied and talked about publicly so that others might not have to live his nightmare.

Sensing death was near, Mr. Jerome-Parks summoned his family for a final Christmas. His friends sent two buckets of sand from the beach where they had played as children so he could touch it, feel it and remember better days.

Mr. Jerome-Parks died several weeks later in 2007. He was 43.

A New York City hospital treating him for tongue cancer had failed to detect a computer error that directed a linear accelerator to blast his brain stem and neck with errant beams of radiation. Not once, but on three consecutive days.

Soon after the accident, at St. Vincent's Hospital in Manhattan, state health officials cautioned hospitals to be extra careful with linear accelerators, machines that generate beams of high-energy radiation.

But on the day of the warning, at the State University of New York Downstate Medical Center in Brooklyn, a 32-year-old breast cancer patient named Alexandra Jn-Charles absorbed the first of 27 days of radiation overdoses, each three times the prescribed amount. A linear accelerator with a missing filter would burn a hole in her chest, leaving a gaping wound so painful that this mother of two young children considered suicide.

THE RADIATION BOOM

When Treatment Goes Awry

Ms. Jn-Charles and Mr. Jerome-Parks died a month apart. Both experienced the wonders and the brutality of radiation. It helped diagnose and treat their disease. It also inflicted unspeakable pain.

Yet while Mr. Jerome-Parks had hoped that others might learn from his misfortune, the details of his case — and Ms. Jn-Charles's — have until now been shielded from public view by the government, doctors and the hospital.

Americans today receive far more medical radiation than ever before. The average lifetime dose of diagnostic radiation has increased sevenfold since 1980, and more than half of all cancer patients receive radiation therapy. Without a doubt, radiation saves countless lives, and serious accidents are rare.

But patients often know little about the harm that can result when safety rules are violated and ever more powerful and technologically complex machines go awry. To better understand those risks, The New York Times examined thousands of pages of public and private records and interviewed physicians, medical physicists, researchers and

Continued on Page 14

Figure 1.4: Lethal radiotherapy accidents were on the front page of the New York Times on January 24th, 2010. An analysis of New York state records showed a total of 621 reported medical radiation mistakes in the period of 2001-2009. The most common causes of mistakes were flawed QA and erroneous data entries/calculations performed by personnel.

correctness of the treatment. The need for balancing TCP against NTCP have resulted in the formal demand that for a successful treatment, the dose must be delivered with a discrepancy of no more than 5 % with respect to the planned dose (ICRU, 1976). Because of this, a dose delivery error of 5 % or larger during treatment is considered a serious and unacceptable error. Recent examples of serious radiotherapy accidents (New York Times, 2010a,b) suggest that lethal treatment errors still occur, even for highly advanced treatment modalities like IMRT (figure 1.4). In order to detect such errors, QA and independent dose verification must be performed routinely and efficiently. Furthermore, external audits and randomized trials between different hospitals is a necessity in order to establish and maintain sufficient medical dosimetry procedures locally and in general (IAEA, 2005). International audit programs, such as the IAEA postal audit program (Izewska et al., 2002) provides the hospitals involved with a much needed platform for comparing and checking the quality of their radiotherapy procedures. Such audit programs typically operate with a 5 % acceptance limit for differences

between clinics (IAEA, 2003); this acceptance limit is adopted from the recommendations stated in the ICRU Report 24 (ICRU, 1976), and is based on the same arguments.
Medical dosimetry can either be performed in phantoms, this being either water tanks, water-equivalent plastic phantoms or anthropomorphic phantoms, or *in vivo*, meaning that the radiation sensitive part of the dosimeter is placed either on the skin of the patient or inside body cavities. According to ICRP (2000), *in vivo* dosimetry should be performed on a routine basis to reduce the probability and severity of errors and accidents in radiotherapy. Whether a dosimeter is used for *in vivo* treatment verification, routine QA, machine QA or an external audit, the dosimeter must be able to measure the dose delivered during treatment with good accuracy and precision well within the 5 % acceptance limit. To be more specific, dosimetric precision within 2 % is acceptable, as this is the same as the requirement on linac output constancy and treatment planning (IAEA, 2005). For this requirement to be fulfilled, several demands must be met. First of all, dosimeter response must be reproducible and stable, even after being exposed to kGy-order accumulated absorbed dose. Additionally, the dosimeter response must be linear with dose, dose rate and dose per pulse, and exhibit negligible dependence on energy, temperature and irradiation angle. Good spatial and temporal resolution is demanded for the dosimetry of complex radiotherapy beams like the ones encountered in stereotactic radiotherapy and IMRT.

The technical aspects of modern radiotherapy are constantly developing in order to optimize the irradiation of cancerous tissue while minimizing side effects to the patient. A disadvantage of the more advanced treatments is reduced transparency and reduced intuitive knowledge about the delivery of radiation during treatment. The modern, complex types of radiotherapy are putting high technical demands on the accelerators and the treatment planning software, as well as on the dosimetry equipment used for QA and dose verification. This is specifically the case for the increasing use of small and irregular fields in modern radiotherapy, necessitating correct dose measurements in narrow beams and high dose gradients to ensure correct treatment delivery. The use of dosimeters that are too large to resolve the dose profile of a narrow beam will inevitably yield a severe error in dose estimation, which can be detrimental if used as beam data for treatment planning. This occurred with the Novalis Tx$^{\mathrm{TM}}$ stereotactic system (Brainlab AG, Germany) in 2007, where the commissioning of a 6 mm x 6 mm μMLC-defined field was performed with an inappropriately large detector. The resulting data were entered into the treatment planning system, resulting in the mistreatment of 145 patients worldwide (IPEM, 2010). This would likely have been circumvented by using a dosimeter better suited for small fields. According to Laub and Wong (2003), the commissioning of IMRT treatment planning tools with detectors that have a limited spatial resolution can lead

to the introduction of systematic errors, a statement that is supported by the mentioned Brainlab incident.
A recent study by Fog et al. (2011), examined the accuracy of RapidArc® radiosurgery delivery in the context of very small fields. For small field segments 1-4 μMLC leafs wide, dose was calculated using the TPS and compared with dose measurements performed using three different dosimetry methods. The results showed that the TPS underestimated the dose delivered by 23-51 % for the smallest field achievable (1 μMLC leaf wide, i.e. 2.5 mm). Furthermore, measurements and calculations of a RapidArc® delivered to a 0.4 cm^3 PTV showed that the measured dose was approximately 20 % higher than the dose calculated by the TPS. This significant discrepancy was believed to be caused by the use of these small field segments, which is a signature feature of RapidArc® plans. The study by Fog et al. (2011) is thus another example of how dosimetry procedures of high spatial resolution can uncover, and possibly reduce, significant systematic dose delivery errors in complex radiotherapy.

1.3 State of the art

This section introduces the most relevant methods for medical dosimetry today. Some of the methods, like ionization chambers and silicon diodes, have been used on a routine clinical basis for decades, while other methods still awaits commercial availability. Dosimeter systems can be used for either 1-D, 2-D or 3-D dosimetry. One-dimensional dosimeters or point dosimeters measure the dose at a defined point, while two- and three-dimensional dosimetry systems measure dose distributions e.g. for IMRT verification. A selection of point dosimeters are shown in figure 1.5.

1.3.1 Calorimetry and primary standards

Calorimeters have the ability to measure the unit of absorbed dose, the gray, in the way it is defined - as the energy absorbed per unit mass. Thus, a calorimeter measures absorbed dose as the radiation-induced temperature increase of a volume of water or graphite (absolute dosimetry). The measurement of absorbed dose using a water or graphite calorimeter however requires complicated and time-consuming procedures, and measurements are mostly restricted to conventional reference conditions, such as 10 cm x 10 cm fields (IPEM, 2010). Water and graphite calorimeters are available at standards measurement laboratories, such as the NPL in London, and are used as primary standards against which other dosimetry systems are calibrated. Primary standards are dosimetry systems of the highest attainable metrological quality, and the measurement of 1 Gy using a primary standard is the basis of clinical reference dosimetry. A dosimeter - typically an ionization chamber - which is to be used as reference dosimeter (secondary standard) at

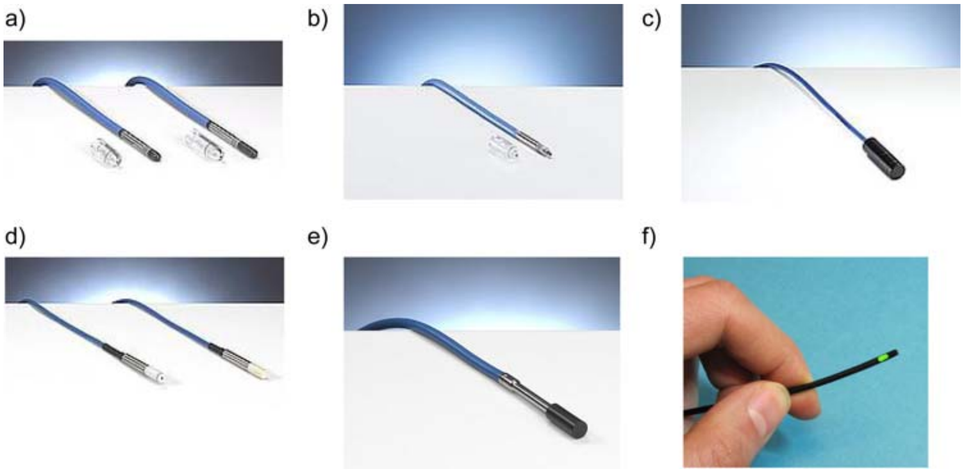

Figure 1.5: Various point dosimeters. a) PTW 31010 and 31013 Semiflex ionization chambers (125 mm^3 and 300 mm^3 detection volume, respectively). b) PTW 31014 Pinpoint® ionization chamber (15 mm^3 detection volume). c) PTW microLion® liquid ionization chamber (2 mm^3 detection volume). d) PTW 60016 p-type dosimetry diodes (0.03 mm^3 detection volume). e) PTW 60003 diamond detector (1 mm^3 detection volume). Source: http://www.ptw.de. f) fiber-coupled organic scintillator (1 mm^3 detection volume).

a hospital, is sent to a standards laboratory, where it is calibrated against the primary standard, yielding a calibration coefficient relating dosimeter response to absorbed dose to water. Apart from calorimetry, primary standards of absorbed dose to water can also be obtained from graphite cavity ionization chambers (ionometric standards) and Fricke dosimeters (chemical dosimetry standards) (IAEA, 2005).

1.3.2 Ionization chambers

The golden standard of radiotherapy dosimetry has so far been the ionization chamber. All radiotherapy departments are in possession of at least one reference ionization chamber that has been subject to traceable calibration at a standards laboratory.

An ionization chamber typically consists of an air-filled cavity and a central electrode, and is connected to an electrometer via a coaxial cable. The incident radiation beam ionizes the air molecules in the radiation-sensitive volume of the chamber, and the high voltage applied to the chamber ensures collection of the resulting ions on the electrode. The ionization current is measured by the electrometer, being proportional to the dose rate in the chamber volume (Attix, 1986; Khan, 2003). Ionization chambers used for dosimetry of radiotherapy x-ray beams are of the thimble chamber variant, where either the anode or the cathode is embedded in the chamber wall, while the other is placed along the central axis of the chamber. In contrary, ionization chambers used for electron beam dosimetry are parallel-plate chambers.

Ionization chambers have low sensitivity compared with solid organic and inorganic detector materials, and are inappropriate for *in vivo* applications because of their large size and need of high-voltage supply. ionization chambers are therefore mostly constrained to phantom measurements, e.g. in a water tank. Because the actual dosimeter material is an air-filled cavity, the sensitivity of the chamber is pressure and temperature dependent. Furthermore, because of the low-density medium of the dosimeter, energy dependent sensitivity changes are also an issue when using ionization chambers in radiotherapy beams. However, applying well-defined correction factors ensures high precision and accuracy of ionization chambers, making them an invaluable tool for beam calibration and reference dosimetry. The estimated relative uncertainty on measured dose to water at reference conditions, using an ionization chamber, is approximately 1.5 % (IAEA, 2000).

For applications such as machine QA and IMRT verification, a few commercial solutions are available in the form of two-dimensional ionization chamber arrays. One example, the PTW 2-D ARRAY seven29®, consists of 729 cubic ionization chambers, each of 125 mm^3 sensitive volume (see figure 1.6). However, most ionization chambers lack the sufficient spatial resolution to be used in small radiation fields, which are commonly encountered in stereotactic radiotherapy as well as IMRT. Although miniature chambers with active volumes between 7 mm^3 and 30 mm^3 are commercially available, the sensitivity is significantly reduced because of the small chamber volume (IPEM, 2010). In this context, liquid-filled ionization chambers such as the PTW microLion® show promise.

1.3.3 Diodes

Semiconductor diodes are a common alternative to ionization chambers in common clinical practice. They are considered to be simpler, more sensitive and easier to use than ionization chambers, and are typically used for *in vivo* dosimetry through placement on the skin of the patient, measuring entrance and exit doses during radiotherapy. The diode functions by electron-hole pairs created by the ionizing radiation, creating a current through the p-n junction of the diode sensitive material. The dosimetric characteristics of diodes are primarily defined by the diode material, the doping level (i.e. the charge carrier concentration) and the size of the sensitive volume. Diodes can be classified as either "p-type" or "n-type". A disadvantage of both p- and n-type diodes is that the sensitivity decreases with accumulated dose, as the charge carriers themselves suffer from radiation-induced damage. For example, Jornet et al. (2000) found that a p-type diode exhibited a sensi-

Figure 1.6: Two examples of commercial point dosimeter 2-D arrays for IMRT verification and QA. Left: PTW 2-D ARRAY seven29$^{®}$ ionization chamber array, comprising 729 cubic chambers. Source: http://www.ptw.de. Right: Scandidos Delta$^{4®}$, consisting of 1069 p-type diodes arranged in a cross-plane configuration in an acrylic cylinder phantom. Source: http://www.scandidos.com.

tivity decrease of 8% after 300 Gy, while the sensitivity of an n-type diode was seen to decrease approximately 0.3 % after 300 Gy. The sensitivity of diodes also depend on temperature, energy, dose rate and irradiation angle, and therefore corresponding correction factors must be applied to ensure usable dose measurements.

Apart from single-diode point measurements, diodes are also a common choice in commercial dosimeter arrays for IMRT QA. The MapCHECK^{TM} two-dimensional diode array (Sun Nuclear Inc., USA) is an example of this, involving 445 n-type diodes, each of 0.64 mm^2 sensitive area, covering a 22 cm x 22 cm field. Another popular example is the Delta$^{4®}$ system (Scandidos AB, Sweden), employing an array of 1069 p-type diodes (approximately 0.1 mm^3 sensitive volume) arranged in a cross-plane (”X”) profile and embedded in a cylindrical acrylic phantom (see figure 1.6). An important characteristic of the Delta$^{4®}$ is that it measures dose absorbed for each individual radiation pulse from the linac with high precision (Sadagopan et al., 2009).

1.3.4 Thermoluminescence dosimeters

When exposed to ionizing radiation, certain crystalline materials store the incident radiation energy in the form of electron-hole pairs trapped in energy levels (traps) between the crystal valence and conduction bands. The energy can be released by recombination of the electron-hole pairs at a recombination center in the band gap, but it requires excess energy to excite electrons and holes out of the trap states. A material exhibiting thermoluminescence (TL) emits visible light when heated to a temperature that yields the right thermal energy to excite electrons and holes from the energy traps. Such a material can be used as a thermoluminescence dosimeter (TLD) in radiotherapy; the TLD is subject to the radiation field, and the radiation energy generates electron-hole pairs that are prevented from recombining by the traps. After irradiation, the TLD is heated to 400 °C or more, releasing the trapped energy by allowing the electron-hole pairs to recombine. The intensity of the heat-induced light from the TLD is proportional to the absorbed dose. Sensitivity can however be subject to large changes, and as a consequence annealing (i.e. resetting of the TLD by emptying all dosimetric traps through heating) and calibration must be performed before each irradiation. An example of a TLD base material is lithium fluoride (LiF), which is a common and well characterized choice due to its good tissue equivalence as well as high sensitivity and dynamic range, able to measure doses from μGy to kGy (Johns and Cunningham, 1983).[2]

TL-based dosimetry is an example of passive dosimetry, where the dose absorbed in the dosimeter is read out after each irradiation. Thus, time-resolved measurements are not achievable, and readout is time consuming. TLDs have been widely used for radiotherapy QA in clinical audits (Kroutilíková and Zácková, 1999; Izewska et al., 2002), both in phantoms and *in vivo*. TLDs can be made quite small and can therefore potentially be used for small-field dosimetry, but uncertainties lower than 2-3 % have proven difficult to achieve because of the complicated readout procedure (Francescon et al., 1998).

1.3.5 Optically stimulated luminescence dosimeters

For certain materials, the emission of light can be perceived as a measure of absorbed dose. As is the case in TLD materials, electron-hole pairs are generated in the conduction and valence bands of the crystalline material. Some electrons immediately recombine with holes at a recombination center, resulting in radioluminescence (RL), while some electrons fall into trap states induced by crystal impurities. These trapped electrons can be re-excited into the conduction band by photons of a certain wavelength. The resulting recombination with holes at the recombination center causes photon emission, hence the term optically stimulated luminescence (OSL). An example of these mechanisms are shown in figure 1.7, illustrating the energy band structure of carbon-doped aluminium oxide (Al_2O_3:C). This material exhibit TL as well as RL and OSL properties.

Materials capable of OSL can be used as passive dosimeters in a manner similar to TLDs. Sometimes referred to as optically stimulated luminescence dosimeters (OSLDs) (Yukihara and McKeever, 2008) or radiophotoluminescence detectors (Arakia et al., 2004), the dosimeters can be read out using

---

[2] Pure LiF is not a TLD material, but can be doped with small amounts of impurities such as magnesium and titanium to give it thermoluminescence properties. Common examples are LiF:Mg,Ti and LiF:Mg,Cu,P.

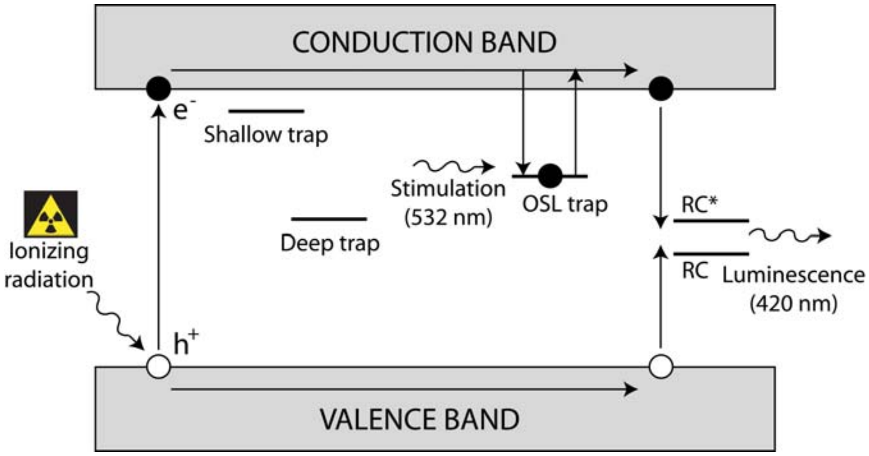

Figure 1.7: Band structure schematic for luminescence generation in an Al_2O_3:C crystal. Ionizing radiation excites electrons into the conduction band, leaving hole states in the valence band. Some electrons recombine with holes at the recombination center (designated RC), causing RL. Other electrons are trapped in dosimetry traps, and can later be released from the traps if optical energy is provided. After stimulation they can recombine with holes at the recombination center, causing OSL.

laser light after irradiation. OSL materials can also be coupled to optical fibers, as will be discussed in section 1.3.13.

1.3.6 EPR dosimetry using alanine

The generation of free radicals by ionizing radiation is the main principle in alanine dosimeters. Similar to TLDs and OSLDs, alanine is used as a passive dosimeter. Crystalline alanine pellets are placed in the radiation field and is read out post-irradiation using electron paramagnetic spin resonance (EPR) spectroscopy. The resulting spectrum provides information on the number of generated free radicals, which is directly proportional to the absorbed dose. The size and shape of the alanine pellets can be customized to fit the experimental requirements, and alanine therefore shows great theoretical potential for small-field dosimetry. This approach was tried by Chen et al. (2005).

Alanine exhibits a low sensitivity, meaning that pellets must be subject to high doses (Gy to kGy) to achieve reasonable measurement precision. An arguable disadvantage of alanine dosimetry is the need of EPR equipment for dose readout, which makes alanine dosimetry more suitable for physics laboratories than for hospitals. Another disadvantage is that alanine pellets are not water proof, greatly complicating measurements in liquid water.

As is also the case with TLDs, dosimeter readout by EPR is complex and time demanding. Although EPR dosimetry and alanine are commonly associated, lithium formate monohydrate has also been investigated for EPR dosimetry, exhibiting higher sensitivity than alanine (Vestad et al., 2004; Gustafsson et al., 2008).

1.3.7 MOSFETs

The metal oxide semiconductor field-effect transistor (MOSFET) is a transistor commonly used for digital and analog circuitry, but it has also found applications in radiotherapy dosimetry, primarily for *in vivo* dosimetry applications. The MOSFET functions by the radiation-induced trapping of charge in an oxide layer, yielding a change in the threshold voltage that is proportional to dose. The integrated dose may be measured during or after irradiation. The MOSFET has an extremely thin and sensitive detection area (dimensions less than 1 μm), which in principal makes the detector ideal for skin dose as well as entrance and exit dose measurements. Like the diode dosimeter, the MOSFET is subject to sensitivity degradation with accumulated dose, and has a limited useable lifetime. MOSFETs also exhibit temperature dependence, which however can be suppressed by using double detectors (IAEA, 2005). Although the MOSFET exhibits excellent spatial resolution, some studies recommend against its use in small field dosimetry (Francescon et al., 1998; Sauer and Wilbert, 2007) and dynamic IMRT verification (Ramasehan et al., 2004) due to poor accuracy and precision as well as a drift in response.

1.3.8 Diamond detectors

In small radiotherapy fields, dosimeters made of natural diamond have proven superior to ionization chambers and diodes due to small size, high sensitivity, good tissue equivalence and resistance to radiation damage (Heydarian et al., 1996; Bucciolini et al., 2003; Laub and Wong, 2003). The diamond has a volume of approximately 1 mm^3 and is sitting in a polystyrene housing, with gold contacts applying a bias voltage. When subject to ionizing radiation, the resistance of the diamond changes, yielding a current signal that is proportional to dose rate. Diamond detectors exhibit negligible temperature dependence and are energy independent, which is another advantage when applied in small fields involving large dose gradients. Disadvantages of natural diamond dosimeters are limited availability, dose rate dependence and the need for pre-irradiating the diamond before each use. At present, only one brand of natural diamond detector (the PTW 60003) is commercially available. However, research into diamond detectors made using chemical vapor deposition is promising (Buttar et al., 2000).

1.3.9 Radiochromic film

In the radiation-sensitive dye material polydiacetylene, ionizing radiation causes a polymerization process that can be measured as a change in the optical density of the dye. This process is used for radiotherapy dosimetry in a radiochromic film, which typically consists of a μm-thick layer of the radiosensitive dye either bonded to a mylar or polyester base. When exposed to ionizing radiation, the film is shaded blue, and the change in optical density is linearly proportional to the absorbed dose for doses in the cGy to Gy range. Radiochromic film can therefore be used as a 2-D dosimeter to e.g. measure lateral dose profiles of single or composite radiotherapy fields. The radiation-induced coloring is self-developing and establishes after a couple of hours after irradiation. The film can be read out using a commercial flatbed scanner and appropriate software. Although the coloring is insensitive to visible light, care should be taken not to expose the film to UV-light and high temperatures.

A commonly used brand of film for radiotherapy dosimetry is Gafchromic$^{\text{TM}}$ EBT, which however recently was replaced by the newer EBT2 generation. Radiochromic film is considered near-tissue equivalent and exhibits good spatial resolution and high dynamic range. A minor degree of energy dependence is however evident; the Gafchromic$^{\text{TM}}$ EBT has been reported to exhibit an under-response to low energy x-rays in the kilovoltage (kV) range (Butson et al., 2005; Lindsay et al., 2010), while the Gafchromic$^{\text{TM}}$ EBT2 has shown a small over-response at low energies. However, Lindsay et al. (2010) also states that energy dependence is highly influenced by the chemical composition of the film, and different lots of film might therefore exhibit differing energy dependence characteristics. The measurement uncertainty that can be obtained with radiochromic film can in principle be within 3% standard deviation (SD); studies by McLaughlin et al. (1994) and Lee et al. (2006) have reported agreement within 2 % between absorbed dose measured with radiochromic film and planned dose for stereotactic treatment fields. However, inhomogeneities due to manufacturing can lead to large uncertainties; in the case of the EBT2, uncertainties up to 8.7 % have been reported (Hartmann et al., 2010).

1.3.10 3-D dosimetry

Fricke gels, polymer gels and polymer solids are so far the only methods able of showing true, three-dimensional dose distributions, and are therefore potentially useful for IMRT and arc therapy QA applications.

Fricke gel dosimetry is based on the radiation-induced conversion of Fe^{2+} ferrous ions into Fe^{3+} ferric ions in ferrous sulphate solutions dispersed in a gel matrix. The resulting change in paramagnetic behavior and optical absorption is proportional to the absorbed dose and can be measured using nuclear magnetic resonance imaging and optical scanning methods (IAEA, 2005). A disadvantage of Fricke gels is blurring of the dose distribution with time, caused by continuous diffusion of the ferric ions. The development of leuco-dye doped solid polymers, such as the so-called PRESAGE$^{\mathrm{TM}}$, has significantly diminished this diffusion problem, resulting in a higher precision of the measured dose distribution (Adamovics and Maryanski, 2006). The incident radiation causes the leuco dye to oxidize, leading to a change in the optical density of the medium which is proportional to the absorbed dose. The dose distribution can then be obtained from the 3-D polymer using optical CT scanning. However, care should be taken to prevent bleaching of the signal between irradiation and readout, by storing the gel at low temperatures and protecting it against UV light (Baldock et al., 2010). In addition, any 3-D gel or solid must be prepared with great care to avoid inhomogeneities leading to significant systematic errors.

1.3.11 EPIDs

Electronic portal imaging devices (EPIDs) are primarily used for verifying patient setup prior to treatment. Several generations of EPIDs have been used clinically; EPIDs based on liquid ionization chambers have been replaced by camera-based systems, which today have mostly been replaced by the amorphous-silicon type (aSi) EPIDs. An EPID measures the dose transmitted through the patient, and hereby provides indirect information of the dose absorbed inside the patient (transmission mode). It can however also be used to measure the energy fluence from the linac beam directly (non-transmission mode). This enables dose verification, both pre-treatment and during treatment, in either transmission or non-transmission mode.

The field of EPID-based clinical dosimetry has been widening, especially concerning patient-specific IMRT QA (van Elmpt et al., 2008). However, an EPID is primarily designed for imaging purposes. Thus, the device is built of several layers of differing chemical composition to optimize the quantum efficiency, affecting the dose response of the device. It also makes the EPID non-water equivalent, necessitating the use of correction factors when comparing EPID-measured dose with e.g. TPS-calculated dose (Gustafsson et al., 2009). Energy dependence has also been reported, due to an over-response to low energy x-rays induced by the different scatter conditions of the layers. According to McDermott et al. (2006), under-response caused by charge trapping in the bulk layers seems to be a general problem for aSi-EPIDs for short irradiation times and low delivered doses. Apart from these shortcomings, the EPID is a convenient tool for patient-specific *in vivo* dose estimation.[3]

---

[3] It must be emphasized that EPID-based patient dosimetry regards estimated dose in the patient, extrapolated from dose measured outside the patient, rather than true *in vivo* measured dose.

1.3.12 Other time-resolved 2-D dosimetry devices

The development of 2-D systems based on scintillator sheets has been investigated for time-resolved QA applications in dynamic radiotherapy. The idea was originally introduced by Boon et al. (1998), who presented a phantom-based 2-D dosimetry system to be used in scanning proton beams. The radiation-induced light from a scintillator screen was directed towards a charged-coupled device (CCD) camera using a 45° mirror.

Petric et al. (2006) presented a similar system to be used in clinical x-ray beams, consisting of a water-filled Lucite phantom with a scintillator sheet embedded in the top. The presented system was able to accurately measure dose profiles for static and dynamic wedge-modulated fields, although dependence on field size and dose rate was evident.

The so-called DosiMap was presented by Frelin et al. (2008b) and regarded a scintillator sheet in a polystyrene phantom. The primary focus of that study was the removal of Cerenkov radiation, which was considered the main source of noise in this type of system. Two different correction methods were applied and tested for a horizontal static field as well as for vertical wedged fields and simple IMRT segment fields. A subtractive method, using a transparent/opaque chessboard pattern placed between the scintillator sheet and the CCD, gave the best results. Good accuracy could be obtained for the static square and wedged fields, but the limited spatial resolution of the method was evident in the IMRT segment field due to the 2 mm x 2 mm period of the chessboard pattern. The other subtraction method, which was based on colorimetric discrimination, was found to induce significant systematic errors in dose distributions involving large spatial dose gradients.

1.3.13 Fiber-coupled optical dosimeters

Certain organic and inorganic materials promptly emit visible light when subject to ionizing radiation. If a small piece of such material is coupled to an optical fiber and placed in the radiation field, the radiation-induced light signal can be transmitted to a photodetector and used as a measure of absorbed dose. In this way, fiber-coupled optical dosimeters can be used to ensure correct dose delivery during radiotherapy. Because the optical dosimeter can be made quite small and does not need a high-voltage supply, it can be used for *in vivo* dosimetry, for example inside brachytherapy guide tubes (Andersen et al., 2009) or attached to clinical rectal balloons (Archambault et al., 2010). An extensive overview of fiber-coupled luminescence dosimetry was recently presented by Andersen (2011).

The major problem inherent to fiber-coupled optical dosimeters is the fiber itself; more specifically, the radiation-induced generation of fluorescence and Cerenkov radiation in the fiber material. The main challenge of fiber-coupled optical dosimetry is therefore to separate the detected light signal corresponding to the dosimeter itself from the parasitic fiber contribution, the so-called stem effect or stem signal.

Inorganic materials

Crystalline compound materials such as copper-doped silica and carbon-doped aluminium oxide have been used for medical dosimetry purposes. Common to these materials is the emission of RL and/or OSL as a direct or indirect response to the ionizing radiation of a radiotherapy beam. Several methods have been presented in the literature for a medical dosimetry system based on fiber-coupled inorganic RL/OSL materials.

RL from copper-doped silica (SiO_2:Cu) was implemented for dosimetry purposes by Justus et al. (2004); the long lifetime of the RL was used to temporally filter out the stem signal from the optical fiber. This was achieved by applying a gating mechanism to the pulsed output of the linac, separating the RL signal from the much faster stem signal. A more independent gating mechanism was applied by Tanyi et al. (2010), to make the method insensitive to synchronization signal differences between different linacs. The method showed promising response characteristics for dose rate, energy and field size variations for several therapeutic MV x-ray beams.

Removal of the stem signal by temporal gating has also been used for the RL signal from Al_2O_3:C, as described by Andersen et al. (2006). Fiber-coupled Al_2O_3:C crystals have been studied extensively and investigated for applications in time-resolved IMRT verification (Andersen et al., 2006), mammography (Aznar et al., 2005), proton therapy (Andersen et al., 2007) and brachytherapy (Andersen et al., 2009). Fiber-coupled Al_2O_3:C crystals can be used both as passive (OSL) and active (RL) dosimeters, and exhibit high sensitivity and high spatial resolution. Here, the fiber cable functions both as a transmitter of the RL/OSL signal and as transmitter for the stimulating laser light in the case of OSL readout. OSL readout of Al_2O_3:C must be performed after each irradiation and is time consuming due to the long luminescence lifetime. Therefore, emphasis has been on using the crystals in RL mode for time-resolved dose measurements. However, certain corrections are necessary because the material has been known to be subject to sensitivity changes with absorbed dose (Damkjær et al., 2008), temperature dependence (Edmund and Andersen, 2007) and memory effects due to deep traps (Damkjær and Andersen, 2010).

Europium-doped potassium bromide (KBr:Eu) was suggested as a "near-real-time" OSL dosimeter in a study by Gaza and McKeever (2006). The OSL signal from the material has a component exhibiting short luminescence lifetime. Because of this, the dosimeter can be read out with short time intervals during irradiation, enabling time-resolved measurements free of the stem signal contribution. However, component-specific sensitivity changes

in the OSL signal complicates the method (Klein and McKeever, 2008).
A fast RL dosimetry system based on cerium- and samarium-doped strontium sulfate (SrS:Ce,Sm) was presented by Benoit et al. (2008a) and used for pulse-resolution dose measurements in radiotherapy beams (Benoit et al., 2008b). The RL of the Ce^{3+} phosphor decays in the matter of approximately 35 ns, and can therefore easily be used to resolve the dose delivery structure of the μs-duration radiation pulses delivered by most medical linacs. However, the fast RL decay makes stem removal by temporal gating impossible, since the RL signal and stem signal cannot be separated sufficiently. Thus, no attempt at actual dose measurements was made.

Organic materials

An organic scintillator is typically based on an aromatic polymer material (e.g. polystyrene and its derivatives) containing one or more fluorescent dyes. When exposed to ionizing radiation, the scintillator emit photons in the visible wavelength area. Hereby, organic scintillators can be used as fiber-coupled dosimeters. Although the method has largely been known since the early 90s (Beddar et al., 1992a,b,c), its potential for routine clinical use has not been exploited due to incomplete removal of the fiber stem signal. However, this situation has changed in the last couple of years. Recent studies have thus reported on calibration of polymer gel dosimeters (Archambault et al., 2006b), the development of two-dimensional scintillator arrays for IMRT QA (Lacroix et al., 2008), *in vivo* dosimetry using rectal balloons (Archambault et al., 2010), measuring perturbation factors for ionization chambers (Lacroix et al., 2010b), and dosimetry in small radiotherapy fields (Klein et al., 2010; Lambert et al., 2010). Brachytherapy applications have also been investigated (Lambert et al., 2006; Cartwright et al., 2009). Organic scintillators of any size can be attached to optical fibers, and therefore the spatial resolution of the dosimeter is in theory only limited by the measurement signal-to-noise ratio. The sensitivity of organic scintillators is inferior compared with inorganic materials like Al_2O_3:C, but makes up for this disadvantage with better water and tissue equivalence, as well as the ability for faster readout. Commercial organic scintillators typically have decay times in the ns range, making them ideal for pulse-resolved dose measurements in radiotherapy beams. As for the SrS:Ce,Sm-based inorganic phosphor, temporal gating cannot be used for stem signal removal since the decay time is too short. However, other methods can be used, as will be presented in section 2.3.2.
Exhibiting good water equivalence, mm-scale spatial resolution and μs-ms temporal resolution, fiber-coupled organic scintillators present a unique opportunity for pulse-resolved dose measurements in complex and dynamic radiotherapy beams. So far, no experimental studies have taken advantage of the fast response of commercial organic scintillators to measure doses de-

livered in radiotherapy beams on the actual timescale of the pulsed linac output. Furthermore, the use of organic scintillators have not to our knowledge been verified by direct comparison with Monte Carlo (MC) simulations of dose delivery in small radiotherapy fields. These two aspects of scintillator-based radiotherapy dosimetry are main focus points of this thesis. The choice of optical fibers and organic scintillators to obtain optimal light collection and detection efficiency is also a point of investigation. The performance of custom-made organic scintillators with long scintillation lifetimes will also be evaluated.

1.4 Thesis outline and objectives

The work summarized in this thesis describes the development and characterization of a dosimetry system based on fiber-coupled organic scintillators that can be used for quality assurance, verification and reference dosimetry of modern radiotherapy modalities. A preliminary version of the system was developed before the start of this PhD project (Beierholm, 2007; Beierholm et al., 2008), but served more as a proof-of-principle study than as a complete dosimetry system. From the start of this project and until now, the system has evolved from a coarse prototype towards a more refined, well-characterized and fully integrated system with enhanced accuracy and precision, as well as a much more detailed temporal and spatial resolution.

Chapter 2 deals with the theoretical aspects of fiber-coupled dosimetry, and describes the dosimetric characteristics of organic scintillators and optical fibers. The theoretical aspects of the stem effect are covered in section 2.3.1, while the various methods to remove or reduce the stem effect are described in detail in section 2.3.2.

Chapter 3 covers the overall experimental setup, describing the basics of radiation delivery from a medical linac and its subsequent detection using the newly developed dosimetry system.

Chapter 4 accounts for experiments made to investigate basic physical and dosimetric properties of fiber-coupled organic scintillators in general, and the new dosimetry system specifically. Studies of the stem effect and some basic clinical dosimetry are covered here.

Chapter 5 regards pulse-resolved dosimetry performed with the new dosimetry system. The measurements were made using an initial and a modified version of the data acquisition setup, and the results and performance of the two methods are discussed.

Chapter 6 deals with the application of the new dosimetry system for dosimetry of complex radiotherapy fields, such as the ones encountered in stereotactic radiotherapy and IMRT. The chapter presents small-field measurements made at AKH in Vienna in collaboration with the International Atomic Energy Agency (IAEA). After this study, we performed small-field measurements at Herlev Hospital to establish a comparison between the new dosimetry system and Monte Carlo calculations of dose delivery in small treatment fields.

Chapter 7 serves as the conclusion of this thesis, summarizing the main conclusions and findings of the project.

Chapter 8 presents a paper published in Radiation Measurements as part of the proceedings of the LUMDETR 2009 conference in Krakow. It describes the first successful experiences with a scintillator-based dosimetry system capable of measuring dose per pulse from a medical linac. The measurements show that the system exhibits satisfactory accuracy but poor precision for quantitative dose measurements of individual pulses. Never the less, the system proves capable of measuring qualitative changes in dose per pulse, such as the dose rate transient occurring at beam start-up.

Chapter 9 presents a paper accepted for publication in Physics in Medicine and Biology. It deals with the application of the new dosimetry system for dosimetry of complex radiotherapy involving high spatial and temporal dose gradients. It is briefly described how the detection hardware of the system has been refined, resulting in higher measurement precision and easier data acquisition. Small-field dose measurements are compared with Monte Carlo calculations, and good agreement within 2 % is found. Additionally, pulse-resolved dose measurements are explored further and compared with the ones presented in chapter 8.

Chapter 10 is a paper accepted for publication in Radiation Measurements as part of the proceedings of the SSD 16 conference in Sydney. The paper regards the use of organic scintillators with long luminescent lifetimes to remove the stem effect through temporal gating. A custom-made organic scintillator, in-house developed at Risø DTU, is compared with a commercial one with regards to luminescent lifetime and signal-to-noise ratio.

Chapter 2

The response of fiber-coupled organic scintillators to ionizing radiation

Before fiber-coupled organic scintillator probes can be used for dose measurements in a clinical setting, the material characteristics of the probes must be known. First of all, it is important to know the basic interaction mechanisms that exist between a beam of ionizing radiation and an absorbing medium, the latter being an optical fiber, a cylindrical piece of organic scintillator, a phantom made of solid water or a patient undergoing radiotherapy.

2.1 Interactions of ionizing radiation with matter

A beam of ionizing radiation will deposit energy in an absorbing medium in various ways, depending on the type of radiation. Photon radiation in the form of x-rays or gamma rays interact with the atoms of the absorber in an overall stochastic fashion, where a low number of interactions result in secondary particles (electrons) depositing energy in the medium. In contrary, charged particles like electrons or protons deposit their kinetic energy in the absorber continuously along the particle track, due to Coulomb forces between the charged particles and the nearby absorber atoms.

2.1.1 Photon radiation

A photon beam of MV x-rays passing through an absorbing medium is attenuated through indirect interactions with the of the absorber. The intensity I of the x-ray beam at a depth x into the medium can be approximated[1] by

---

[1] This is merely an approximation since equation 2.1 strictly applies for monoenergetic x-rays under conditions of good geometry.

the exponential relation

$$I = \exp(-\mu x) \tag{2.1}$$

where μ is the linear attenuation coefficient in a medium of thickness Δx:

$$\mu = \frac{\text{fraction of photons interacting in } \Delta x}{\Delta x} \tag{2.2}$$

However, it is common to use the so-called mass attenuation coefficient μ/ρ instead of μ in equation 2.1, with ρ the density of the absorbing medium. Mass attenuation coefficients are given in SI units of mg/cm^2. The dose is not deposited by the photon radiation directly, but by secondary charged particles that are generated by photon-absorber interactions. Depending on their energy, photons can interact with an absorbing medium through three processes: Photoelectric absorption, Compton scattering, and pair production. The interaction mechanisms are shown in a schematic form in figure 2.1. In this way, secondary charged particles are generated in three distinct processes. For the MV x-ray beams used in radiotherapy, Compton scattering is the dominant interaction process and dose is therefore deposited in the absorbing medium by secondary electrons.

For MV x-rays, the energy deposition with depth in the absorbing medium results in a distinct depth-dose profile. Figure 2.2 shows an example of percentage depth dose (PDD) for a 6 MV x-ray beam. Below the surface of the medium, the dose deposition rapidly rises to a maximum, beyond which the decay is exponential. The initial rise in dose deposition - called the build-up region - is caused by secondary electrons released in the medium through either of the interaction processes mentioned above, mostly by Compton scattering. The build-up region is also characterized by the absence of charged particle equilibrium (CPE). According to Attix (1986), CPE is fulfilled within a given volume when each charged particle of a given type (in this case, each secondary electron) and energy leaving the volume is replaced by an identical particle of the same energy entering the volume, in terms of expectation values. The build-up region and the depth of maximum dose deposition, d_{max}, are essentially defined by the finite range of the secondary electrons, and thus depend on the initial x-ray beam energy. The higher the mean energy of the incident x-rays, the longer the mean path length of the secondary electrons and the larger d_{max}.

2.1.2 Charged particle radiation

For electrons and other charged particles, interactions with the absorbing medium are usually described in terms of mean ranges and stopping powers. The mean range of a charged particle can be seen as a path length in the absorber. It is defined as the mean distance traversed by a charged particle beam in an absorber, at which the particle number in the beam drops to half its initial value. The stopping power is defined as the infinitesimal energy

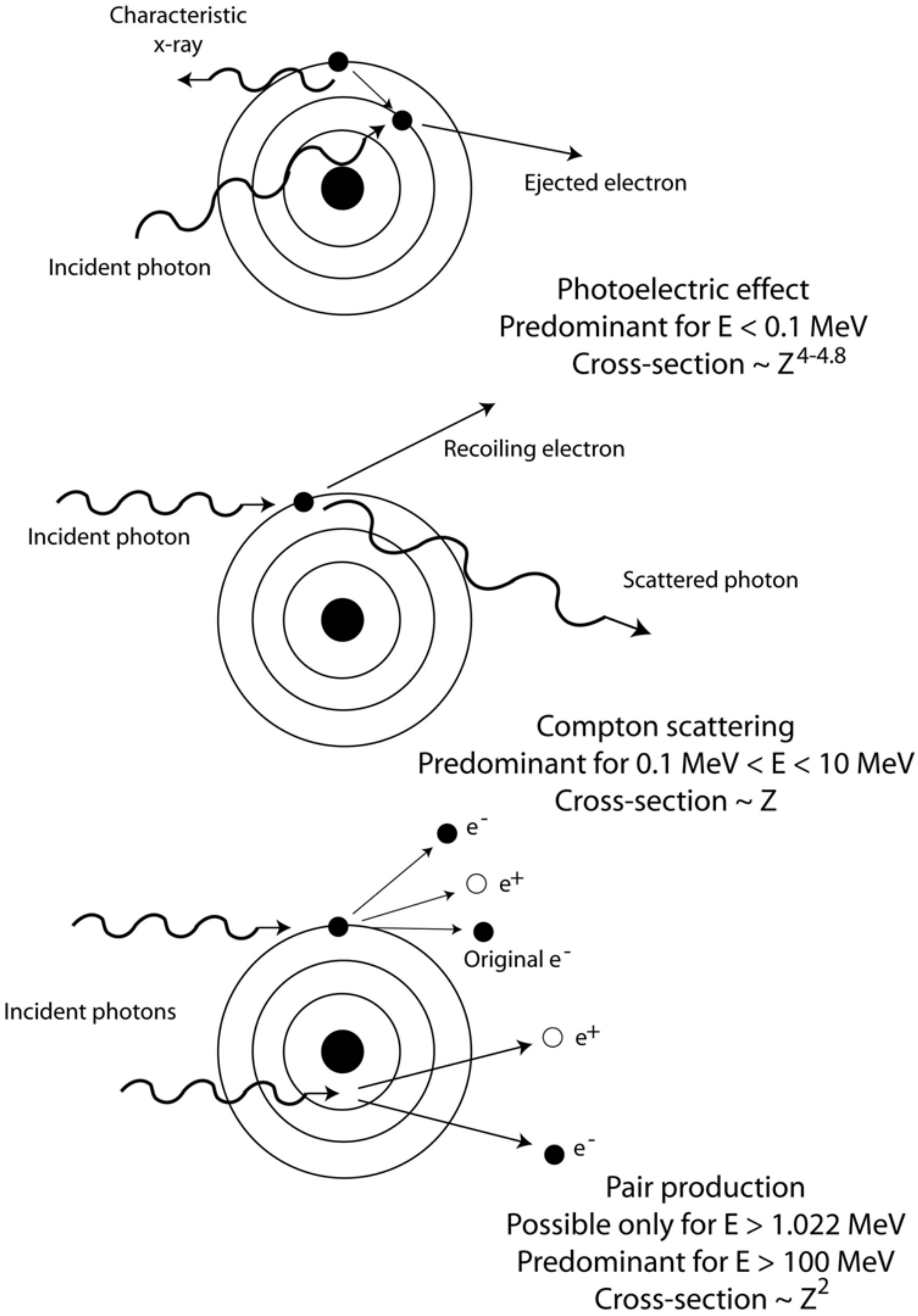

Figure 2.1: Schematic view of the three photon interaction processes photoelectric absorption, Compton scattering and pair production. Redrawn from Aznar (2005).

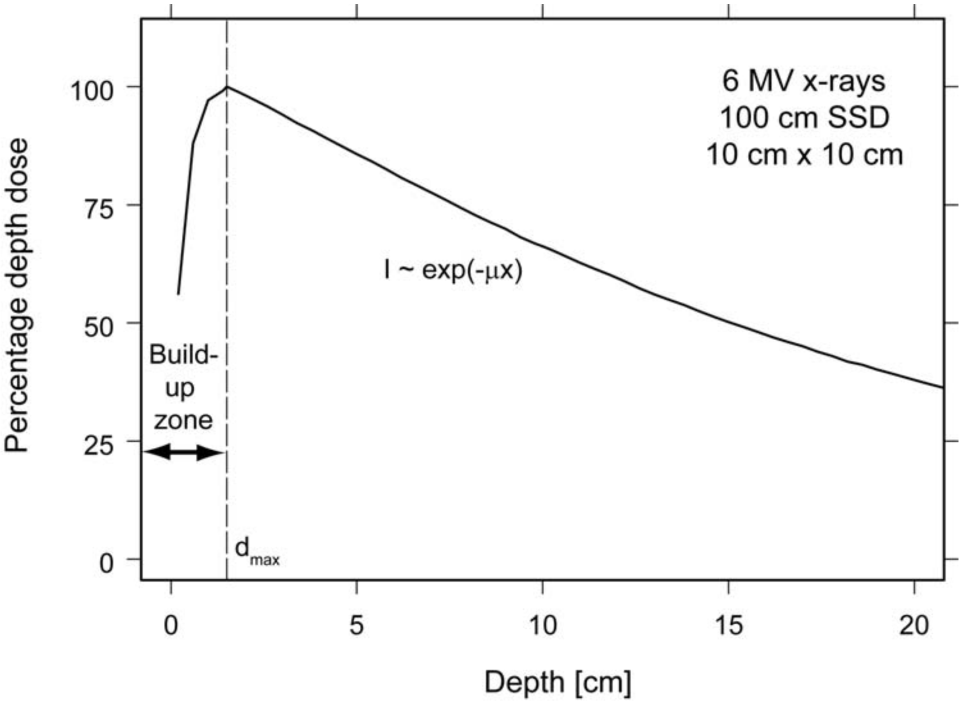

Figure 2.2: Example of a depth dose curve for photon radiation. Percentage depth dose for 6 MV x-rays in water, measured with a PTW 30013 Farmer® ionization chamber at Herlev Hospital. The measurements were performed at an SSD of 100 cm with a square field of 10 cm x 10 cm size. The dose deposition builds up to the depth of maximum dose before decaying exponentially.

loss dE, caused by inelastic collisions, of a charged particle traversing an infinitesimal length dx in the absorber:

$$S(E) = -\frac{dE}{dx} \tag{2.3}$$

The stopping power is energy dependent and increases with the distance traversed in the absorber, peaking approximately at the mean range and then rapidly falling to zero. This characteristic stopping power peak also represents a peak in dose deposition and is called the Bragg peak. Because the main energy deposition is very localized, the nature of the Bragg peak is exploited in radiotherapy using proton or heavy ion beams, where a very concentrated dose can be deposited at the exact location of a cancerous tumor in a patient with minimal exposure to the tissue in front of and behind the tumor. Radiotherapy using electrons is less expensive than proton or heavy ion therapy, but the depth dose curve lacks a discernable Bragg peak due to straggling of the individual electrons, causing a smearing of the collective depth-dose profile. Electrons have a relatively small range in water and tissue because of their low mass. For example, medical linacs can typically deliver electron beams of energies between 4 and 20 megaelectron volt (MeV). Using the continuous slowing down approach (CSDA) in the ESTAR program[2], 4 MeV monoenergetic electrons are found to have a range of 2.04 cm in water, while the corresponding range for 20 MeV monoenergetic electrons is 9.32 cm. Electron beams are therefore primarily used for treating superficial malignancies such as skin cancer. Protons and heavy ions have larger masses; therefore they penetrate deeper and are much less susceptible to straggling, and thus exhibit a distinct Bragg peak and a more localized dose deposition. Proton treatments are normally delivered using proton beams of many different energies to apply a spread out Bragg peak dose deposition profile to the tumor area. At this time, a total of 29 facilities worldwide deliver proton treatments, with emphasis on treating children because of the decreased risk of developing radiotherapy-induced secondary cancers later in life. Only 5 centers worldwide offer carbon ion treatments at this time.[3]

2.2 Dosimetric characteristics of organic scintillators

An organic plastic scintillator consists of i) a polymer matrix of aromatic hydrocarbons (the base) emitting ultraviolet light when exposed to ionizing radiation and ii) an organic fluorescent dye (the wavelength shifter) that is highly absorbing at short wavelengths and emits at longer wavelengths (e.g. visible blue or green). When the polymer base is subject to ionizing radiation, the aromatic molecules are excited from the ground energy state. As a mode of de-excitation, the molecules emit short-wave UV light. The polymer base therefore serves as a primary scintillator; however, most polymer materials exhibit a large degree of overlap between absorption and emission bands. This severely limits the number of photons escaping from the material. To circumvent this problem, a wave shifter is introduced as a dopant in the polymer base, resulting in a scintillation Stokes-shift towards wavelengths in the visible area, where the degree of self-absorption is much less severe. In commercial organic scintillators, the scintillation process mostly occurs through singlet transitions and is therefore very fast, on the order of nanoseconds. Organic scintillators with longer decay times can however be engineered by making the emission of scintillation light occur through a triplet transition.

This section covers physical parameters that are relevant to the use of any dosimeter material in radiotherapy beams. The water equivalence of a dosimeter regards how the material responds to the radiation field com-

---

[2] Source: http://physics.nist.gov/PhysRefData/Star/Text/ESTAR.html

[3] Source:http://ptcog.web.psi.ch/ptcentres.html

pared to water, as well as how the presence of the dosimeter in a homogenous water medium perturbs the radiation fluence. Energy dependence concerns to what degree measurements made with the dosimeter are influenced by changes in the energy spectrum of the radiation beam. temperature dependence concerns how temperature changes in the ambient medium influence the dosimeter response. Resistance to radiation-induced damage shows how the sensitivity or output of the dosimeter material degrades with absorbed dose. Finally, angular dependence shows how sensitive the dosimeter is to changes in the orientation between the dosimeter and the radiation beam.

2.2.1 Water equivalence

In medical dosimetry, water has always been the chosen reference material and substitute for living human tissue. Therefore, routine QA measurements are typically performed in homogenous water. If a dosimeter is highly water equivalent, the perturbation of the radiation fluence due to the presence of the dosimeter in a water tank is minimized. Depending on the radiation field, there are different physical parameters that quantifies the water or tissue equivalence of a dosimeter material. For low energy x-rays typically used in diagnostics, the effective atomic number (Z_{eff}) is the parameter that best describes water equivalence of a compound material. The atomic number is defined as

$$Z_{eff} = \sqrt[m]{a_1 Z_1^m + a_2 Z_2^m + ...} \tag{2.4}$$

Here, the exponent m is an energy-dependent number, covering the range from 3-4 (kV range x-rays) to 1 (MV range x-rays). Z is the atomic number of the individual element while a is the element-specific ratio of the number of electrons to the total number of electrons. A thorough description of the effective atomic number concept can be found in Johns and Cunningham (1983). The organic scintillators used during this project are polystyrene based. The chemical formula of polystyrene is $-(C_6H_5CH - CH_2)_n-$. this means that carbon ($Z = 6$) contributes $8 \times 6 = 48$ electrons, while hydrogen (Z=1) contributes $8 \times 1 = 8$ electrons. The effective mass number of polystyrene can then be calculated:

$$Z_{eff}(polystyrene) = \sqrt[m]{(48/56) \times 6^m + (8/56) \times 1^m} \tag{2.5}$$

For x-ray energies relevant to diagnostic radiology procedures like CT, $3.4 < m < 3.8$ yielding a Z_{eff} of approximately 5.7. For MV-range radiotherapy beams, $m = 1$ and $Z_{eff} = 5.3$. For comparison, Z_{eff} for water is approximately 7.5 for the diagnostic x-ray energy range and 6.6 for the MV energy range.

Another measurable quantity governing the water equivalence of a dosimeter material is the mass-energy absorption coefficient μ_{en}/ρ. The mass-energy absorption coefficient of a material exposed to photon irradiation of a given energy is given as

$$\frac{\mu_{en}}{\rho} = \frac{\mu}{\rho} \cdot \frac{\overline{E}_{ab}}{h\nu} \tag{2.6}$$

where μ/ρ is the mass attenuation coefficient introduced in section 2.1.1, $\overline{E}_{ab}$ the average energy absorbed per interaction and $h\nu$ the photon energy. For MV x-rays delivered in radiotherapy beams, Compton scattering is the dominant interaction mechanism between the indirectly ionizing radiation and the absorbing medium. Because of this, μ_{en}/ρ is arguably a better representative for water equivalence than Z_{eff} in this energy range. This is because the cross section for Compton scattering is less dependent on atomic number compared with photoelectric absorption, which dominates at diagnostic energies. Beddar et al. (1992b) compared mass-energy absorption coefficients of a polyvinyltoluene-based scintillator to those of water and polystyrene for monoenergetic photons in the keV-MeV energy range. Good agreement between water and polystyrene was observed in the MeV range (see figure 2.3, upper part). Other physical parameters that can be used to quantify water equivalence are mass-collision stopping powers and electron densities. ICRU (1984) stated good agreement between polystyrene and water when comparing mass-collision stopping powers for monoenergetic electrons in the 1-50 MeV range. This agreement is also found in the bottom part of figure 2.3. Polystyrene has an electron density of 3.238×10^{23} electrons per gram. By comparison, the electron density of water is 3.343×10^{23} electrons per gram.

2.2.2 Energy dependence

The energy of the incident ionizing radiation influences the dosimetric response of organic scintillators in two ways: The efficiency of the scintillation process, and the dose absorption relative to a reference material (i.e. water).

Scintillation efficiency

A recent study by Frelin et al. (2008a) regarded intercomparison experiments performed for different polystyrene- and polyvinyltoluene-based commercial organic scintillators. The study showed that the sensitivity of all scintillators could be considered energy independent (within a 5 % tolerance) for electron energies above 100 keV and for photon energies above 200-250 keV. These values are generally confirmed in the litterature (Nowotny, 2004; Williamson et al., 1999). The reduced sensitivity of organic scintillators to low-energy ionizing radiation is generally known as quenching, and is a consequence of high ionizing density; when the charged particles or photons are of low energy, the radiation energy is deposited within a small volume, leading to a quenching effect in the scintillator matrix. This is in principal not an

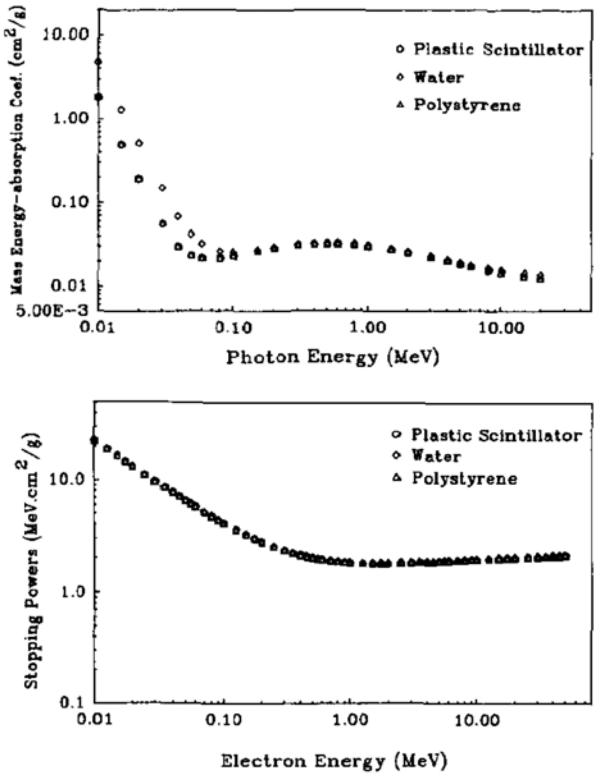

Figure 2.3: Top: Mass-energy absorption coefficients versus photon energy for a polyvinyltoluene based plastic scintillator, water and polystyrene (logarithmic scale). Bottom: Mass-collision stopping powers versus electron energy for the same three media (logarithmic scale). Source: Beddar et al. (1992b).

issue when the dosimeters are placed in the primary radiation field, but will have an effect for measurements out of field where the contribution from low energy scattered photon radiation is significant.

Dose absorption

The response of polyvinyltoluene-based organic scintillators to higher energy photons have been investigated using Burlin cavity theory (Beddar et al., 1992b; Clift et al., 2000b) and Monte Carlo simulations (Beddar et al., 2005). The Burlin cavity studies reported a change in the ratio between absorbed dose to the scintillator and absorbed dose to water of 0.8 % for photon energies from 200 keV to 20 MeV. Similarly, the Monte Carlo study reported a change in the ratio within 1.0 % for energies from 500 keV to 20 MeV.

2.2.3 Temperature dependence

Beddar et al. (1992b) investigated the temperature dependence of fiber-coupled polyvinyltoluene-based organic scintillators by immersing one in water and subjecting it to 4 MV x-rays from a medical linac for temperatures between 0 and 50 °C. No significant difference from overall measurement uncertainty could be observed, and it was therefore concluded that the scintillator probe under study could be considered temperature independent in a clinically relevant temperature range. A similar experiment was performed by Lambert et al. (2007), which reported a temperature dependence of 0.1 %/°C or lower. Even though these experiments were performed only for polyvinyltoluene-based scintillators, it has implicitly been assumed that temperature independence applies to organic scintillators in general. Hence, no experiments have been performed to verify the temperature independence of polystyrene-based scintillators, although the manufacturers state that their products are usable in the temperature range from -20 to +50 °C (Saint-Gobain, 2005).

2.2.4 Resistance to radiation-induced damage

In the context of scintillation dosimetry, radiation-induced damage is defined as a decrease in scintillator light output with absorbed dose. The effect can be either permanent or non-permanent. Beddar et al. (1992b) reported on radiation-induced sensitivity decrease for the polyvinyltoluene-based scintillator under study when subjecting it to large doses of Cesium-137 gamma rays. A sensitivity reduction of 2.8 % was measured after a total delivered dose of 10 kGy. Busjan et al. (1998) reported on radiation damage effects in a polystyrene-based scintillator. It was argued that the decrease in scintillator sensitivity was caused by the non-permanent formation of absorption centers in the polystyrene. These centers seemed to be formed primarily in the visible blue area, with a large degree of overlap between the resulting absorbtion spectrum and the emission spectrum of the scintillator. The presence of oxygen was found to have an effect on the formation of the absorption bands and the subsequent sensitivity recovery. A sensitivity decrease of 3.5 % in the presence of oxygen was evident after irradiating the scintillator with 100 kV x-rays for a total dose of 2.4 kGy. The degree of sensitivity change was seen to be far greater in an oxygen-free environment, amounting to 19 % for the irradiation procedure. A study by Wick and Zoufal (2001) showed that radiation-induced sensitivity changes are apparently more severe for the absorption of low doses than for high doses, indicating a saturation behavior of the radiation-induced damage.

2.2.5 Angular dependence

According to the IPEM Report No. 103 (IPEM, 2010), the response of any dosimeter should ideally be independent of the irradiation angle to within ± 0.5 % for a ± 60° angular variation. In reality, however, most detectors do not have an isotropic response. To circumvent this problem, dosimeters are generally used in the same geometry as that in which they are calibrated, which is with the dosimeter axis parallel to the gantry rotation axis (IAEA, 2005).

Due to the construction of a fiber-coupled organic scintillator, some degree of directional dependence is expected due to the stem signal generated in the fiber (see next section). Therefore, a test of directional independence is also a test of the completeness and accuracy of stem signal removal.

Lambert et al. (2006) examined the angular dependence of a 1 mm diameter fiber-coupled BC-400 scintillator when used for high dose rate brachytherapy dosimetry. The measurement values obtained varied no more than 2 % when the angle between the fiber and a ^{192}Ir source was varied between -150° and 90°. The measurements were however not corrected for the fiber stem signal, as this was perceived as insignificant under the given irradiation conditions.

An angular dependence test was performed by Archambault et al. (2007) for a fiber-coupled BCF-12 scintillator of 1 mm diameter. The fiber-coupled scintillator probe was inserted in a small spherical phantom, oriented in such a way that the scintillator was at the center of the phantom and the fiber was perpendicular to the linac gantry rotation axis. Exposing the probe to 6 MV x-rays from different angles led to a measurement variation of no more than 0.6 % when the stem signal from the fiber was corrected for. This shows that fiber-coupled organic scintillators are in principal angular independent, provided that the parasitic light signal from the optical fiber is corrected for.

2.3 The nature of the stem effect

When a light-guiding optical fiber is subject to ionizing radiation, light is generated in the fiber material itself. This is called the stem effect or stem signal because of the resulting enhanced light signal from the fiber and scintillator probe; a ”stem” is super-imposed on the light signal from the scintillator, as depicted in figure 2.4. Because of the stem effect, it is hardly possible to distinguish the scintillator signal from the parasitic fiber signal. Therefore, the stem effect poses a serious problem to the use of organic scintillators for radiotherapy dosimetry because of a decrease in the signal-to-noise ratio. In addition, the amount of light coming from the fiber is dependent on the amount of fiber in the radiation field, yielding large systematic errors when the field size or the position of the scintillator relative to the field changes significantly.

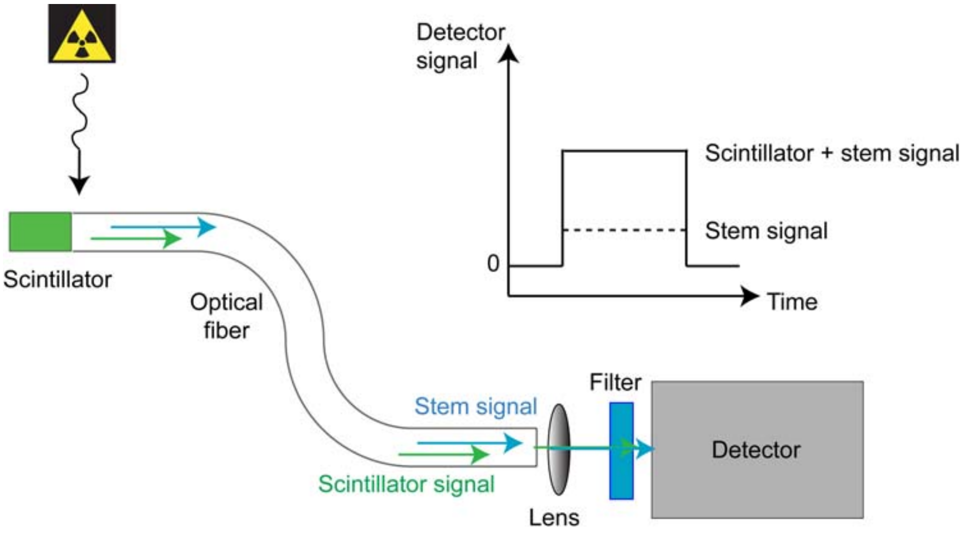

Figure 2.4: Schematic view of how Cerenkov radiation and fiber fluorescence enters into the total detected light signal as a stem effect.

2.3.1 Origin of the stem effect

Different physical processes contribute to the stem effect. In the literature, these are often separated into two main contributions: Fluorescence and Cerenkov radiation.

Fluorescence is a process similar to scintillation. In the case of optical fibers, fluorescence is believed to be caused by fiber impurities such as oxygen molecules (i.e. because of water abundance). The impurity molecules absorb the radiation energy from charged particles and photons, emitting Stokes-shifted photons as a means of de-excitation.

Cerenkov radiation is emitted whenever a charged particle traverses a medium with a velocity higher than the velocity of light in that medium (Jelly, 1958). This can be the case for charged particle as well as photon irradiation; in the latter case as a result of secondary electron generation. In general, a charged particle passing through a dielectric material will briefly change the electromagnetic field in the vicinity of the particle track, hereby polarizing the atoms in the medium. As a result of the polarization, radiation is emitted as the atomic electrons return to equilibrium and the atoms are depolarized. In most cases, the radiation wavefronts are out of phase with each other and the net radiation is canceled out by destructive interference of the waves. However, if the charged particle velocity is higher than the phase velocity of light in the medium, the radiation waves can interfere constructively. This corresponds to the condition $v > c/n$ or $n\beta > 1$, where n is the refractive index of the medium and $\beta = v/c$ is the velocity of the particle in the medium relative to that of light in vacuum. Cerenkov radia-

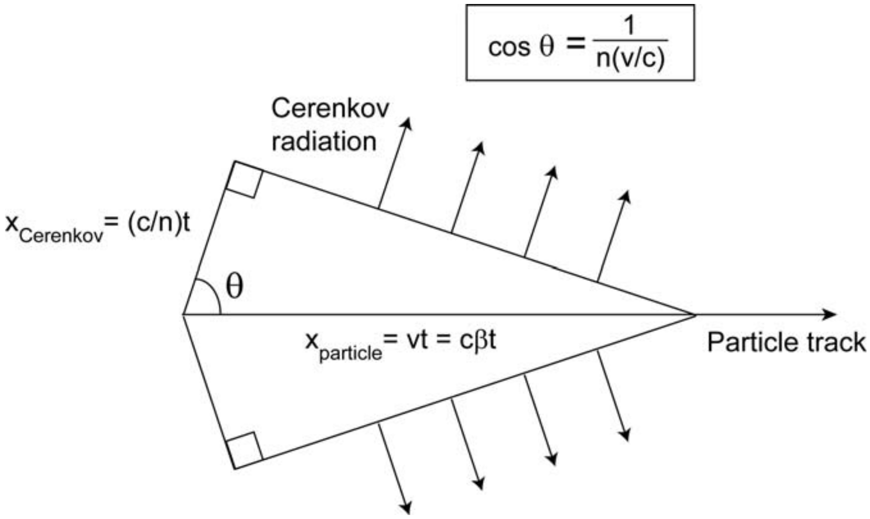

Figure 2.5: Schematic view of Cerenkov light generation in a dielectric medium. When a particle of velocity $v > c/n$ traverses a medium of refractive index n, Cerenkov radiation is emitted in a cone of half angle θ with velocity c/n.

tion is therefore only generated for particles having energies above a certain threshold, E_{thresh}:

$$E_{thresh}\ (\text{keV}) = \frac{511\ \text{keV}}{\sqrt{1-(v/c)^2}} - 511\ \text{keV} \tag{2.7}$$

For most commercial optical fibers, this corresponds to an E_{thresh} of approximately 180-190 keV.

The Cerenkov radiation is dominant in the UV and visible blue wavelength areas, exhibiting a distinct $1/\lambda^3$ dependence. There is a Cerenkov cutoff in the x-ray wavelength area, since here $n < 1$. The radiation is emitted in a cone of angle $\theta = \arccos(1/n\beta)$ relative to the propagation direction of the charged particle, as seen in figure 2.5. Since light is guided in an optical fiber by the process of total internal reflection, the amount of Cerenkov radiation collected in the fiber will be angular dependent, as illustrated in figure 2.6. Therefore, the intensity of detected Cerenkov radiation depends not only on the energy of the ionizing radiation and the amount of optical fiber irradiated, but on the angle between fiber and radiation beam as well[4]. To be more specific, the Cerenkov intensity produced by an electron beam of given flux density is proportional to $1 - 1/(n\beta)^2$.

Measurements concerning Cerenkov radiation emission from different kinds

---

[4] In the case of x-rays, the direction of the generated secondary electrons is not well defined. As a result, Cerenkov radiation is emitted isotropically and the Cerenkov intensity is virtually angular independent.

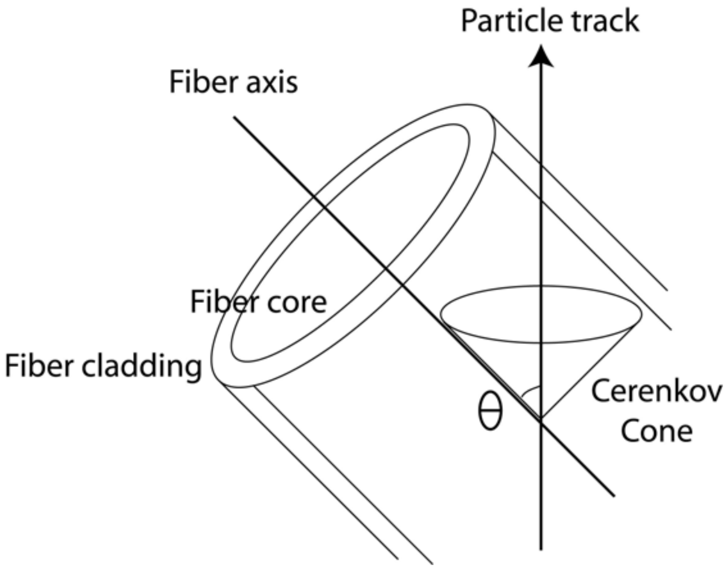

Figure 2.6: Schematic view of Cerenkov light generation in an optical fiber. The light is emitted in a cone of half angle θ. Redrawn from Beddar et al. (2004).

of light guides were presented in Beddar et al. (1992a). This paper concluded that Cerenkov radiation was the dominant cause of the stem effect when using MeV electron beams, fiber fluorescence being negligible in comparison. The study focused on multimode, step-index fibers made of fused silica (SiO_2), although polystyrene, PMMA and water were also used as fiber materials. Cerenkov intensity and angular dependence was examined by irradiating the fibers with 6 and 12 MeV electrons delivered by a Varian Clinac$^{®}$ 1800. The resulting light generated in the fiber was detected with a Hamamatsu R1635 photomultiplier tube (PMT). The fiber-beam angle of maximal Cerenkov intensity was generally close to 45° in the MeV energy range; approximately 44° for silica, approximately 52° for polystyrene, and approximately 37° for liquid water-core light pipes. This coincided fairly well with the theoretical considerations since e.g. $n = 1.46$ for silica corresponds to a Cerenkov emission angle of $\theta = \arccos(1/n\beta) = 46.6°$ for an electron beam energy of 6 MeV and 46.7° for a 12 MeV beam energy. Similarly, minimal Cerenkov radiation reaches the detector when the radiation beam is perpendicular to the fiber axis (i.e. at a 90° fiber-beam angle). The measurements reported in the paper indicated little or no contribution from fiber fluorescence, and it was therefore concluded that Cerenkov radiation was the dominant cause of the stem effect when irradiating optical fibers with MeV-energy electrons.

In a study by de Boer et al. (1993), spectral measurements of the stem signal were performed using silica fibers exposed to i) 20 MeV electrons from a Varian Clinac® 2100C and ii) 125 kV x-rays from a Phillips RT-250 orthovoltage unit. The resulting emission spectra from the silica fibers were obtained using a Hamamatsu R1463 PMT combined with a Digikrom 240 scanning monochromator. This study showed that although Cerenkov radiation was dominant for MeV-energy electrons, a contribution from fiber fluorescence was also evident (approximately 5 % of the maximal generated Cerenkov intensity). This was seen when comparing fiber emission spectra from 20 MeV electron irradiations at 90° fiber-beam angle with the ones of 125 kV x-ray irradiations; both corresponding to situations where the Cerenkov effect is minimal. The spectra where similar, indicating that the process responsible was the same. Spectra obtained when irradiating the fibers with 20 MeV electrons at 45° and 90° fiber-beam angles showed an expected $1/\lambda^3$ wavelength dependence for the Cerenkov effect. The fiber fluorescence spectrum was found to lie in the visible blue and green wavelength area between 400 and 550 nm, with peak emission at approximately 455 nm.

Similar results were presented by Clift et al. (2000a), using a polystyrene-based optical fiber exposed to bremsstrahlung x-rays generated from a 20 MeV electron beam at the ARPANSA Laboratory, Melbourne. A mathematical model, predicting the contribution from Cerenkov radiation to the overall light signal from a fiber-coupled scintillator probe, was also presented.

One study (Arnfield et al., 1996) dealt with the concept of fiber-coupled organic scintillators for use in brachytherapy. The paper reported on the testing of five kinds of silica optical fibers - four of these exhibiting high OH content and one being "low-OH". The OH content of a fiber has an influence on the transmission spectrum as well as susceptibility to radiation damage. The fibers showed contributions from both fiber fluorescence and Cerenkov radiation when subject to photon radiation from a ^{192}Ir high dose rate (HDR) brachytherapy source of 380 keV mean energy. The most surprising result of the study was the high light output of the low-OH fiber, which exhibited by far the largest degree of fiber luminescence. Apart from this, the observed Cerenkov and fluorescence spectra where in general accordance with the ones obtained by de Boer et al. (1993). It was also clarified that the observed light originated in the fiber core and not in the cladding; no significant difference in luminescence intensity was observed when irradiating fibers with and without cladding.

A thorough mathematical analysis of the coupling between scintillator and optical fiber was performed in Beddar et al. (2004). Through geometrical considerations it was shown that the intensity of Cerenkov radiation captured in the fiber not only depends on the electron energy, but also the refractive index of the fiber core n_{core} and that of the cladding n_{clad}, as well as the difference between them $\triangle n$:

$$I_c \propto \frac{2}{\pi} \arcsin\left(\sqrt{\frac{n_{co}\triangle n}{2(n_{co}^2-1)}}\right) \times \left(1-\frac{1}{n_{co}^2\beta^2}\right) \tag{2.8}$$

In the case of electrons of relativistic energies, $\beta \simeq 1$ and the captured Cerenkov intensity becomes independent of electron energy. When regarding the coupling of scintillation light into the optical fiber, the fiber acceptance angle ϕ_A depends on the refractive indices of scintillator, fiber core and fiber cladding:

$$\sin\phi_A = \frac{\sqrt{2n_{co}\triangle n - \triangle n^2}}{n_{sci}} \tag{2.9}$$

with n_{sci} the refractive index of the scintillator. The refractive index difference $\triangle n$ thus have a large influence of the light collection efficiency of the fiber, concerning scintillation as well as Cerenkov radiation. This expression is analogous to the definition of the numerical aperture (NA), given by

$$NA = \sqrt{n_{core}^2 - n_{clad}^2} \tag{2.10}$$

Efficient collection of light from the scintillator into the fiber core necessitates matching the NA of the scintillator to that of the fiber.

The matter of whether Cerenkov radiation is the dominant physical process responsible for the stem effect is not fully resolved. A paper by Marckmann et al. (2006) reported that fluorescence, not Cerenkov radiation, dominated the stem effect generated in five commercial PMMA and silica fibers when exposed to MeV electrons. This is in contradiction to the results presented by Beddar et al. (1992a) and de Boer et al. (1993). Furthermore, the fluorescence spectra observed by Marckmann et al. (2006) peaked at approximately 360 nm for all fibers. This was explained to be a result of water abundance in the fibers, although the spectra were not consistent with the ones presented by de Boer et al. (1993) and Clift et al. (2000a).

A study by Nowotny (2007) focused on the luminescence from ten different kinds of optical fibers when these were exposed to x-rays from a Siemens Polydoros 50S clinical x-ray device (up to 150 kV tube voltage). The core of the fibers studied was of either polystyrene, PMMA, high-OH silica or low-OH silica. Of all fibers, a low-OH silica fiber (Thorlabs BFL48-1000) was found to exhibit the largest radioluminescence response, closely followed by two polystyrene fibers of the wavelength shifting type (Saint-Gobain BCF-91A and BCF-92). Low-OH silica fibers should therefore not be used in medical dosimetry. This statement is further underlined in section 4.1.1.

2.3.2 Ways to eliminate the stem effect

Several methods have been proposed for correcting the scintillation signal for the parasitic stem effect. The possible correction methods can generally be separated into three overall methods: background subtraction using dual fibers, spectral discrimination, and temporal discrimination. A summary of the different methods will be given in this section.

Background subtraction

The so-called dual-fiber method was introduced in Beddar et al. (1992b,c). This method involves two optical fibers bundled together, each attached to a separate PMT. One fiber (the "background fiber") dose not have a scintillator attached to it, and thus only the contribution from the stem effect is detected. This contribution is then to be subtracted from the signal from the scintillator-coupled fiber, giving only the signal from the scintillator. The most obvious drawbacks of using two fibers are decreased spatial resolution and the need for gain balancing the two PMTs. Furthermore, the method fails in situations where the dose absorbed in the two fibers are not the same. In applications involving large dose gradients, such as IMRT or stereotactic radiotherapy, unacceptable over- or underestimations of the dose absorbed in the scintillator will be induced when the two fibers are subject to different dose distributions. Never the less, the dual-fiber method has been implemented in small-field applications such as stereotactic radiosurgery (Létourneau et al., 1999) and opthalmic plague dosimetry (Flühs et al., 1996).

Simple spectral filtration

Spectral filtration as an approach to stem effect correction was presented by de Boer et al. (1993). Spectral analysis of fiber fluorescence and Cerenkov emission, as described in section (2.3.1), motivated the idea of using optical interference filters to attenuate the part of the electromagnetic spectrum where the stem effect is dominant. If the scintillator and fiber spectra are sufficiently separated, this method could theoretically be used to correct for the stem effect and improve the signal-to-noise ratio. To accomplish this, several commercial organic scintillators were used, with different concentrations of wavelength-shifting fluors for emission in the visible blue, green and yellow spectrum.

The blue-emitting Bicron® BC-400 and orange-emitting BC-430 were used along with the custom made orange-emitting BC-430-SR and green-emitting BC-499-37, BC-499-49 and BC-499-50. The BC-430 exhibited incomplete wavelength shifting, with the emission spectrum smeared out over the entire visible wavelength area. This was caused by a too low concentration of wavelength shifting fluors (0.2% by mass), as was evident from the higher concentration of fluor and more completely shifted emission spectrum of the non-commercial BC-430-SR type (0.6% by mass).

The three yellow-emitting scintillators also had different fluor concentra-

tions, with the BC-499-50 showing chemical saturation at 1.5% by mass fluor concentration, and thus the best wavelength shifting achievable. The different scintillators were attached to silica optical fibers. Irradiating the fiber probes with 20 MeV electrons for different field sizes and 90° fiber-beam angle, the light from scintillator plus fiber was detected with a PMT with and without optical filters. The best results were obtained when combining the orange-emmiting BC-430-SR ($\lambda_{peak} = 580$ nm) with a 530 nm long pass filter; this gave a stem effect contribution of 2.8% of the scintillator signal per cm of irradiated fiber. Slightly poorer was a combination of the green-emitting BC-499-50 ($\lambda_{peak} = 530$ nm) and a 495 nm long pass filter, giving a 3.5% stem-to-scintillation ratio per cm of irradiated fiber. However, since 10 cm of irradiated fiber will result in a stem effect contribution of at least 28%, the presented filtration method is not sufficient for stem effect reduction in clinical beams where the field size, and hereby the amount of fiber irradiated, can vary considerably.
Spectral filtration of the stem effect was studied further in Clift et al. (2000a). In addition to interference filters, various coating materials were applied to the scintillator distal end to improve scintillation collection and signal-to-noise ratio. Bicron® BC-428 and BC-430 organic scintillators were attached to polystyrene optical fibers and irradiated with 20 MeV electrons in a water phantom. The light from the probes were detected with RS BPW-21 and UDT PIN 6DPI photodiodes, and a Cerenkov and fluorescence radiation (CFR) probe was used to measure the stem signal contribution. The low sensitivity of photodiodes compared with PMTs was compensated for by using scintillators and fibers of 5 mm diameter. Titanium Oxide (TiO_2) was found to be the most efficient reflective coating. Furthermore, a 3% CFR-to-scintillator contribution was reported when using the orange BC-430 scintillator combined with OG-530 and BG-40 band pass filters for a circular electron beam of 12 cm diameter. However, measurements involving large field sizes would still give a significant stem effect contribution, and it is uncertain how the high effective atomic number of a coating material like TiO_2 will affect the water equivalence of the organic scintillator.

Temporal gating

Time-based stem effect removal was introduced by Clift et al. (2002), using an organic scintillator with a long luminescence decay time - the Bicron® BC-444G. The method takes advantage of the rapid decay of Cerenkov and fiber fluorescence radiation (a few ns) compared to the scintillation from the BC-444G ($\sim$ 260 ns). Through the application of a pulsed linear accelerator and a gating algorithm, the light from fiber and scintillator is detected shortly after each radiation pulse. In this way, a large part of the scintillator signal will still be detected, while the rapidly decaying stem effect contribution will not. There are three drawbacks to the method: (i) it can only be applied for pulsed beams; this is not a big loss, however, since most radiotherapy treatments are performed using linacs. (ii) The BC-444G is custom made. Most commercial plastic scintillators exhibit time constants in the nanosecond range, and are thus too fast for temporal gating to be successful. (iii) As is the case for simple spectral filtering, at the cost of overall signal-to-noise improvement the scintillator signal is reduced.

Hollow-core fiber light guidance

Lambert et al. (2008) introduced the concept of a 1 m long hollow silver-coated capillary tube guiding the light from the scintillator to the optical fiber. This setup was shown to essentially eliminate the stem effect normally generated within the first 1 m of optical fiber while still transmitting an adequate signal from the scintillator. Light guidance in air is an appealing concept since no Cerenkov radiation is generated in an air-core light guide; Because no fluorescence is expected, the stem effect can in principle be circumvented entirely. In the case of Lambert et al. (2008), the air-core light guide was a rigid silica tube silver-coated on the inside for better light transmission. A Bicron® BC-400 blue-emitting organic scintillator was inserted in one end of the silica tube, while an optical fiber transmitted the radiation-induced light signal from the other end of the tubing to the photodetector. The proposed method yielded depth dose measurements that agreed within 1.5 % with ionization chamber measurements for 6 MV x-rays; for 9 MeV electron beams, the agreement was within 3.0 %. The concept has since evolved, and a study which characterizes the air-core dosimeters in small field and dynamic dose delivery applications has been published recently (Lambert et al., 2010). The main disadvantage of the method is the considerable signal loss to be expected when guided through a 20 cm long hollow tube.

An alternative approach to stem signal-free light guidance is the use of hollow-core photonic crystal fibers (Russell, 2006). However, since the physical principles behind photonic band gap guidance restrains the dimensions of the fiber, it is unlikely that a hollow-core fiber of sufficient diameter (0.5-1.0 mm) can be produced. Therefore, a hollow-core fiber might function as an example for stem signal-free light guidance, but the fiber core will likely be too small to be practical for applications involving organic scintillators of mm-size.

Chromatic removal

For this project, we have adapted the so-called chromatic stem removal method to our new dosimetry system. The chromatic removal method is a further development of the simple spectral filtration method, and has so far yielded promising results for removal of Cerenkov radiation and fiber

Table 2.1: Chromatic removal calibration procedures investigated in the study by Guillot et al. (2011).

Procedure		Calibration measurements
A	No. 1	Scintillator in isocenter of reference field Fiber straight
	No. 2	Scintillator in isocenter of large field Fiber curled up in field
B	No. 1	Scintillator in isocenter of reference field Fiber straight
	No. 2	Scintillator in isocenter of large field Fiber straight
C	No. 1	Scintillator in isocenter of reference field Fiber straight
	No. 2	Scintillator in isocenter of large field Fiber straight
	No. 3	Scintillator in isocenter of large field Fiber curled up in field
D	No. 1	Scintillator in isocenter of reference field Fiber straight
	No. 2	Scintillator out of field Fiber straight through field

fluorescence. The overall idea is that a spectral separation of fiber light and scintillator light is followed by a mathematical analysis of the two signal components. Optical components such as 45° dichroic mirrors are used to separate the total light signal into two wavelength bands: one dominated by the light from the scintillator, the other dominated by Cerenkov radiation and fiber fluorescence. In the original approach presented by Fontbonne et al. (2002) and Frelin et al. (2005), a green-emitting scintillator (Saint-Gobain BCF-60) was used, combined with yellow and magenta dichroic mirrors to discriminate the light signal into a blue, fiber-dominated detected signal A and a green, scintillator-dominated signal B[5]. Following this approach, the dose D absorbed in the scintillator would be given by the relation $D = a \cdot A + b \cdot B$. The unknown constants a and b are calculated by calibrating the dosimeter probe at known delivered dose for two different irradiation conditions: (i) an irradiation with a small amount of the fiber in the radiation field, to minimize the generation of Cerenkov light and fiber fluorescence; (ii) an irradiation involving as much fiber in the radiation field as possible to maximize the stem effect. From these measurements, a and b can be found from the detected signals in the two channels, and from the known doses:

$$D_1 = a \cdot A_1 + b \cdot B_1 \tag{2.11}$$

---

[5] in the original paper, the stem signal component was designated B (for blue) and the scintillator component G (for green)

for the minimized stem configuration, and

$$D_2 = a \cdot A_2 + b \cdot B_2 \tag{2.12}$$

for the maximal stem configuration. It is stated in Fontbonne et al. (2002) that the constants a and b are independent of beam energy, and apart from MV-energy x-rays the method has also been applied to electron beams. In Archambault et al. (2006a), chromatic removal is reported to be superior to background subtraction and simple filtration. It is however unclear how well the method performs if scintillator and fiber emission spectra are not well separated. Archambault et al. (2006a) reports the use of a blue-emitting BCF-12 scintillator, even though the scintillation spectra has a large degree of overlap with the fiber fluorescence and Cerenkov spectra. A similar setup was used in Beierholm et al. (2008), but the resulting depth-dose curves indicated some degree of field size dependence due to erroneous stem signal suppression.

A very recent study by Guillot et al. (2011) elaborated on the experimental conditions that must apply for the chromatic removal procedure to be correct. The theoretical expression of the measured dose given as a linear combination of two signal contributions A and B is further elaborated, so that

$$D = a \cdot A + b \cdot B = a\left(A + \frac{b}{a} \cdot B\right) \tag{2.13}$$

where a is defined as the so-called gain factor of the fiber-coupled organic scintillator. It depends on the number of scintillation photons measured during calibration, as well as on the stem-to-scintillation ratio, A/B, measured in the two spectral channels. The ratio $-b/a$ is defined as the Cerenkov light ratio or stem signal ratio[6]. This means that the calibration coefficients a and b depend on the stem signal ratio. As stated in the paper, "The condition of validity of the spectral method is that the calibration factors must remain constant for all situations encountered during measurements". For the calibration procedure to be correct, the stem signal ratio must therefore be constant for the calibration configurations used. According to Guillot et al., this can be achieved in three ways. One is to choose an optical fiber for which attenuation is sufficiently low; another is to choose an optical fiber that exhibits wavelength-independent attenuation properties. Either of these two options ensure that the attenuation of light in the two wavelength domains is virtually the same. In this way, the b/a-ratio is not affected by differences in attenuation lengths between photons generated in the scintillator and ones generated at different lengths along the fiber. The third option is to optimize the transmission spectra of the optical filters used to separate the two spectral channels. The paper evaluates four different calibration

---

[6] The authors implicitly assume that the stem signal is composed of Cerenkov radiation only.

procedures, which have been summarized in table 2.1. The accuracy of all four procedures were evaluated in measurement configurations dominated by the stem signal. Procedures C and D were found to produce the best results. The calibration procedure D is similar to the procedure we have applied during experiments presented in this thesis.

2.4 Summary

- When exposed to ionizing radiation, an organic scintillator emits light in the UV wavelength area as a means of de-excitation of aromatic molecules. Fluorescent wave shifting molecules shift the emitted light towards longer wavelengths subject to less overlap with the scintillator absorption band.

- It has been stated in the literature that organic scintillators are highly water equivalent. Additionally, they are considered energy independent in the MV/MeV energy range, exhibit negligible temperature dependence (0.1 %/C° or lower) in the 0-50 C° range, and can be exposed to total doses of several kGy before showing significant signs of permanent or non-permanent radiation damage.

- Light from the scintillator is transmitted to a detector through a multi-mode optical fiber by the process of total internal reflection. Radiation-induced light from the optical fiber, the so-called stem signal, also contributes to the total light signal.

- The total light signal is converted into an electrical current by a PMT, CCD camera or other suitable photodetector.

- The stem signal comprises fluorescence and Cerenkov radiation generated in the optical fiber. There is no consensus in the literature regarding whether fluorescence or Cerenkov dominates the stem signal.

- The nature and intensity of the stem effect apparently depends on the optical fiber constituents and irradiation conditions - such as the energy of the ionizing radiation and the angle between the fiber axis and the radiation beam.

- Several methods for stem effect removal can be considered. So-called chromatic removal has been chosen for the experimental setup presented in this thesis. Chromatic removal involves light detection in two wavelength intervals followed by a calibration procedure involving two or more measurements, yielding the measured dose to the scintillator.

Chapter 3

Materials and methods

The recently developed dosimetry system, consisting of fiber-coupled organic scintillators and in-house developed data acquisition hardware, is introduced in this chapter. The fiber-coupled organic scintillators are positioned in the linac radiation beam and emit visible light as a response to the radiation. The radiation-induced light signals are transmitted through the optical fibers to the in-house developed detection system, which consists of optical elements for chromatic signal separation, photodetectors for light detection, and electronics for data acquisition and analysis.

3.1 Making of the dosimeter probes

The organic scintillator employed in this project was in most cases the polystyrene-based Bicron® BCF-60. This kind of organic scintillator is commercially available from Saint-Gobain Ceramics & Plastics Inc., France. The BCF-60 is basically a doped optical fiber, consisting of a polystyrene base matrix doped with a fluorescent dye that shifts the primary scintillation light from UV to visible green. Because scintillation light is emitted isotropically, only a small portion of the scintillator light is normally directed through the scintillator towards the optical fiber, while the remaining light is lost to the surroundings. To minimize this effect, the BCF-60 is surrounded by an acrylic cladding to guide the scintillation light by total internal reflection - similar to an optical fiber. The BCF-60 comes in 2 m long fibers that can easily be cut to the desired length. The diameter of the scintillator is 1 mm in total.

The BCF-60 has been coupled to optical fibers and used for radiotherapy dosimetry in studies published by research groups in France (Fontbonne et al., 2002; Frelin et al., 2005) and Canada (Archambault et al., 2005, 2006a). Although the light output of the BCF-60 is low compared with blue-emitting

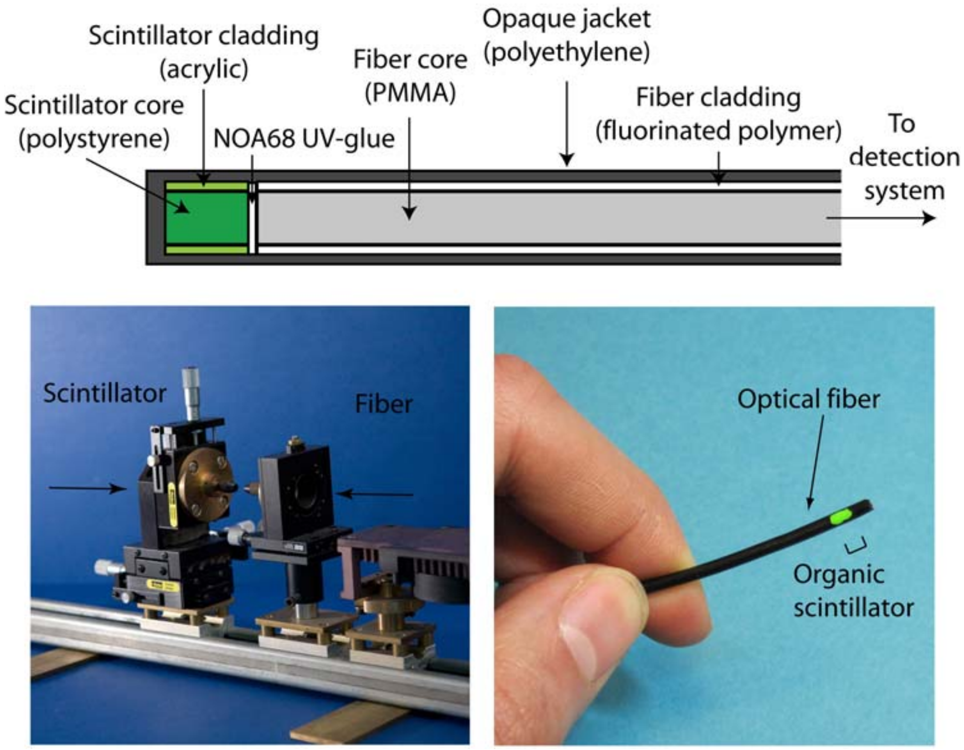

Figure 3.1: Making of a fiber-coupled organic scintillator. The scintillator and fiber are polished and thereafter coupled using a mechanical fixation mount and UV-curing glue. A coating of black epoxy cement is later applied to protect and light-tighten the bond. The position of the scintillator is indicated with green paint. The scintillator position is obtained from the shadow it casts on a piece of radiochromic film after exposure to 50 kV x-rays.

scintillators, such as the BCF-12[1], it was chosen for this project based on its potential for more accurate chromatic stem signal removal. Although Archambault et al. (2006a) used the blue-emitting BCF-12 for chromatic removal, previous studies by our research group show that the use of blue-emitting scintillators is problematic due to a potential large overlap between the stem signal and scintillator emission spectra (Beierholm, 2007). In addition, the attenuation of light due to Rayleigh scattering in an optical fiber is wavelength dependent. Specifically, UV and blue light is attenuated more severely than light of longer wavelengths. Because the chromatic removal procedure is based on the collection of light in two wavelength domains, differential light transmission in the fiber becomes an issue if the light is

---

[1] According to the data sheet by Saint-Gobain (2005), the scintillation output of the BCF-60 is approximately 7100 photons/MeV compared with 8000 photons/MeV for the BCF-12.

generated in different parts of the fiber. As will be shown in section 4.3.4, this poses a greater problem for a UV/blue-based chromatic separation than for a blue/green-based one.

Seven different kinds of commercial optical fibers were investigated for potential dosimeter use together with the BCF-60 scintillators. Two fibers were based on silica; namely, the BFH48-600 and BFL48-600, both sold by Thorlabs Sweden AB. The remaining five fibers were polymer-based: The ESKA^{TM} Premier GH2001-P and GH4001-P (Mitsubishi-Rayon Co., Japan); the PJS-CD1001-22E (Toray Industries Inc., Japan); the BCF-98 (Saint-Gobain Ceramics & Plastics Inc., France), and finally, the graded-index GIPOF120-P (Chromis Fiberoptics Inc., USA; sold by Thorlabs Sweden AB). Based on basic intercomparison experiments to be presented in section 4.1, the ESKA^{TM} Premier GH4001-P was chosen as the best fiber for the applications presented in this thesis.

Scintillators and fibers were coupled in the following manner: First, the BCF-60 scintillating fibers were cut to desired length (1-10 mm in this project). The exposed ends of the scintillator and the optical fiber were polished prior to coupling. Aluminium oxide polishing paper of 5, 3, 1 and 0.3 μm grain size (Thorlabs Sweden AB) was used, and the junctions were subsequently cleaned using water and pressurized air. The two components were aligned using a mechanical fixation mount and a stereo microscope, before making the coupling permanent using UV-curing, refractive index-matching glue (NOA68, Norland Products Inc., USA). To light-tighten and protect the bond, a jacket was made from black epoxy cement (EPO-TEK$^{®}$ 320, Epoxy Technology Inc., USA) around the exposed part of the probe. The cemented probe end was subsequently painted with black paint to completely prevent entry of exterior light. It is critical to know the exact position of the scintillator in the probe, especially when measuring in small radiation fields. To determine the location of the scintillator, the probe end was placed on a piece of radiochromic film (Gafchromic^{TM} EBT) and exposed to 50 kV x-rays from a small x-ray device. After a few minutes of exposure at 0.8 mA of applied current, the shadow of the probe was evident on the film. The position of the scintillator was indicated on the probe using green paint, as seen in figure 3.1. The other end of the fiber was terminated by a permanent SubMiniature version A (SMA) connector to allow easy connection to the light detection hardware.

3.2 Detection hardware

To collect the light signal from a fiber-coupled organic scintillator and convert it to an electrical current and subsequently a measurement of absorbed dose, the detection hardware must contain optics for wavelength discrimination and a suitable photodetector, along with suitable data acquisition

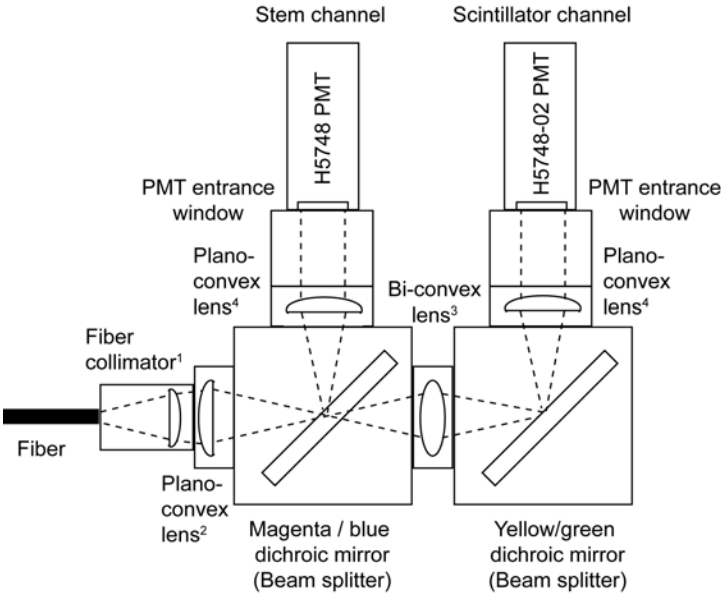

Figure 3.2: Schematic showing the optical setup of the light detection hardware. The optical elements used for focusing (Thorlabs AB, Sweden) are the following: ^{1}f230SMA-A aspheric lens fiber collimator (f = 4.34 mm); ^{2}LA1560-A plano-convex spherical lens (f = 25.4 mm); ^{3}LB1761-A bi-convex spherical lens (f = 25.4 mm); ^{4}LA1951-A plano-convex spherical lens (f = 25.4 mm).

electronics. The light signal from the scintillator is dominated by visible green light, while the stem signal from the fiber is dominated by visible blue and soft UV light. Two 45° dichroic mirrors (Edmund Optics Ltd., United Kingdom) were used to split the total collected light signal into a blue component and a green component. The expected transmission and reflection properties of the mirrors used are listed in table 3.1. The total light signal transmitted through the optical fiber enters the detection hardware by a fiber collimator. The GH4001-P fiber has a large numerical aperture (NA = 0.5), so the light beam was focused on the dichroic beams and PMT front

Table 3.1: Transmission and reflection properties of the dichroic filters used for the detection hardware, as stated by the manufacturer.

Dichroic mirror	Stock No.	Transmission (%)	Transmission λ (nm)	Cut-off λ (nm)	Reflection λ (nm)
Blue	NT47-267	90	530-800	510	400-475
Green	NT47-268	90	600-800	NA	520-550
Magenta	NT66-247	90	520-580	495 & 605	400-465 & 635-725
Yellow	NT66-246	90	400-495	520	550-725

windows using various lenses (see figure 3.2). The light collection setup was built in a frame of lens tubes and cube modules from Thorlabs Sweden AB. Because this setup involves high F-number optics, the transmission and reflection spectra of the two dichroic mirrors might not be as expected. However, this solution was a compromise between maximized optical throughput and well-defined spectral separation between the two channels.

The Hamamatsu H5784 and H5784-02 PMT modules were chosen as suitable photodetectors for a fast-acquisition detector system. Since the instantaneous dose rate within the radiation pulses from the linac is very high, the chosen photodetector must be able to handle these concentrated radiation bursts. Until the beginning of this PhD project, the Perkin Elmer MP982 and MP983 were the chosen PMT modules for a fiber-coupled optical dosimetry system (Aznar, 2005; Beierholm et al., 2008). The Perkin Elmer modules operate in photon-counting mode, measuring low light intensity signals with 15 ns temporal resolution. However, the very high event rate caused by a pulsed linac beam saturates the Perkin-Elmer PMTs if the instantaneous count rate becomes comparable to or exceeds approximately 4 MHz (Beierholm, 2007). For the medical linacs used in this project, a pulse width on the order of 5 μs and a pulse period on the order of 3 ms is typical at maximum delivered dose rate. This means that a detected light signal of 1 count per second (cps) corresponds to an actual event rate of 600 Hz. Furthermore, this indicates that a count rate of roughly 6600 cps or higher will yield a nonlinear, saturated PMT response (If the decay time of the organic scintillator was significantly longer, this would not be a problem as the event rate would drop). Because such light levels are not uncommon in these applications, the Perkin-Elmer PMTs were considered unsuitable for a fiber-coupled organic scintillator dosimetry system.

The H5784 and H5784-02 PMT modules are operated in current mode, meaning that the signal incident photons results in an averaged electron current which is then measured as a voltage signal. The sensitivity of the PMTs can be set by varying the gain voltage (0.0-0.9 V). Hereby, the high event rates encountered in pulsed linac beams do not affect the PMT response as dramatically as for the Perkin-Elmer modules. Another advantage of the Hamamatsu PMTs is their small size, making them convenient for fitting inside a hardware casing together with optical elements and data acquisition electronics.

The finished ME04 hardware, including PMTs, optics and electronics, is shown in figures 3.3 and 3.3.

3.2.1 PMT voltage readout 1: Capacitor discharge sampling

The first version of the ME04 detector system employed a simple resistor-capacitor circuit for signal transduction. The light signal from fiber and scintillator induced a current in the PMTs, leading to charge build-up and

Figure 3.3: ME04 hardware during data acquisition at Rigshospitalet. On the top shelf stands a laptop PC, used for controlling data acquisition and analysis, and a TTi TGA12101 waveform generator used for processing the target current signal from the linac. The ME04 system is seen on the bottom shelf, along with two NI USB-6218 DAQ cards used for data acquisition.

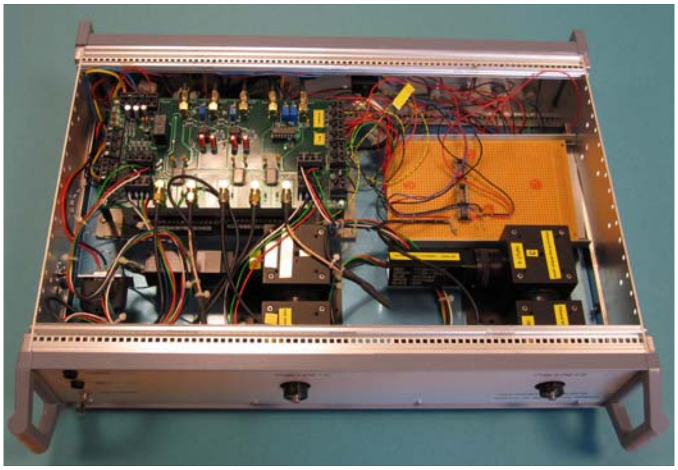

Figure 3.4: ME04 hardware with the top cover removed. The light collection optics and PMTs are placed in the front part, while the data acquisition electronic circuits are seen in the back.

subsequent discharge of a capacitor through a resistor. The characteristic time constant τ of capacitor discharge was controlled by the capacitance C and the resistance R, since $\tau = RC$. For fast data acquisition, a capacitor of 10 nC capacitance and a resistor of 10 kΩ resistance were connected in series, yielding a time constant of 100 μs. The capacitor discharge sampling was triggered by the linac synchronization pulse, using 20 samples per pulse at 50 kHz sampling rate (see figure 3.5).

3.2.2 PMT voltage readout 2: Switched integrator sampling

As an improvement over the original data sampling method, a setup comprising Burr-Brown ACF2101 dual switched integrating amplifiers was built. This kind of voltage readout is different from the original setup in several ways. The resistor-capacitor circuit was maintained; the main difference from the initial voltage readout setup is that the charge built up in the capacitor can be held while sampled. This ”sample-hold” setup applies an analog switch; opening of the switch causes the output from the resistor-capacitor circuit to be maintained. An amplifier is included in the circuit to prevent attenuation of the voltage signal. Detailed descriptions of switched integrator circuits are found in Dawson (2008) and Mountford et al. (2008). During irradiation, each synchronization pulse from the linac yielded charge building up in the capacitor. Using the switched integrator circuit, the capacitor output was held, integrated, and read out before it was reset at the onset of the next synchronization pulse. The main advantage of this setup was that the PMT voltage signals did not need to be sampled simultaneously, since the integrated signal was held fixed until the switch was opened again. The temporal characteristics of voltage readout was controlled through several parameters: the sample rate and the number of samples per pulse, as well as the onset and duration of the sample-hold parameters reset, hold and scan.

Three ACF2101 dual switched integrators were used in the improved ME04 design. Two were used for sampling of the voltage readings from the four PMTs while the third was used for measuring the time integral of the linac target current. The temperature inside the hardware casing was measured using a thermistor. For each synchronization pulse, the held voltage signal was sampled once. Figure 3.6 shows the basic principles of synchronized sampling using the switched integration amplifiers. Before adjusting the sample-hold timing parameters, the time structure of the linac was determined using an oscilloscope as well as the ME04 system in non-synchronized (continuous) sampling mode. Based on this, the following parameters were chosen: The switch was closed after 6 μs and opened again after 86 μs, yielding a signal integration window of 80 μs. While held, the integrated signal was sampled after 100 μs. The sample-hold circuit was reset 0.5 μs after each linac synchronization pulse.

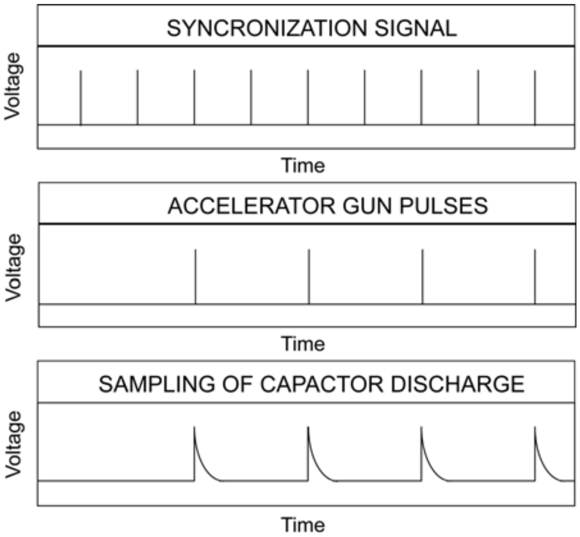

Figure 3.5: Synchronized signal voltage readout with sampling of capacitor discharge. The linac gun pulse frequency is shown for a repetition rate which is half of the maximum rate.

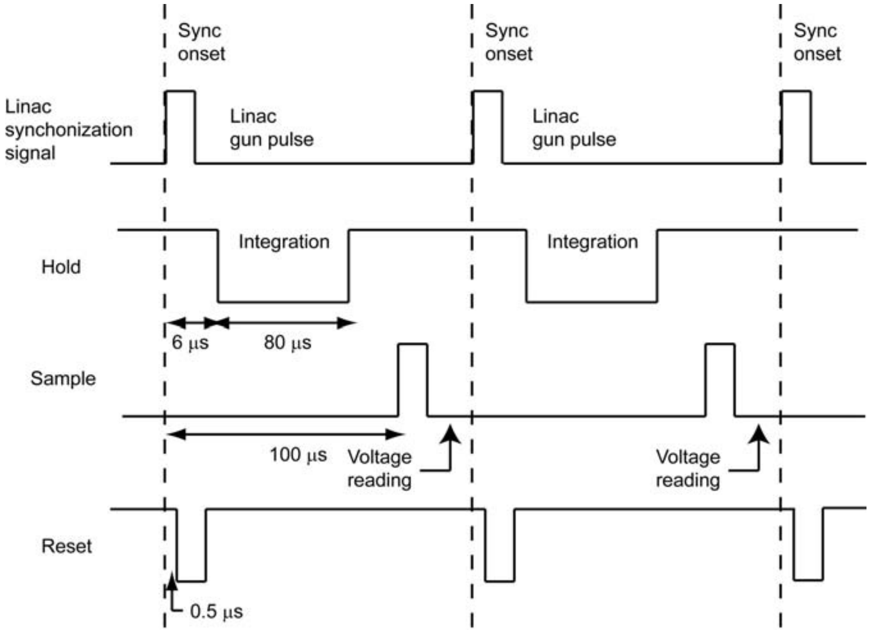

Figure 3.6: Synchronized signal voltage readout with switched integrator sampling. The intrinsic timing is reset at the onset of the linac synchronization pulse; the switch is closed after the termination of the synchronization pulse, allowing integration of the charge built up in the capacitor. The switch is opened again to hold the voltage reading, which can then be sampled.

3.3 Measurement setup at a hospital

All clinical measurements presented in this thesis were performed using MV x-ray beams delivered by a medical linac at a hospital. The fiber-coupled organic scintillator probes were irradiated in a solid water phantom (CTG-457, Gammex Ltd, UK). As shown in figure 3.7, grooves of 2.5 mm x 2.5 mm x 300 mm dimensions were drilled along the center of some of the solid water slabs for a tight housing of the dosimeter probes. The slab containing one or two dosimeter probes was then inserted in the stack at the desired measurement depth, as shown in figure 3.8 (left). Measurements of percentage depth dose were made by moving the dosimeter slab down the stack for each measurement depth.

A flow chart of the measurement setup is presented in figure 3.9. The radiation-induced light signals were transmitted through the 10 m long optical fibers to the ME04 hardware, which was positioned in the maze on the other size of the concrete wall shielding the treatment room. This was done to prevent electrical interference caused by stray radiation in the treatment room. The voltage signals from the switched integrator circuits were acquired using an NI USB-6218 DAQ cards (National Instruments Inc., USA) connected to a laptop computer using a USB cable. The timing of the synchronized data acquisition was similarly controlled by a timing module consisting of two NI USB-6218 cards. Two laptop computers were used to carry out the data acquisition. The laptop connected to the ME04 (the "DAQ" computer) was placed inside the maze corridor, alongside the ME04 system on a small roller table as seen in figure 3.8 (right). The DAQ computer was remote controlled by the "remote" computer using an ethernet connection; this was done so that data acquisition could be controlled from inside the linac control room on the other side of the maze, using the remote laptop. Data acquisition and data analysis was performed using the so-called MEView software, which has been in-house developed in LabVIEW$^{\mathrm{TM}}$.

To enable synchronized data sampling, the ME04 must be connected to the linac synchronization signal output using a BNC cable. For measurements performed using a Varian linac, the ME04 was connected to the "SYNC" output of the linac. To be able to i) count the linac target current pulses and ii) measure the target current per pulse, the ME04 was also connected to the "ITARGET" output of the linac via BNC cables. For measuring the time integral of the target current for each synchronization pulse, the ME04 was connected to the ITARGET output directly. For logging and counting the gun pulses, manipulation of the ITARGET signal was necessary via an intermediate connection to a TTi TGA12101 waveform generator (Thurlby Thandar Instruments Ltd., UK).

For measurements performed using an Elekta linac, synchronized data sampling was enabled by connecting the ME04 to the "ST" BNC output of the linac. The waveform generator was in this case necessary for transforming

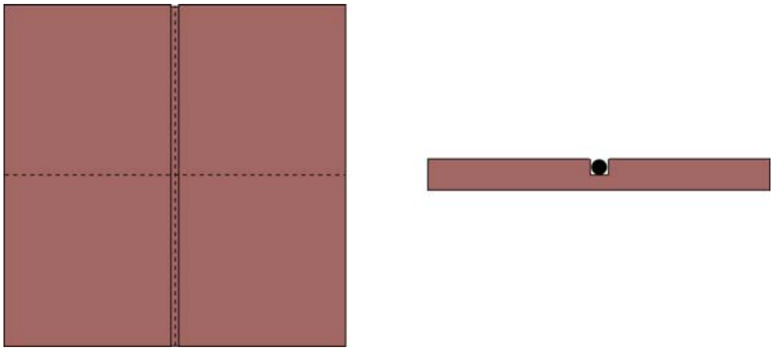

Figure 3.7: Grooves were drilled in some of the solid water slabs to house the dosimeter probes.

Figure 3.8: Example of measurement setup at Rigshospitalet. Left: Fiber-coupled organic scintillators are irradiated in solid water using 6 MV x-rays from a Varian 2300 iX medical linac. Right: The light signals are transmitted to the detection system on the other side of a concrete maze. On the table (top to bottom shelf) is a laptop for data acquisition, a frequency generator for handling the target current signal from the linac, an ME04 detector system for organic scintillator probes, and two ME03 systems for Al_2O_3:C probes.

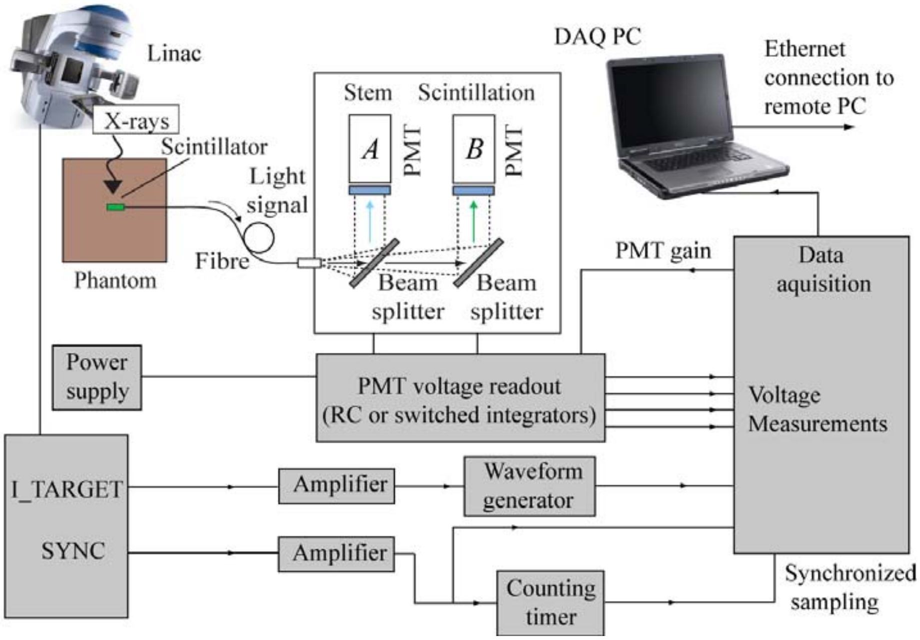

Figure 3.9: Flow chart of light detection and linac-synchronized data acquisition. For each linac SYNC pulse, the light from fibers and scintillators is chromatically discriminated and converted into voltage readings using either simple RC circuits or Burr-Brown switched integrator circuits.

the irregular ST signal into a usable square signal. Measurements of target current were not performed for the Elekta linacs.

3.4 Dosimeter calibration

Following the chromatic stem removal procedure, at least two measurements are needed to calibrate a fiber-coupled organic scintillator probe: One measurement for an irradiation configuration minimizing the contribution from the stem signal, and another measurement for a configuration which maximizes the stem signal contribution. From these measurements, two equations in two unknowns are obtained, yielding the calibration coefficients needed to convert the light signal readings into absorbed dose (recall equations 2.11 and 2.12).

The basic calibration configurations used in this project are shown in figure 3.10. The first measurement involves an irradiation at known delivered dose D_1 with the scintillator in the beam isocenter, sought to minimize the stem signal contribution relative to the scintillator signal. The second measurement involves an irradiation at out-of-field dose D_2 with the fiber going straight through the field and the scintillator positioned out of field. Hereby,

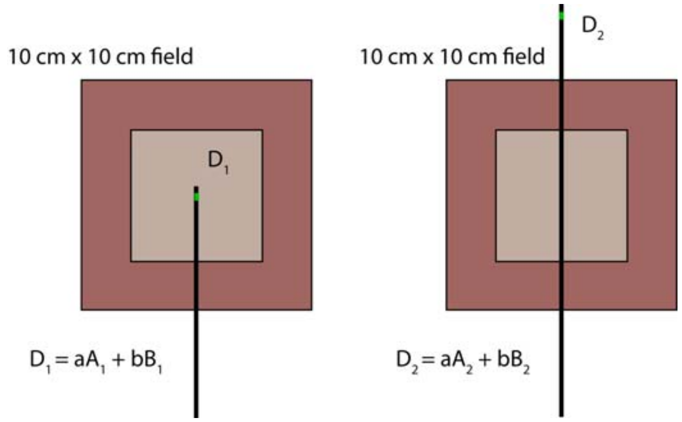

Figure 3.10: The two measurement configurations used for calibrating the fiber-coupled organic scintillators. Left: Irradiation at known delivered dose D_1 with the scintillator in the beam isocenter. Right: Irradiation at out-of-field dose D_2 with the fiber going straight through the field and the scintillator positioned out of field. The number of delivered MUs is the same for the two configurations.

the contribution from the stem signal is maximal since only the fiber is in the primary radiation field. Based on the conclusions of Beierholm et al. (2008), this second calibration configuration was chosen instead of the one suggested by Frelin et al. (2005) for two reasons: First, the out-of-field configuration is evidently a closer approximation to a maximum stem-to-scintillation ratio than an irradiation with approximately 1.5 m of wound fiber in a large radiation field. Secondly, the out-of-field configuration is expected to be less affected by the effects of attenuation length differences, and should thereby be less subject to systematic errors due to changes in the stem-to-scintillation ratio. In the out-of-field calibration configuration, the dose to the scintillator outside the field must preferentially be measured independently using an ionization chamber, TLD, or other dosimetry method; the other option is to shield the scintillator sufficiently to assume that the absorbed dose is negligible.

3.4.1 Calibration depth and field size

An important point regards the depth at which the calibration is performed. One can argue that d_{max} is normally considered the reference depth, since linacs are typically calibrated to deliver 1 cGy per MU for a 10 cm x 10 cm field at d_{max}. However, the exact value of d_{max} is not well defined, and will introduce a small systematic error if a dosimeter probe to be calibrated at 1.5 cm depth is actually calibrated at 1.4 cm depth. Following the arguments of Dutreix et al. (1997) and IAEA (2000), dosimeter calibration should be performed at 10 cm depth to avoid the electron contamination that is evident at and near d_{max}. Another important point is the field size(s) used for calibration. Since most linacs are calibrated at 10 cm x 10 cm field size, it seems natural to use this as the reference field size at which calibration is performed. More than one field size can be used for the two calibration configurations, to give a better measure of the uncertainty associated with the estimation of the two calibration coefficients. However, the inclusion of other fields than the reference 10 cm x 10 cm field makes calibration increasingly dependent on other dosimetry techniques used to independently measure the dose delivered at these fields.

3.4.2 Calibration settings used during this project

Table 3.2 gives the calibration configurations used for the major experiments presented in this thesis. All calibration configurations involved probe orientations with scintillators in as well as out of the field. The beam energy was 6 MV and the SSD 100 cm in most cases. For measurements of output factors and percentage depth dose (OF and PDD series, section 4.3.4), calibration was performed at 10 cm x 10 cm field size, while the pulse-resolved measurements in section 5.1.1 involved calibration at several field sizes of 3 cm x 3 cm up to 20 cm x 20 cm. The RapidArc® measurements of section 5.1.2 were made using 18 MV and not 6 MV beam energy. Here, the scintillator probes were calibrated at 5 cm depth, at 10 cm x 10 cm field size. Section 6.1 regards the only measurement series made at 95 cm and not 100 cm SSD, for 10 cm x 10 cm field size at 5 cm depth.

For all experiments mentioned so far, the dose to the scintillators in the out-of-field configuration was assumed to be negligible. The only exceptions to this were the experiments described in section 5.2 and 6.2, as well as in figure 4.14 of section 4.3.4. Here, probes were calibrated at 10 cm depth and 10 cm x 10 cm field size. The dose to scintillators out of field was measured using LiF TLDs. After the measurements, the dose absorbed in the TLDs was read out using a Dosacus TLD-reader (Alnor Oy, Finland) at the Radiation Research Division of Risø DTU.

3.5 Summary

The components used for the different developments of the dosimetry system are summarized in table 3.3. The preliminary dosimetry system is the one presented in Beierholm (2007) and Beierholm et al. (2008); as such, the table briefly summarizes the development of the system during the last three years.

Table 3.2: Dosimeter sensitive size, beam energy, SSD, field size (FS), depth (d) and given dose used for obtaining the calibration coefficients a and b/a for the various experiments in this project.

Experiment	Scint. length (mm)	Beam energy (MV)	SSD (cm)	FS (cm x cm)	d (cm)	Given dose (Gy)	a $\times 10^{-4}$	b/a
OF (Sec. 4.3.4)	3	6	100	10	1.5	0.999	-1.189	-4.289
				10	1.5	0.000		
PDD (Sec. 4.3.4)	3	6	100	10	1.5	0.999	-1.189	-4.289
				10	1.5	0.000		
DPP (RC) (Sec. 5.1.1)	3	6	100	3-20	1.5	0.907-1.051	-1.193	-4.253
				3-20	1.5	0.000		
	4	6	100	3-20	1.5	0.907-1.051	-3.550	-6.037
				3-20	1.5	0.000		
RapidArc (Sec. 5.1.2)	3	18	100	10	5	0.961	-2.005	-4.111
				10	5	0.000		
	4	18	100	10	5	0.961	-5.891	-6.092
				10	5	0.000		
DPP (Int) (Sec. 5.2)	4	6	100	10	10	0.157	-1.485	-3.612
				10	10	0.001		
	2	6	100	10	10	0.157	-8.727	-2.603
				10	10	0.001		
IAEA-OF (Sec. 6.1)	1	6	95	10	5	0.237	-2.169	-3.937
				10	5	0.000		
Small-OF (Sec. 6.2.1)	1	6	100	10	10	0.157	-1.976	-4.216
				10	10	0.001		
Small-PDD (Sec. 6.2.2)	1	6	100	10	10	0.157	-1.976	-4.216
				10	10	0.001		
Volume Averaging (Sec. 6.2.3)	1	6	100	10	1.5	0.249	-2.033	-4.184
				10	1.5	0.001		
	2	6	100	10	1.5	0.249	-1.113	-3.900
				10	1.5	0.001		
	3	6	100	10	1.5	0.249	-2.769	-3.674
				10	1.5	0.001		
	4	6	100	10	1.5	0.249	-1.452	-3.498
				10	1.5	0.001		
	5	6	100	10	1.5	0.249	-3.722	-4.810
				10	1.5	0.001		
	10	6	100	10	1.5	0.249	-0.282	-4.042
				10	1.5	0.001		

Table 3.3: Components used for the scintillator-based dosimetry system.

	Preliminary dosimetry system	ME04 system version 1	ME04 system version 2
Organic scintillator	Saint-Gobain BCF-12	Saint-Gobain BCF-60	Saint-Gobain BCF-60
Fiber	ESKA^{TM} GH4001-P	ESKA^{TM} GH4001-P	ESKA^{TM} GH4001-P
45 deg dichroic filters	Delta BSP 390/500	Edmund dichroic blue/green	Edmund dichroic yellow/magenta
PMTs	Perkin-Elmer MP983	Hamamatsu H5784/H5784-02	Hamamatsu H5784/H5784-02
Data Acquisition	Uniform sampling	Synchronized sampling (RC capacitor discharge)	Synchronized sampling (switched integrator)
Pulse resolution	No	Yes	Yes

Chapter 4

Basic experiments and dosimetry

This chapter presents experiments that have motivated the development of the final dosimetry system and measurement setup. To maximize the accuracy and precision of dose measurements using fiber-coupled organic scintillators, several parameters can be varied and optimized. The choice of optical fiber must be justified by favorable transmission properties, minimal beam perturbation and well-defined stem signal characteristics. Secondly, the method used to correct for the stem signal generated in the fiber must be effective to minimize systematic measurement uncertainties. All experiments discussed in this chapter have been performed to evaluate and optimize the performance of the new dosimetry system.

4.1 Optical fiber characteristics

Several brands of optical fiber were evaluated during the course of this project. The relevant properties of all fibers are listed in table 4.1. Entries marked with an (a) are provided by the manufacturers. Cerenkov threshold, relative Cerenkov intensity and fiber acceptance angle have been calculated from the core and cladding refractive indices using equations 2.7, 2.8 and 2.9.

4.1.1 Spectroscopic measurements

According to Marckmann et al. (2006), one of the causes of the stem effect is fluorescence due to water in the fiber. Following this argument, a low-OH fiber would theoretically exhibit a negligible contribution from fiber fluorescence to the overall stem signal. However, the studies by Arnfield et al. (1996) and Nowotny (2007) showed that the stem signal of low-OH fibers is significantly larger than for other fibers. In the study by Arnfield, the

Table 4.1: Relevant characteristics of the different kinds of commercial optical fibers investigated in this project. Rows marked with (a) are manufacturer data. The transmission loss of the fibers are estimated values obtained from the curves presented in appendix A.

	GH2001-P	GH4001-P	PJS-CD1001-22E	BCF-98	GIPOF120-P	BFH48-600	BFL48-600
Manufacturer	Mitsubishi-Rayon	Mitsubishi-Rayon	Toray Industries	Saint-Gobain	Chromis Fiberoptics	Thorlabs	Thorlabs
Core material^a	PMMA	PMMA	PMMA	Polystyrene	CYTOP	SiO_2	SiO_2
Index profile^a	Step index	Step index	Step index	Step index	Graded index	Step index	Step index
n^a_{core}	1.49	1.49	1.49	1.60	1.36(max)	1.46	1.46
Numerical aperture^a	0.5	0.5	0.63	0.58	0.185	0.48	0.48
Core diameter (μm)^a	486	980	980	970	120	600	600
Cladding diameter (μm)^a	500	1000	1000	1000	490	1040	1040
Transmission loss (dB/m)^a	0.09 @ 500 nm	0.09 @ 500 nm	0.11 @ 500 nm	0.30 @ 500 nm	0.06 @ 600 nm	0.02 @ 500 nm	0.02 @ 500 nm
Bending radius (mm)^a	15	25	NA	NA	10	94.5	94.5
Cerenkov threshold (ke$V$)	177.5	177.5	177.5	143.6	245.6	188.0	188.0
Cerenkov norm. intensity	1.00	1.00	1.25	1.43	0.25	1.50	1.50
Acceptance angle (deg)	18.8	18.8	23.4	21.4	7.0	29.5	29.5

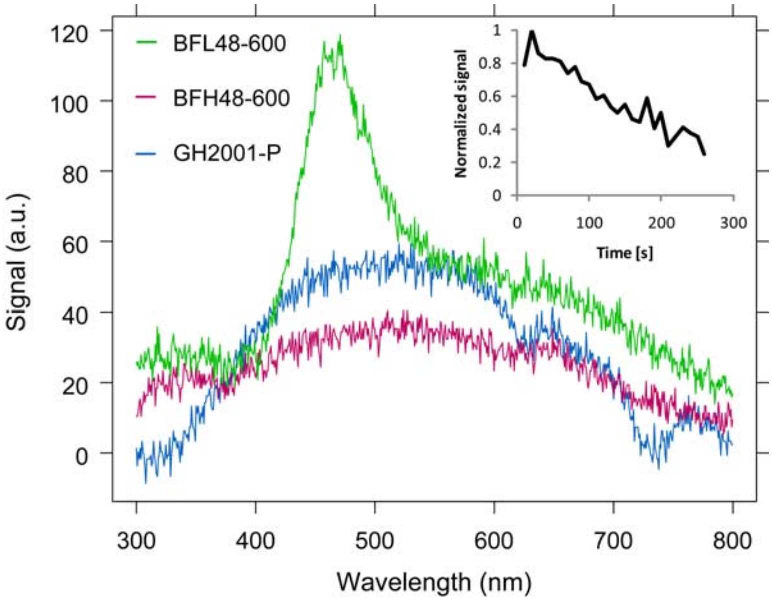

Figure 4.1: Raw stem signal spectra for BFL48-600 (Low-OH silica), BFH48-600 (High-OH silica) and GH2001-P (PMMA) for 300-800 nm wavelength. The length of the fibers were approximately 5 m. Insert: Behavior of the 450 nm luminescence peak of the BFL48-600 with exposure time, obtained using the QE65000 spectrometer in time-resolved mode.

low-OH fiber under study exhibited a strong luminescence peak at approximately 450 nm. To investigate the matter of low-OH fibers ourselves, we performed a simple experiment using an Ocean Optics QE65000 spectrometer to record the stem signal spectrum of a 5 m long low-OH BFL48-600 silica fiber and compare it to that of high-OH fibers. The fibers were exposed to γ radiation from a high-dose rate ^{60}Co gamma cell. The dose rate to the fibers was approximately 150 mGy/s. The raw data can be seen in figure 4.1. Stem signal spectra are plotted in the 300 nm to 800 nm wavelength range for fibers BFL48-600, BFH48-600 and GH2001-P. A distinct luminescence peak at approximately 450 nm is seen for the low-OH fiber. This apparent luminescence band showed evidence of radiation-induced degradation after a couple of minutes of γ exposure (figure 4.1, insert). The spectra have been corrected for the wavelength-dependent sensitivity of the spectrometer, but not for the transmission loss through the fiber. Nevertheless, this simple experiment supports that low-OH fibers are unsuitable for fiber-coupled optical dosimetry, as stated by Arnfield et al. (1996) and Nowotny (2007).
To investigate the stem signal in more detail, an Oriel 77250 1/8 grating monochromator (1200 lines/mm ruled grating; 1 mm slit width) and a Perkin-Elmer MP982 PMT were used to detect the wavelength-dependent intensity of the stem signal generated when irradiating a 5 m long PMMA-

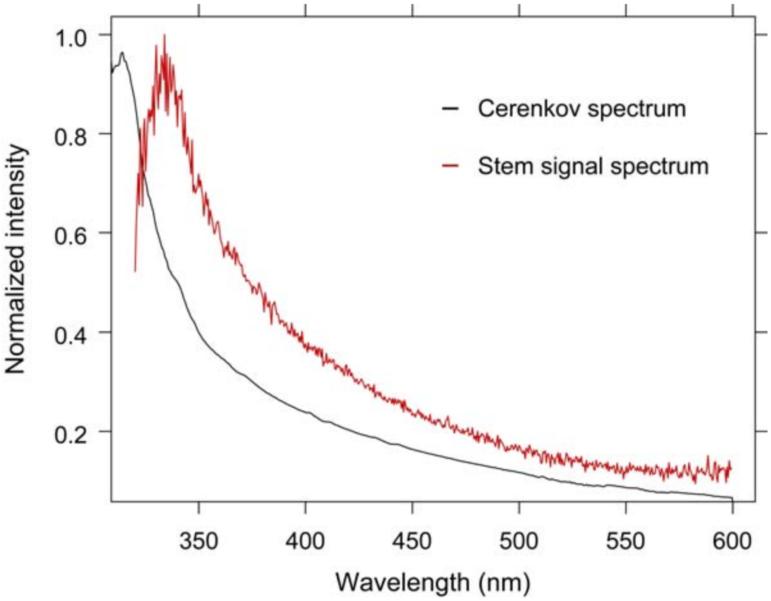

Figure 4.2: Stem signal spectrum for a PMMA-based GH2001-P optical fiber, obtained using the Oriel monochromator setup. Red curve: Measured fiber stem signal spectrum generated by β radiation from a radioactive source at 90° angle of incidence. Black curve: Theoretical Cerenkov intensity spectrum folded with the transmission spectrum of a 5 m GH2001-P long fiber.

based GH2001-P fiber using β-radiation from an 1.48 GBq ^{90}Sr/^{90}Y radioactive source ($E_{max} \simeq 2.2$ MeV). One end of the fiber was fixed onto a plastic tray, which was then inserted in a holder directly under the radioactive source, giving a 90° angle between the source and the fiber. The other end of the fiber was connected to the monochromator and PMT via an SMA connector and a Thorlabs f230SMA-A fiber collimator. The monochromator was wavelength calibrated using an Oriel 6025 Hg(Ar) lamp. The optical matching of the numerical aperture of the optical fiber to that of the monochromator was unfortunately very poor, resulting in a large signal loss. To generate a satisfactory spectral curve, a data acquisition speed of 0.1 nm/s was used. The result is shown in figure 4.2 for wavelengths between 300 nm and 600 nm. The spectral sensitivity of fiber, monochromator and PMT was taken into account by recording the transmission spectrum of a known blackbody source (HL-2000 Tungsten Halogen lamp, 2960 K color temperature, Ocean Optics Inc.). The stem signal spectrum was then divided by this sensitivity spectrum to obtain the true, sensitivity-corrected spectrum. The angle between the fiber and the primary radiation beam was 90°, so the contribution to the stem signal from Cerenkov radiation was expected to be smaller than the fluorescence contribution. Nevertheless, the expected water emission peak around 360 nm predicted by Marckmann et al. (2006) was not found. For comparison, a theoretical Cerenkov radiation spectrum is also plotted in figure 4.2. This spectrum is a folding between a simple λ^{-3} Cerenkov intensity spectrum and the transmission spectrum of the GH2001-P fiber, which was measured using the monochromator setup and the HL-2000 lamp. The Cerenkov spectrum exhibits an apparent maximum around 315 nm; this is believed to be caused by high transmission loss combined with the cut-off of PMMA occurring in this spectral region. By comparison, the measured fiber stem signal peaks at approximately 334 nm. The difference between the two spectra is believed to be the fiber fluorescence contribution. However, this experiment is not supported by the findings reported in studies like de Boer et al. (1993) and Marckmann et al. (2006). Similar spectral curves were recorded for the PMMA-based GH-4001 ($\lambda_{peak} \simeq 337$ nm) and the silica-based BFH48-600 ($\lambda_{peak} \simeq 323$ nm) fiber stem signals.

4.1.2 Fiber intercomparison

The magnitude of the stem signal generated in the different optical fibers was compared by subjecting the fibers to β radiation from the ^{90}Sr/^{90}Y radioactive source. Each fiber was polished using aluminium oxide polishing sheets (see section 3.1). One end of the fiber was placed under the radioactive source, at a specified distance such that the dose rate to a water equivalent material was approximately 5.8 mGy/s at the location of the fiber tip. The other end was connected to a Perkin-Elmer MP983 PMT. Several samples of each fiber were used, being either 5 m or 1 m in length.

Table 4.2 shows the relative stem signal magnitude for the respective fibers. The measured values have been divided by the volume of irradiated fiber, and are presented normalized to the ESKA^{TM} Premier GH4001-P stem

Table 4.2: Relative magnitude of the stem signal generated in the different optical fibers when exposed to beta radiation. The measured stem signals have been divided by the irradiated fiber volume and corrected for transmission loss, and are shown normalized relative to the GH4001-P stem signal. Uncertainties are given as 1 SD of the mean.

	GH4001	GH2001	CD1001	BCF-98	GIPOF120	BFH48
Number of fibers	4	4	3	3	4	3
Number of measurements	10	10	9	9	8	6
Core diameter [μm]	980	486	970	120	600	600
Normalized stem signal per mm^3	1.00 ± 0.04	1.03 ± 0.03	1.35 ± 0.05	0.64 ± 0.04	0.17 ± 0.01	0.82 ± 0.03

signal. All stem signal values expect one[1] were corrected for attenuation-induced signal loss using the attenuation values given in table 4.1. The low-OH BFL48-600 silica fiber was omitted from this intercomparison due to its unfavorably high and unpredictable stem signal, as evident from figure 4.1 and supported by the studies by Arnfield et al. (1996) and Nowotny (2007). The measured stem signals were found to be of comparable magnitude for the GH4001-P and GH2001-P PMMA-based fibers. The fiber exhibiting the lowest measured stem signal, amounting to 17 ± 1 % of the GH4001-P stem signal, was the graded-index GIPOF120-P perfluorinated polymer fiber. If this fiber was to be fabricated with a core of 0.5-1.0 mm diameter, it would be a promising choice for scintillation dosimetry applications. However, 120 μm is the largest fiber core diameter available among the graded-index polymer fibers. Given the fiber core cross-sectional area compared with a 1.0 mm diameter BCF-60 scintillator, this means that 98.5 % of the scintillator light will be lost at the scintillator-fiber interface, resulting in a low signal-to-noise level. Additionally, it is expected that the fluoride doping of the fiber makes it highly susceptible to radiation damage. The stem signal of the polystyrene-based BCF-98 was found to be 36 ± 4 % lower than for the GH4001-P. However, attenuation is significantly higher in the BCF-98, and this will be a potential problem for the chromatic removal calibration procedure[2]. The third PMMA-based fiber, the PJS-CD1001-22E exhibited a stem signal of 35 ± 5 % higher magnitude than for the GH4001-P. Because we are using the chromatic removal method, this is not a significant disadvantage.

Finally, the BFH48-600 high-OH silica fiber exhibited a stem signal that was 18 ± 3 % lower than for the GH4001-P. In addition, the silica fiber exhibits the lowest attenuation of all the tested fibers. Contrary to PMMA- and polystyrene-based fibers, silica fibers are however not water equivalent. For dose measurements in water or solid water, the silica fiber will therefore perturb the radiation fluence around the dosimeter probe more than a polymer fiber will. This might be a critical effect in non-equilibrium situations, such as in build-up regions or small fields. Therefore, we chose not to use the BFH48-600 for our fiber-coupled organic scintillators.

From this comparison between different kinds of optical fibers, the ESKA^{TM} Premier GH4001-P was found to be the best choice of fiber for this project. However, the use of other PMMA-based fibers could also be justified, along with the use of high-OH silica fibers for applications where the water equivalence of the dosimeter is not critical.

---

[1] The transmission loss of the GIPOF120-P at 500 nm was unfortunately not available. Therefore, the measured stem signal from this fiber was not corrected for attenuation-induced signal loss.

[2] This is further supported in the paper by Guillot et al. (2011) that was published near the conclusion of this project.

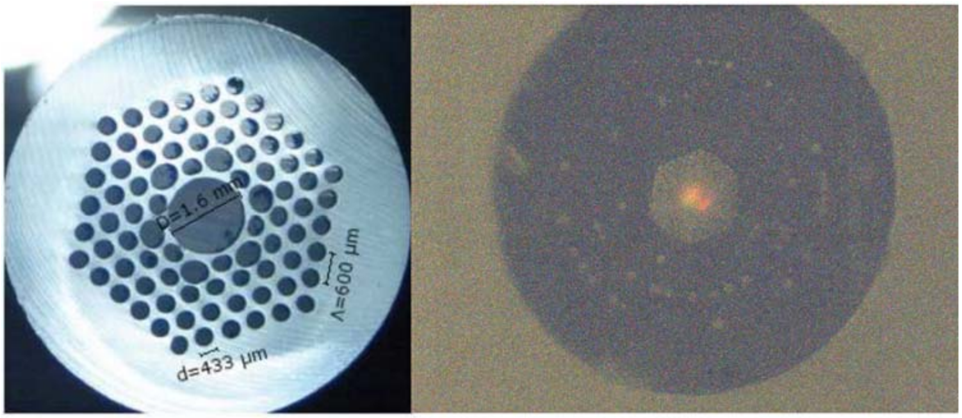

Figure 4.3: Cross-sectional view of a 350 μm hollow-core PCF, manufactured by Kristian Nielsen at DTU Photonics. Left: Preform of the microstructured fiber (picture obtained using scanning electron microscope). Right: The finished drawn fiber, guiding visible light. The microstructure is seen to occupy a relatively small area of the total fiber cross section (picture obtained at 20 x magnification).

Photonic crystal fibers

Micro-structured optical fibers, also called photonic crystal fibers (PCFs), were also briefly investigated for use in this project. In such fibers, the guidance of light in the fiber core is governed by a structure of holes instead of a core and cladding of different refractive indices. Furthermore, the approach for Cerenkov-free light guidance in a capillary tube led us to believe that the same Cerenkov-free light guidance might be achieved with hollow-core PCFs. However, the main challenge of hollow-core as well as solid-core PCFs is the small dimensions of such fibers.

To evaluate the feasibility of the method, we investigated a hollow-core PCF which was manufactured for us by Kristian Nielsen at DTU Photonics. Cross-sectional views of the fiber preform and the finished fiber are presented in figure 4.3. The length of the fiber was 25 cm, while the total outer diameter of the fiber was 350 μm. A simple experiment using the fiber coupled to a piece of BCF-12 organic scintillator and exposed to β radiation from the ^{90}Sr/^{90}Y radioactive source suggested that the diameter of the hollow core was too small for sufficient collection and transmission of light from the scintillator. A solid-core PCF of similar dimensions was also prepared for us. The solid-core version gave better results, but the signal-to-noise ratio of the measurements was still insufficient. Because the guidance properties of both solid-core and hollow-core PCFs are highly dependent on the dimensions of the fiber structure, it was not possible to achieve a fiber of satisfactory dimensions to ensure a sufficiently high throughput. The PCFs were therefore omitted from further study.

4.2 Organic scintillators with long luminescent lifetimes

As described in section 2.3.2, temporal removal of the stem signal can be achieved for radiotherapy dosimetry applications if the luminescent lifetime of the dosimeter material is significantly longer than that of the stem signal. However, this has proven difficult to accomplish for organic scintillators, which normally exhibit lifetimes of the same order of magnitude as the stem signal (ps-ns). As described by Lindvold et al. (2010), organic scintillators with individually customized emission spectra and luminescent lifetimes can be made in the laboratory by choosing a suitable scintillator base and suitable organic dyes. In this section, intercomparison measurements between an in-house developed organic scintillator and the commercial BCF-60 are presented.

The in-house developed scintillator was designated Scintillator 73. A Trimethylol propane benzoatediacrylate photo-curable monomer served as the scintillator base. The base was doped with a 2,5-Diphenyloxazole (PPO) primary scintillator (6.3 % wt) and a Perylene wavelength shifter at 1:250 Perylene-PPO concentration. Similar to the BCF-60 commercial plastic scintillator, the doped Scintillator 73 monomer was moulded onto a GH-4001P fiber of approximately 10 m length.

4.2.1 Luminescent lifetime measurements

The scintillation process in organic plastics is normally very fast, occurring through singlet transitions. In the long-lifetime Scintillator 73 investigated in this study, the de-excitation process occurs through a triplet process with much lower probability than for a singlet process.

Samples of Scintillator 73 and BCF-60 were excited by high energy x-rays from a Varian 2300 iX linac at Herlev Hospital. The fiber-coupled organic scintillators were exposed to 6 MV x-rays at 10 cm x 10 cm field size at 1.5 cm depth in solid water. The scintillator light was detected by a Perkin-Elmer MP983 PMT, operated in photon-counting mode and equipped with a 460-540 nm band pass filter. Lifetime measurements were made by gating the detected signal using a TTL 7408 gate controlled by the linac synchronization signal, and data acquisition was conducted using a NI 6218 DAQ card. A detection window 10 μs wide was applied using the TTL gate. By varying the delay between the linac synchronization pulse and the opening of the gate for each measurement, luminescence decay curves were achieved in 10 μs increments for Scintillator 73, BCF-60, and a blank ESKA$^{\text{TM}}$ GH-4001P fiber.

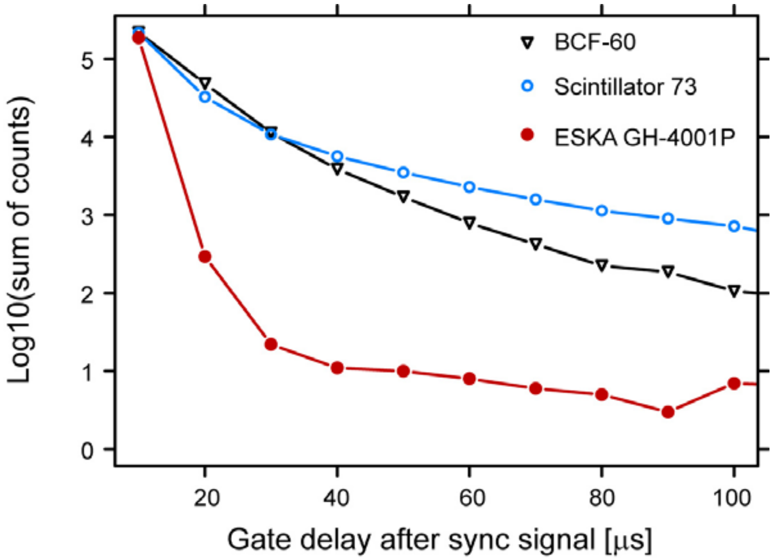

Figure 4.4: Linac irradiation lifetime measurements (semilogarithmic scale). Detected signal versus gate delay for Scintillator 73, BCF-60 and ESKA^{TM} GH-4001P optical fiber. The gating window was 10 μs long for all measurements.

Figure 4.4 shows the 1/e resulting lifetime measurements on a semilogarithmic scale. A 10.3 ± 2.6 μs lifetime was measured for BCF-60, while 20.2 ± 4.4 μs was the lifetime measured for Scintillator 73. The measured luminescent lifetimes for both the BCF-60 and Scintillator 73 agreed well with lifetimes obtained with a Edinburgh Instruments FLS920 spectrofluorimeter (see chapter 10). However, the noise floor evident in figure 4.4 and the lifetime measured for the bare optical fiber raises concern. It is unknown if the apparent 2-5 μs measured stem signal lifetime is an artifact caused by the measurement setup, or a real property of the optical fiber. However, the latter option is highly unexpected and not supported in the literature (Clift et al., 2002; Justus et al., 2004; Marckmann et al., 2006).

4.2.2 Basic dose measurements

An attempt at performing actual dose measurements with Scintillator 73 was made by choosing a gating window of 60 μs and a delay of 40 μs. Measurements of percentage depth dose and output factors were performed using an Elekta SL*i* linac at Herlev, delivering 8 MV x-rays. The PDD measurements showed agreement within 3 % compared with expected, tabulated values (BJR, 1996). However, the signal-to-noise ratio was impaired by the gating due to the insufficient lifetime of Scintillator 73. Furthermore, incomplete suppression of the stem signal was evident, yielding a 5 % dose error when the size of the field was varied between 5 cm x 5 cm and 25 cm

x 25 cm.
These experiments show that although the application of temporal stem signal removal for fiber-coupled organic scintillators seems theoretically achievable, the signal-to-noise ratio and accuracy of the dose measurements is insufficient if the scintillator luminescent lifetime is not significantly different from the stem signal lifetime as well as from the linac pulse duration. Therefore, we concluded that a dosimetry system based on chromatic stem effect removal was at this point the only realistic option for accurate radiotherapy dosimetry using fiber-coupled organic scintillators.

4.3 Dosimetry system characteristics

For a new dosimetry system to be effective in a clinical environment, several demands must be met. A highly reproducible response that is linearly proportional to the dose absorbed and independent of dose rate is a general demand; furthermore, dose measurements using fiber-coupled organic scintillators must be free from influence of the parasitic stem signal generated in commercial optical fibers. The experiments presented in sections 4.3.1, 4.3.2 and 4.3.3 were performed at Herlev Hospital using the improved signal voltage readout (switched integration) during the summer of 2010. Probes were irradiated using a Varian Clinac® 2300 iX. The experiments presented in section 4.3.4 were made partly at Rigshospitalet in the summer of 2009 using the first version of the voltage readout setup (capacitor discharge sampling), and partly at Herlev Hospital in 2010 using the switched integrator setup. Irradiations at Rigshospitalet were performed using a Varian Clinac® 21 EX, while irradiations at Herlev Hospital were made using a Varian Clinac® 2300 iX.

4.3.1 Measurement reproducibility and signal-to-noise

The precision of the fully developed ME04 dosimetry system can be considered in two situations: Accumulated dose measurements and dose-per-pulse (DPP) measurements. The precision of accumulated dose measurements was determined as the measurement reproducibility obtained from 10 consecutive irradiations of 25 cGy accumulated dose each. This reproducibility was found to be on the order of 0.3 %, roughly corresponding to 0.7 mGy. Because the number of scintillation photons detected by the ME04 system is linearly related to the dose absorbed in the scintillator, measurement precision depends on the accumulated dose. The precision of pulse-resolved dose measurements was defined as the relative SD of the DPP. Although a 25 MU irradiation typically consists of approximately 900 radiation pulses, we used the part of the irradiation consisting of the last 500 pulses where linac dose rate fluctuations were minimal. In this way, the precision of individual DPP measurements was found to be 2.1 % (1 SD) at d_{max} (approximately

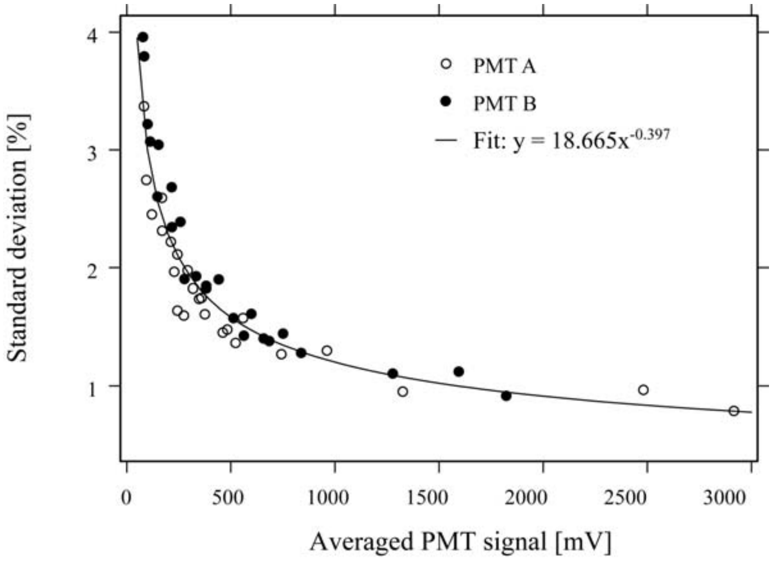

Figure 4.5: Relative SD plotted against average signal per pulse. Hollow circles: PMT A (stem signal). Filled circles: PMT B (scintillator signal). The solid line is a power law regression fitted to the data points.

0.277 mGy per pulse) for a scintillator of 1 mm length and 1 mm diameter. It should be emphasized that linac-inherent DPP fluctuations always contribute to the uncertainty of dose estimates. Measuring the target current within the 500 pulse interval revealed fluctuations of approximately 1.5 % (1 SD). The DPP precision depends on the overall system throughput and therefore on the size of both detected signal contributions (A and B). Figure 4.5 depicts the relative SD for signal contributions A and B as a function of the average detected light signal per pulse, for arbitrary depths, field sizes and probes of different scintillator size. A clear correlation between the magnitude of the detected signal and the relative SD is seen, emphasizing the importance of optimizing the light collection efficiency through the entire dosimetry system.

4.3.2 Dose rate dependence

Based on the study by Beddar et al. (1992c), organic scintillators are generally assumed to be independent of dose rate. Figure 4.6 supports this statement. A fiber-coupled organic scintillator probe (1 mm scintillator length) was subjected to a fixed delivered dose of 25 MU at dose rates from 100 MU/min to 600 MU/min at d_{max} depth, for a 10 cm x 10 cm reference field. The figure shows that any dependence of the scintillator response on dose rate cannot be distinguished from the 0.7 mGy measurement uncertainty.

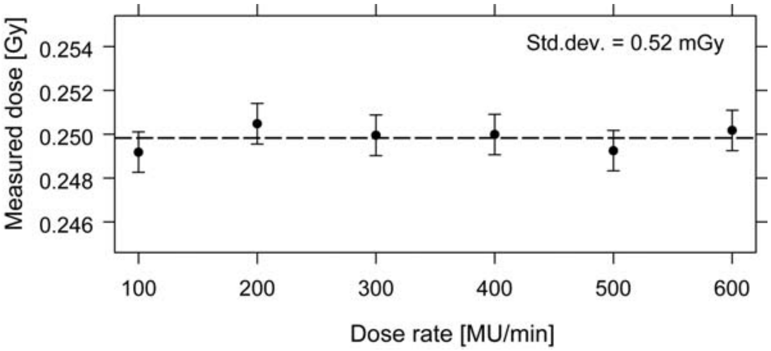

Figure 4.6: Dose rate dependence for 25 MU delivered at 100-600 MU/min for a 10 cm x 10 cm field at d$_{max}$.

4.3.3 Linearity with dose

To investigate whether our dosimetry system exhibited a linear dose response, the dose delivered to the fiber-coupled organic scintillator probe was varied between 1 MU and 100 MU for a fixed 300 MU/min dose rate at d$_{max}$ depth and 100 cm SSD. The field size was 10 cm x 10 cm. The response of the ME04 dosimetry system with absorbed dose was found to be linear in this dose range. Figure 4.7 depicts how well the system responds to differences in delivered dose, in terms of measured dose versus delivered dose (one delivered cGy corresponding to one delivered MU at reference field size and depth). A discrepancy between delivered and measured dose is seen when less than 10 MU are delivered. However, this is not unexpected since the number of delivered radiation pulses from the linac gets more variable for low delivered dose levels and do not necessarily follow a linear trend. For a 100 MU delivery, we counted approximately 3600 delivered radiation pulses; for a 1 MU delivery, we counted between 42 and 46 delivered radiation pulses instead of the expected 36, primarily due to the dose rate transient at the beginning of beam delivery. This transient behavior is discussed in detail in chapter 5.

4.3.4 Accuracy of stem removal

The stem signal is generated in three well-defined portions of the fiber. One part of the fiber is in the primary radiation field; another part is in the phantom, exposed to stray radiation from the main field. Finally, a large amount of fiber is outside the phantom, but is lying on the floor in the treatment room and exposed to stray radiation in the vicinity of the linac.

The dosimetry system prototype described in Beierholm (2007) and Beierholm et al. (2008) was based on a UV/blue chromatic removal configuration using the blue-emitting BCF-12 organic scintillator (Saint-Gobain Ceramics

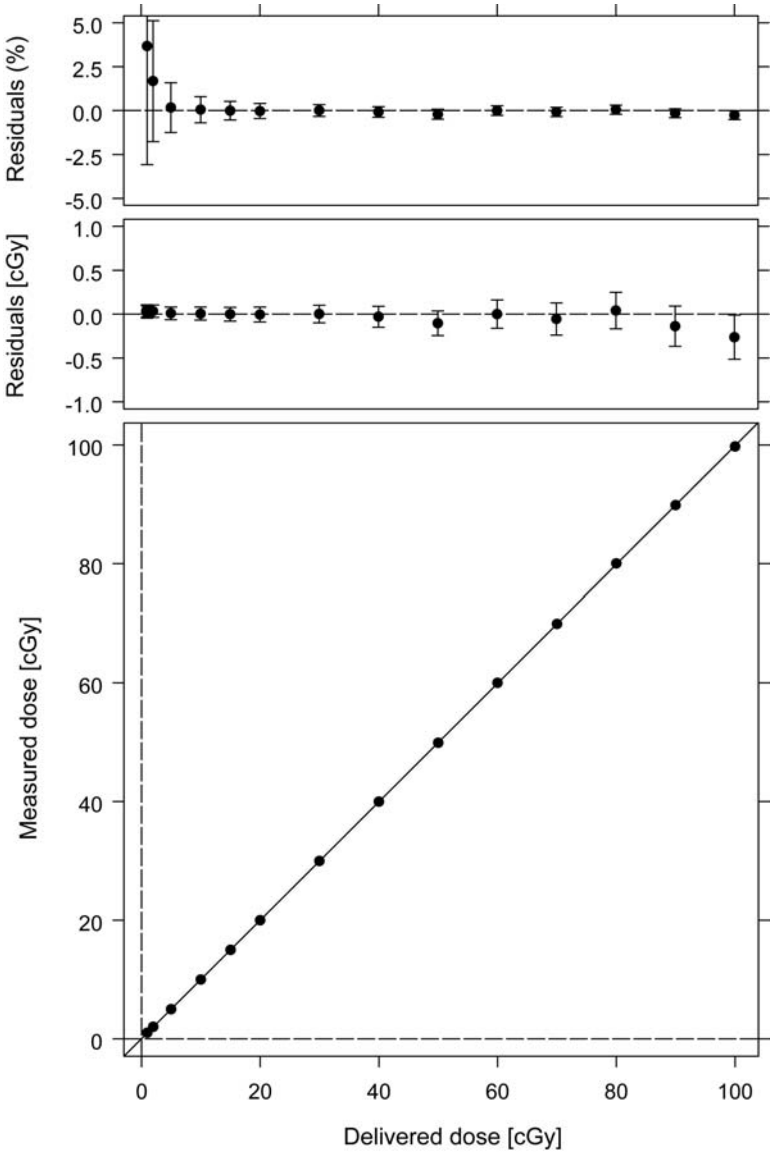

Figure 4.7: Measured dose as a function of delivered dose for 1-100 cGy delivered at 300 cGy/min dose rate, for a 10 cm x 10 cm field at d_{max}. For this irradiation configuration, 1 delivered MU corresponds to 1 cGy. Error bars (1 SD) corresponds to the accumulated dose uncertainty.

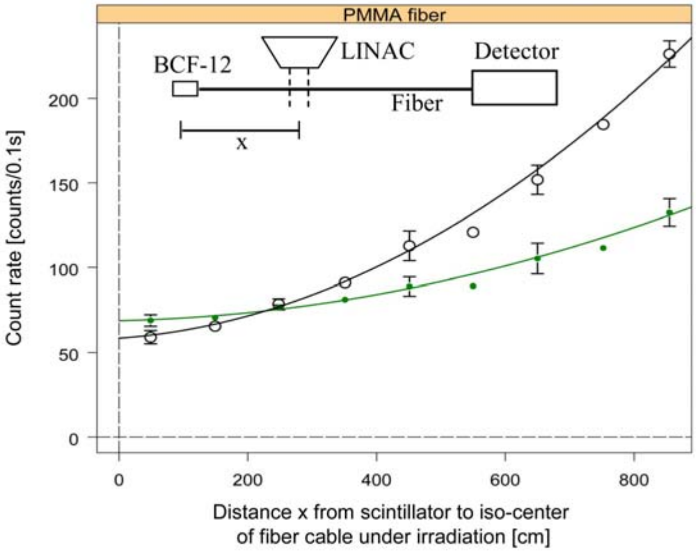

Figure 4.8: The fiber-filtration experiment performed in Beierholm (2007). Several positions along an ESKA^{TM} GH2001-P optical fiber are in the radiation field from a Varian 600SR linac, changing the transmitted signal values in the two spectral channels. Filled green circles: 420-470 nm wavelengths. Hollow black circles: 300-350 nm wavelengths. Error bars (1 SD) indicate stray radiation-induced signal variations caused by random orientation of the fiber cable.

& Plastics Inc., France). The system was able to suppress the stem signal to a level of approximately 30 mGy for a 300 MU irradiation (i.e. 1 %), and measured the absorbed dose with agreement within approximately 3.3 % when compared with reference data. The relatively poor accuracy and precision was believed to be caused by attenuation-induced signal filtration and overlapping stem signal and scintillation spectra. The modified blue/green configuration presented in this thesis was expected to provide a better wavelength discrimination between the stem signal and the scintillator signal, and should also be less sensitive to attenuation-induced signal filtration in the optical fiber. This section covers experiments performed to assess whether the new system configuration has lead to a more effective stem suppression.

Attenuation-induced signal filtration

The attenuation of light through an optical fiber of given length varies greatly with wavelength. For example, UV light is generally subject to higher attenuation than visible blue light. Because of this, light in two different wavelength domains are attenuated differently, yielding a filtration

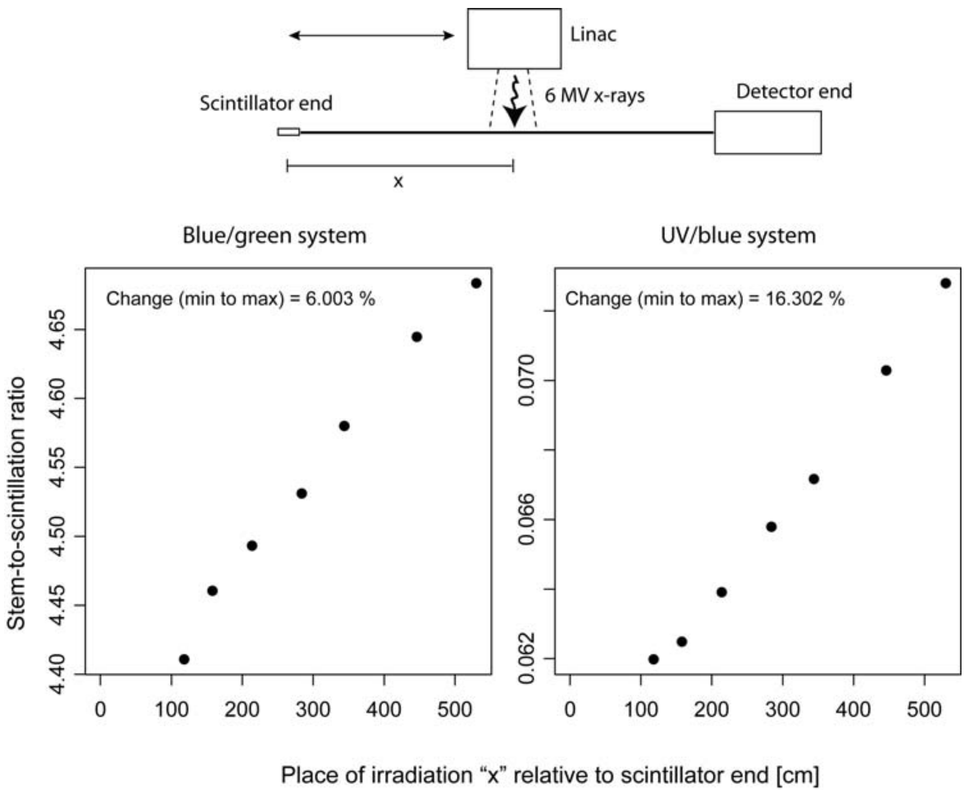

Figure 4.9: Stem-to-scintillation ratio for the blue/green and UV/blue system configurations as a function of irradiation position along the optical fiber.

of the signal components. This phenomenon was investigated in Beierholm (2007), resulting in the two curves shown in figure 4.8. The effect was significant for a system based on UV and blue wavelength channels, and was the main reason for the partial out-of-field calibration configuration presented in that work. The chromatic stem signal removal method is highly dependent on a constant stem signal spectrum, and might therefore be very sensitive to changes in signal transmission. To further examine how the stem signal and scintillation signal spectra change when transmitted through an optical fiber, an experiment at Rigshospitalet was performed. The experiment regarded a comparison between the old UV/blue detection system and the new blue/green system, using the Varian 21 EX to irradiate fiber-coupled scintillator probes at different positions along a fiber-coupled organic scintillator probe. The changed transmission through the fiber resulted in an increase in the stem-to-scintillation ratio. For the blue/green configuration, the stem-to-scintillation ratio is seen to change 6.0 % for a 4 m difference in fiber position. This corresponds to a change of 1.5 %/m. For the UV/blue configuration the change is 16.3 % over 4 m, corresponding to 4.1 %/m. From this simple experiment, it can be concluded that the blue/green-based chromatic removal system is approximately 2.7 times less sensitive to attenuation-induced signal filtration than the UV/blue-based system. However, care must still be taken to avoid large changes in the length of irradiated fiber, since the calibration and stem removal method relies on a constant stem-to-scintillation ratio.

Stray radiation

As discussed in Beierholm (2007), stray radiation from a linac induces a considerable stem signal in optical fibers. Stray radiation consists of low-energy photons scattered from the linac head and surroundings. The intensity of the stray radiation is much lower than in the primary radiation field, amounting to approximately 0.1 % at 1 m distance from the primary field (IEC, 1998). However, this can accumulate to a considerable stem signal contribution because several meters of fiber are typically lying on the treatment room floor, exposed to the stray radiation. Therefore, the orientation and amount of fiber in the treatment room should not be changed from measurement to measurement.

Under normal measurement conditions during this project, the fibers were arranged so that the length of fiber exposed to stray radiation was minimized and subject to minimal variations. To assess the significance of stray radiation-induced stem signal variations, however, we measured the dose for a fixed field and depth for several orientations of the optical fiber. As seen in figure 4.10, the fiber was arranged in random loops and wounds on the treatment room floor to vary the contribution to the stem signal. Figure 4.11 shows the dose measured, normalized to the mean value, for 13 different orientations of the fiber in the stray radiation field. The uncertainty of the dose estimate caused by this variation amounted to 0.4 % (1 SD). This is higher than the measurement reproducibility, which was approximately 0.3 % (1 SD), but still a small effect considering the variation of the different fiber orientations.

Field size dependence

In the standard measurement configuration, the organic scintillator is located in the isocenter of the beam and the fiber is kept straight. For the out of field configuration, the scintillator is located well outside the field while the fiber goes straight through the field. In these two situations, an increase in field size will increase the stem signal while the light from the scintillator will only be increased by a small amount. For accurate chromatic correction of the stem effect, the measured dose must therefore be independent of the amount of irradiated fiber. This can be tested in both measurement configurations.

Figure 4.10: Stray radiation-induced stem signal variation by placing varying lengths of fiber in the treatment room during irradiation.

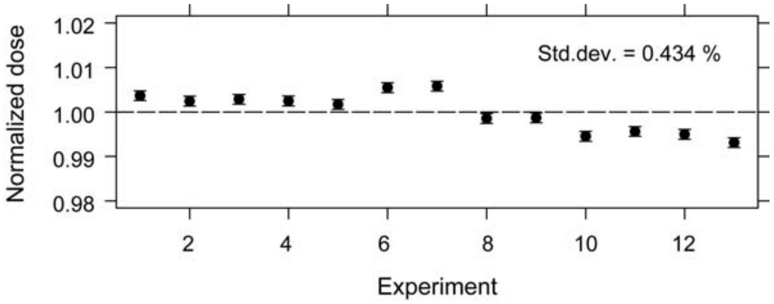

Figure 4.11: Dose measurement variation caused by the fiber being exposed to different levels of stray radiation in the treatment room. Experiment No. 11 and 12 correspond to the fiber arrangements shown in figure 4.10 right and lower left panel, respectively.

For the scintillator-out-of-field configuration, the measured dose should be close to zero, since the only contribution to the dose absorbed in the scintillator will be stray radiation. This hypothesis is tested in figure 4.12, where the dose measured by the scintillator out of field is plotted versus field size. The scintillator was calibrated to 0 mGy dose out of field for a 10 cm x 10 cm field. The measured dose is seen to be close to zero for field sizes between 3 cm x 3 cm and 10 cm x 10 cm, but is expectedly higher for larger fields due to the increased contribution from stray radiation at large fields.
For the scintillator-in-isocenter configuration, the increase in measured dose with field size should be equal to the output factor of the field. The output factor for a given field is a measure of how much dose that is delivered at the isocenter per delivered monitor unit, relative to a reference field which is typically 10 cm x 10 cm. Output factors are normally defined at d_{max}, which is approximately 1.5 cm for 6 MV x-rays. Measured output factors for field sizes from 3 cm x 3 cm up to 20 cm x 20 cm at 1.5 cm depth are shown in figure 4.13. The measurements are compared with hospital reference measurements performed with a PTW Semiflex ionization chamber in a water tank. From the residual plot, it is seen that the scintillator measurements agree with the ionization chamber within 1 % for all fields.

Depth dependence

A recent study by Lambert et al. (2009) suggested that the stem signal spectrum is dependent on the incident energy spectrum of a 6 MV x-ray beam, and hereby on the depth in a water equivalent medium. This statement was based on a spectroscopic study of the stem signal generated in an unnamed PMMA fiber at various depths in Gammex solid water. The resulting spectra differed with depth for wavelengths below 450 nm. The reason for this depth dependence was believed to be the change in the secondary electron spectrum coupled with the energy dependence of the Cerenkov effect. The authors recommended that any stem signal removal procedure that relied on the constancy of the stem signal spectrum be tested as a function of depth. We investigated this matter by making a depth-dose curve with the scintillator located out of field and the fiber going straight through the solid water phantom and radiation field. The field size was fixed at 10 cm x 10 cm, so no change in the intensity of stray radiation at the position of the scintillator was expected. If the chromatic removal method was robust, the estimated out of field dose should be independent of the fiber depth. The results are shown in figure 4.14, where estimated dose to the scintillator is plotted against depth. No significant deviation from the mean value was seen with depth, and the 0.8 mGy SD was comparable to the overall measurement uncertainty for the respective experimental conditions. The statement that the stem signal spectrum should be depth-dependent was therefore not supported by our data.

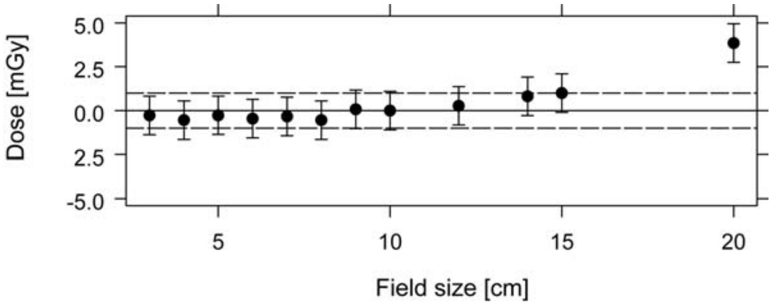

Figure 4.12: Measured dose versus field size, for square fields from 3 cm x 3 cm to 20 cm x 20 cm size. The scintillator is positioned out of field, and the fiber is going straight through the field at 1.5 cm solid water depth. Error bars (1 SD) correspond to the accumulated dose uncertainty.

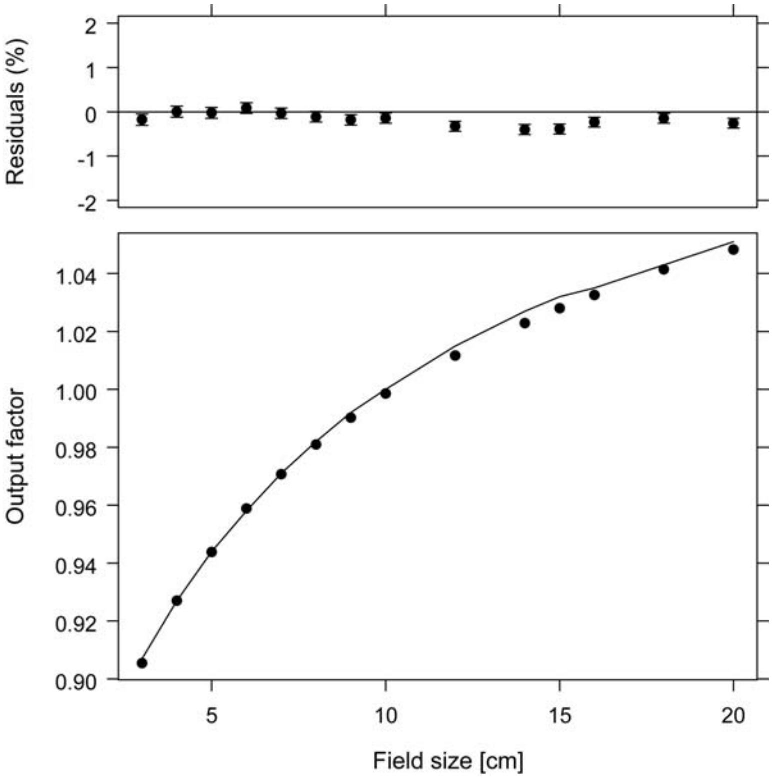

Figure 4.13: Measured output factor (OF) versus field size, for square fields from 3 cm x 3 cm to 20 cm x 20 cm size at 1.5 cm solid water depth. Filled symbols: Scintillator measurements. Line: Reference measurements of absorbed dose to water, measured using an ionization chamber. Error bars (1 SD) correspond to the accumulated dose uncertainty.

Figure 4.15 shows measured PDD curves for 6 MV x-rays for 4 cm x 4 cm, 10 cm x 10 cm and 20 cm x 20 cm fields. The curves have been normalized to the dose measured at 1.5 cm depth, and are compared with hospital reference data performed with a PTW Semiflex ionization chamber in a water tank. A water-to-solid water depth correction factor of 1.011 was applied in accordance with Seuntjens et al. (2005), in an attempt to correct for differences in electron densities between water and solid water. The residual plots show that most measurements agree within 2 %, although larger discrepancies are seen in the build-up region. However, the exact depth of the fiber-coupled organic scintillator is uncertain due to the large thickness of the specific probe used for these measurements. Because the PDD is most critically dependent on depth in and around the build-up region, this could explain the relatively large uncertainties evident from the residuals. Additionally, the material differences between water and solid water are not easily accounted for, and the correction factor used might be insufficient. Higher accuracy is therefore expected for PDD measurements performed in a water tank, or by comparing solid water measurements with reference measurements or Monte Carlo simulations performed in solid water. We will verify this expectation for the latter case in chapter 6.

4.4 Summary

- The ESKA$^{\text{TM}}$ Premier GH4001-P PMMA-based optical fiber was found to be the best choice for fiber-coupled organic scintillator dosimetry in this project, based on a comparison between different fibers.
- An in-house developed organic scintillator was evaluated for temporal stem signal removal applications, but the luminescent lifetime was not sufficiently long to meet the demands of the temporal removal method.
- The systematic calibration error caused by attenuation-induced filtration was found to be approximately 1.5 %/m for the new blue/green chromatic removal configuration and approximately 4.1 %/m for the old UV/blue configuration.
- The systematic error induced by stray radiation amounted to approximately 0.4 % for the new dosimetry system.
- The measurement precision of the new dosimetry system was found to be 0.3 % for accumulated dose measurements and 2.1 % for dose per pulse measurements at reference conditions (10 cm x 10 cm, 100 cm SSD, d_{max}).
- The system response was found to be linear with dose in the 1-100 cGy range and independent of dose rate.

- Output factor measurements at d$_{max}$ for 3 cm x 3 cm to 20 cm x 20 cm fields agreed with reference ionization chamber measurements within 1 %.
- Percentage depth dose measurements for 4 cm x 4 cm, 10 cm x 10 cm and 20 cm x 20 cm fields agreed with reference ionization chamber measurements within 2 %, except in build-up regions.

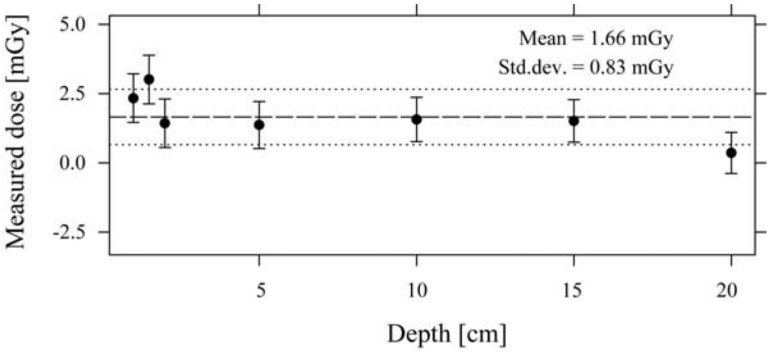

Figure 4.14: Measured dose versus depth, for 1 cm to 20 cm solid water depth. The scintillator is positioned out of field, and the fiber is going straight through a 10 cm x 10 cm field. Error bars (1 SD) correspond to the accumulated dose uncertainty.

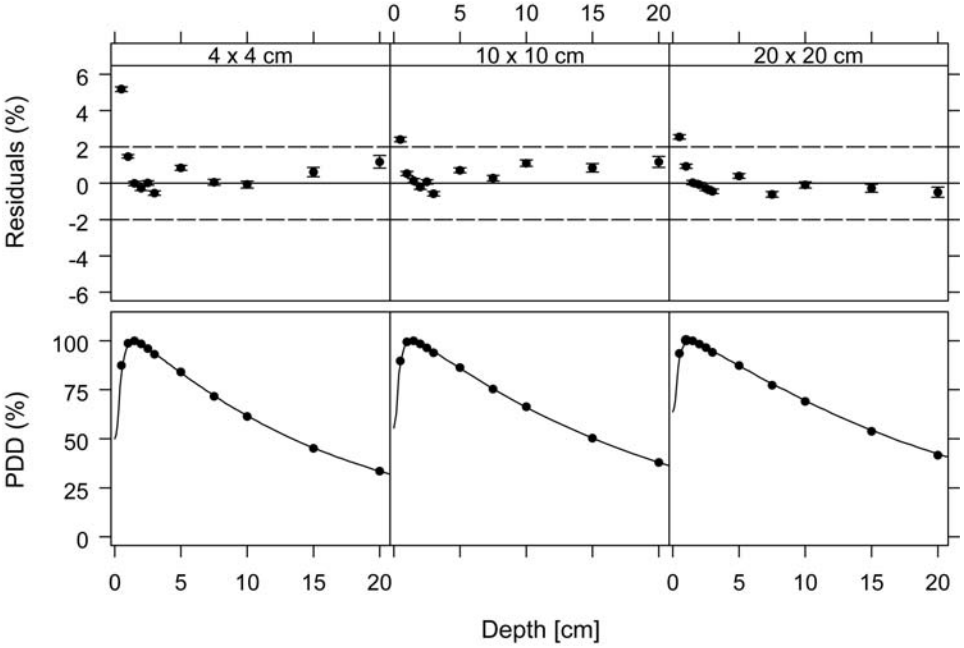

Figure 4.15: Measured percentage depth dose (PDD) in solid water for 4 cm x 4 cm, 10 cm x 10 cm and 20 cm x 20 cm square fields. Filled symbols: Scintillator measurements. Line: Reference measurements of dose to water, measured using an ionization chamber. Measurements have been normalized to the values at d_{max}. Error bars (1 SD) correspond to the accumulated dose uncertainty.

Chapter 5

Pulse-resolved dosimetry in clinical beams

As radiotherapy procedures such as arc therapy and gated radiotherapy are getting more common, a need for time-resolved dosimetry methods arises to verify the dose delivery of a medical linac on a small timescale. Treatment modalities exhibiting dynamic dose delivery (e.g. IMRT) consists of many low-dose fragments where changing of the shape of the radiation field or the gantry rotation speed happens on the timescale of a few radiation pulses. Additionally, the instantaneous dose rate within the pulses of radiotherapy beams is very high, easily reaching 50 Gy/s for normal beam delivery and well over 100 Gy/s for flattening-filter-free delivery. Therefore, dosimeters exhibiting μs-ms temporal resolution will prove advantageous in measuring the dose for each radiation pulse of a treatment, potentially yielding previously uncovered dosimetric information.

To our knowledge, no experimental studies have so far taken advantage of the fast (ns) response of organic scintillators to measure linac dose delivery on a pulse timescale.

5.1 Measurements using RC circuits

The experiments presented in this section were performed using the simplified voltage readout method (capacitor discharge sampling) described in section 3.2.1.

To assess the feasibility of the dosimetry system for pulse-resolved dosimetry, two fiber-coupled scintillator probes were exposed to 6 MV x-rays from a Varian Clinac$^{®}$ 21 EX at Rigshospitalet. The sensitive volumes of the probes were relatively large (respectively 3 mm and 4 mm scintillator length) to enhance probe light output, and hereby the precision of the dose measurements. The two probes were placed adjacent to each other at 1.5 cm depth in solid water, at 100 cm SSD. For each irradiation, a dose of 100

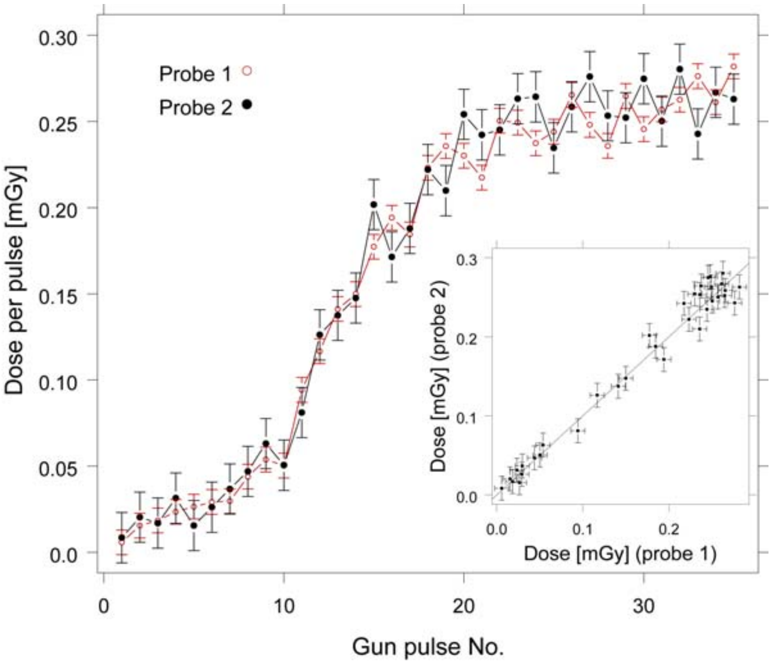

Figure 5.1: Dose delivery transient for the first 35 gun pulses of a 100 MU irradiation. Error bars indicate the predicted uncertainty on the measured DPP (1 SD). Insert: Correlation between scintillator probe 1 and probe 2.

MU was delivered at a dose rate of 600 MU/min. Field sizes between 3 cm x 3 cm and 10 x 10 cm were used for calibration of the probes.

5.1.1 A transient in the dose delivery

Figure 5.1 shows the measured dose per pulse (DPP) for the two scintillator probes, at the beginning of an irradiation at 10 cm x 10 cm field size. A transient in the dose delivery is clearly evident, with the dose per pulse slowly reaching the expected constant value of roughly 0.3 mGy per pulse. The insert shows that the dose measurements performed using the two scintillator probes are highly correlated. The dose delivery transient was also evident as a brief variation in the dose rate displayed on the treatment console at beam start-up, further indicating that the observed transient was indeed caused by the linac and not the dosimetry system. The transient behavior of medical linacs has also been seen in measurements using fiber-coupled Al_2O_3:C probes (Aznar et al., 2004). Another interesting observation of the pulse-resolved measurements was the apparent irregular radiation (gun) pulse frequency of the Varian 21 EX, sometimes resulting in missing pulses. This may have negligible influence on the total delivered dose since the effect is corrected for by the monitor ionization chambers and more pulses are

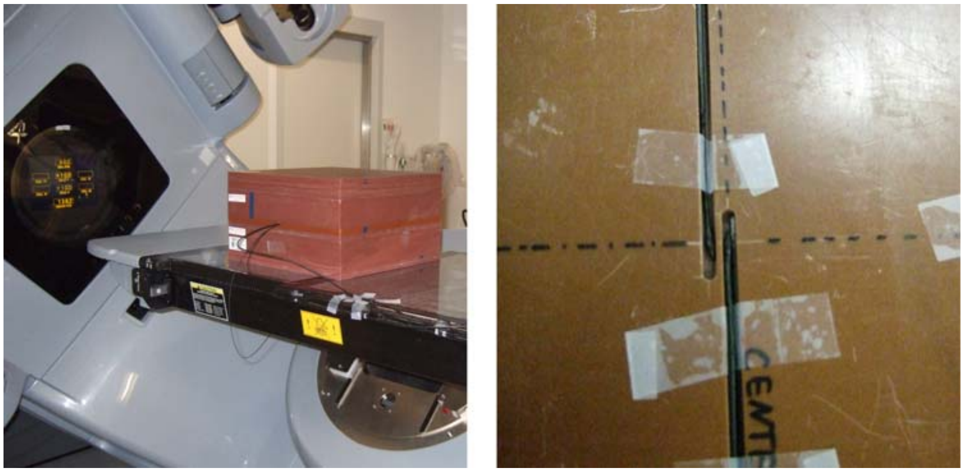

Figure 5.2: Left: RapidArc$^{®}$ measurements using 18 MV x-rays from a Varian Clinac$^{®}$ 2300 iX, irradiating two fiber-coupled scintillator probes at 8.5 cm solid water depth. Measurements were made with the probes arranged parallel (as shown) as well as perpendicular to the gantry rotation axis. If the removal of the stem signal was complete, the measured doses should be similar regardless of probe orientation. Right: The solid water slab used for housing two dosimeter probes. Probe No. 1 was centered while probe No. 2 was offset by a few millimeters.

delivered. However, for small dose segments, the dose delivery per pulse is highly relevant. It would therefore be interesting to see how the dose monitoring system corrects for e.g. missing pulses in the small dose segments of an IMRT treatment.

As described in section 3.2.1, the pulse-resolved measurements were performed using a sampling rate of 50 kHz, with each capacitor discharge pulse being recorded using 20 samples for each linac synchronization pulse. This approach resulted in large data files (on the order of 8 MB for a 100 MU irradiation), making data analysis and data acquisition impractical due to memory limitations. The dose per pulse was obtained from the sum of the 20 voltage readings. However, these readings could not be sampled simultaneously for the 4 PMTs. Only one analog-to-digital converter was employed in the setup, which meant that the 4 PMT signals were multiplexed. However, this led to a voltage reading offset of 1 μs between the 4 channels. These timing offsets led to errors in signal readings, and as a result the dose per pulse could not be measured with a precision better than 3 % for PMTs 1 and 2 (probe No. 1), and 6 % for PMTs 3 and 4 (probe No. 2).

5.1.2 Measuring a RapidArc® delivery

To test the scintillator system in a clinically relevant situation, two fiber-coupled scintillator probes were subjected to a 2 Gy RapidArc® delivery. Irradiations were carried out using a Varian Clinac® 2300 iX at Rigshospitalet. The plan was a modified prostate plan, made to deliver 2 Gy in a single arc to the center of a solid water phantom 17 cm high. To follow the modified treatment plan, the probes were irradiated at 8.5 cm solid water depth at 91.5 cm SSD. This was the only measurement series involving 18 MV and not 6 MV beam energy. The two probes were the same as in section 5.1.1 (3 mm and 4 mm scintillator length). Prior to arc delivery, the probes were calibrated at 10 cm x 10 cm field size, 100 cm SSD and 5 cm depth.
The arc irradiation was repeated four times for the fiber-coupled scintillator probes; three irradiations with the probes arranged with the fiber parallel to the gantry rotation axis (see figure 5.2, left), and one irradiation with the probes perpendicular to the rotation axis. This was done to evaluate the accuracy of the chromatic stem signal removal. Measurements were subsequently compared with measurements performed with Al_2O_3:C probes and an ionization chamber (Scanditronix-Wellhöfer FG65-G, connected to a Keithley 6517 electrometer).

Total dose delivered

The dose measured for each of the four arc deliveries are shown in table 5.1 for the two fiber-coupled scintillator probes. The dose measurements are seen to be very different for the two probes. In the case of probe No. 1, the delivered dose is significantly overestimated when the fiber is perpendicular to the rotation axis, indicating erroneous or incomplete removal of the stem signal. For the three arcs using the parallel configuration, the delivered dose is underestimated by approximately 0.7 %. The cause of these errors were believed to be erroneous calibration, possibly due to faulty PMT gain

Table 5.1: Measured total dose for the RapidArc® irradiations in perpendicular ($\perp$) and parallel ($\|$) orientations. Uncertainties are given as 1 SD for the four measurement values, and for the mean value as 1 SD of the mean.

Dosimeter	Arc No. 1 $\perp$	Arc No. 2 $\|$	Arc No. 3 $\|$	Arc No. 4 $\|$	Mean
Scintillator Probe No. 1	2.243 ± 0.011	1.988 ± 0.009	1.988 ± 0.009	1.985 ± 0.009	2.051 ± 0.064
Scintillator Probe No. 2	2.001 ± 0.009	2.001 ± 0.009	2.001 ± 0.009	1.993 ± 0.009	1.999 ± 0.002

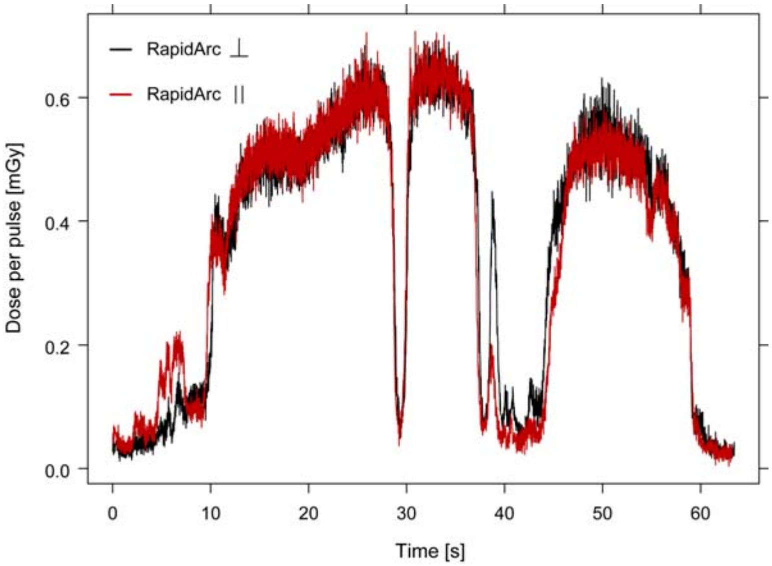

Figure 5.3: Measured dose per pulse for the entire duration of the RapidArc®. Black curve: Irradiation with scintillator probe No. 2 arranged perpendicular to the gantry rotation axis. Red curve: Irradiation with the probe parallel to the gantry rotation axis.

adjustment. Probe No. 2 gave consistently better results than probe No. 1; the measured dose agreed with the expected dose to within 0.4 % for all four arcs, also for the perpendicular orientation. By comparison, the mean dose for all four arcs was 2.002 ± 0.014 Gy measured with Al_2O_3:C. The mean total dose measured by the ionization chamber was only 1.840 ± 0.001 Gy. This significant discrepancy was however expected, because the considerable size of the chamber (650 mm^3 active volume) causes volume averaging-induced errors in situations of high dose gradients (for more on volume averaging in small fields, refer to chapter 6).

Dose delivered per pulse

For static beam delivery, a quick comparison with the measurements presented in section 5.1.1 showed that the dose delivered per pulse at 18 MV is approximately twice as large as for 6 MV.

A time-resolved view of dose delivery during the entire arc is shown in figure 5.3, where the dose per gun pulse is plotted versus time for probe No. 2. The figure indicated small differences between the perpendicular and parallel probe orientations - especially in the 5-8 and 38-45 seconds intervals. This may be due to the fact that the probe was offset from the center of the field by a few millimeters (see figure 5.2, right). As a consequence, the scintillator would not be in the exact same position in the two measurement

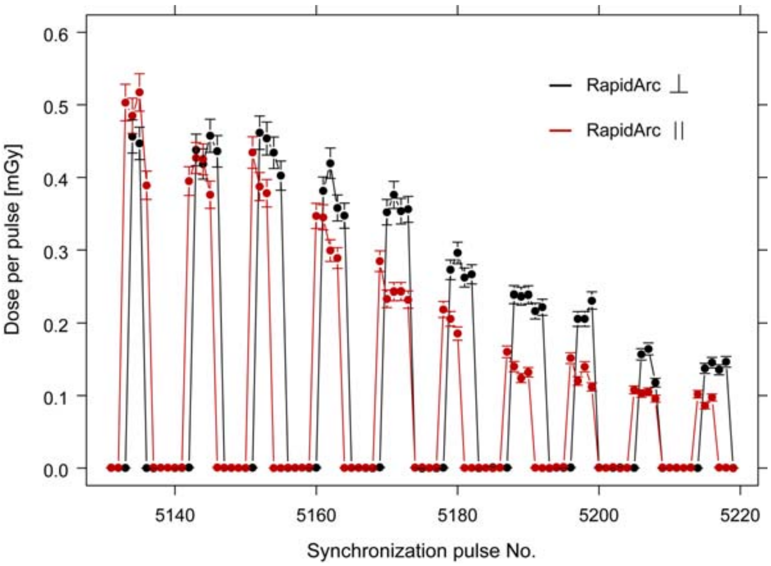

Figure 5.4: Measured DPP for a time window from 28.5 s to 29.0 s of the RapidArc®. Black curve: Irradiation with scintillator probe No. 2 arranged perpendicular to the gantry rotation axis. Red curve: Irradiation with the probe parallel to the gantry rotation axis. Error bars (1 SD) correspond to the DPP uncertainty, being roughly 5 % for this measurement setup.

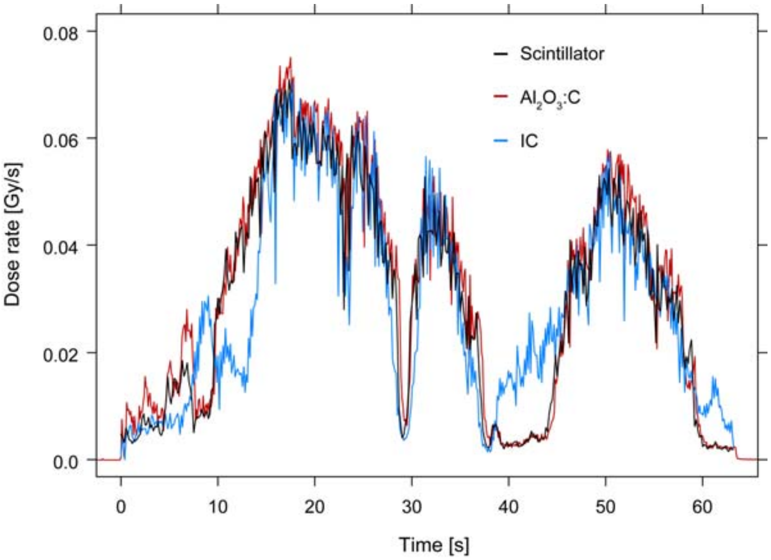

Figure 5.5: Measured dose rate in Gy/s for scintillator probe No. 2 (black), an Al_2O_3:C probe (red) and the FG65-G ionization chamber (blue), all in parallel orientation. The pulse-resolved scintillator measurements have been downsampled by a factor 180, corresponding to the 180 Hz synchronization frequency.

orientations. As the probe is subjected to high dose gradients throughout the irradiation, the difference in position will give a difference in absorbed dose (This effect was referred to as the "IMRT fingerprint" in Aznar (2005)). The dynamics of dose delivery are examined on a per-pulse basis in figure 5.4, where a subset of synchronization pulses of the entire irradiation is displayed. The chosen subset corresponds to the 28.5-29.0 s time window, where probe No. 2 is subjected to large dose gradients. The figure indicates how the dose rate is dynamically varied during the RapidArc® delivery. Comparing two or more of the four irradiations reveal that the dose delivery does not strictly maintain the same synchronization. Whether this is a feature of the RapidArc® delivery itself or of the data acquisition is unknown, considering the complexity of the dynamic dose delivery in arc radiotherapy. Figure 5.5 compares all three dosimetry methods on a Gy/s dose rate scale. The scintillator measurements were downsampled by a factor of 180 to account for the synchronized sampling frequency. The scintillator and Al_2O_3:C measurements exhibited very similar time-resolved dose profiles; the ionization chamber response was different as expected, considering the large detector volume.

The pulse-resolved scintillator measurements presented here indicate that the new dosimeter system is able to provide highly detailed temporal information of dose delivery. The qualitative observations of pulse-resolved dose delivery presented in figures 5.3, 5.4 and 5.5 illustrate the possibilities of pulse-resolved dosimetry in dynamic radiotherapy.

5.2 Measurements using switched integrators

The experiments presented in this section were performed using the modified voltage readout method (switched integrator sampling) described in section 3.2.2.

Compared with the RC circuit implementation, the introduction of switched integrators in the dosimetry system has reduced timing errors and intrinsic voltage fluctuations of the hardware. Because the voltage signals from the PMTs are held fixed for a specified amount of time using the "sample-hold" method, they need not be sampled simultaneously. This development has significantly improved the measurement precision of the dosimetry system. In addition, since each synchronization pulse is sampled only once, the amount of data and thereby the file size is reduced while maintaining the same dosimetric information.

New pulse-resolved dose measurements were performed, this time at Herlev hospital using a Varian Clinac® 2300 iX and fiber-coupled scintillator probes of 1-3 mm scintillator length. The probes were calibrated at 100 cm SSD, at 10 cm depth and 10 cm x 10 cm field size. As mentioned in section 3.4, the dose to the scintillators in the out-of-field configuration was measured using LiF TLDs.

Table 5.2 shows examples of pulse-resolved dose delivery characteristics for a probe of 1 mm scintillator length at different field sizes, depths and dose rates. For each irradiation, 25 MU were delivered. The transient number of pulses refer to the number of gun pulses that are delivered before the linac reaches a sustained, stable DPP. The transient number of pulses given in the table are the number of pulses exhibiting a DPP value being lower than the mean plateau value by more than two SDs. The precision of the measured DPP was given as 1 SD from the mean value of the last 500 pulses of the irradiation. This subset was chosen because the DPP was considered stable and constant in this region (plateau) of the irradiation. The measured DPP was averaged over the whole irradiation, which typically consisted of approximately 900 gun pulses. The expected DPP was calculated from the expected total dose, obtained from Monte Carlo simulations of a scintillator in solid water[1], divided by the total number of gun pulses. The difference between measured and expected DPP is given in % for each irradiation. A small change in the total number of delivered gun pulses was seen with dose rate; however, the effect is small, and more experiments are needed to present a quantitative statement on this matter. The measured DPP for fixed dose rate at different field sizes and depths coincided well with the expected values.

---

[1] For a thorough description of the Monte Carlo simulations that were applied, refer to chapter 6 and 9.

Table 5.2: Transient behaviour, number of pulses, DPP precision (1 SD), and the difference between measured and excepted DPP for irradiations at different field sizes, depths and dose rates.

Field side (cm)	Depth (cm)	Dose rate (MU/min)	Total dose (Gy)	Total no of pulses	Trans. no of pulses	DPP prec. (%)	Meas. DPP (mGy)	Exp. DPP (mGy)	DPP diff. (%)
10.0	1.5	100	0.250	896	16	2.2	0.2792	0.2790	0.1
10.0	1.5	200	0.250	899	18	2.3	0.2784	0.2781	0.1
10.0	1.5	300	0.250	900	15	2.1	0.2773	0.2778	-0.2
10.0	1.5	400	0.250	903	17	2.2	0.2769	0.2769	0.0
10.0	1.5	500	0.250	903	15	2.3	0.2757	0.2769	-0.4
10.0	1.5	600	0.250	905	20	2.2	0.2760	0.2762	-0.1
10.0	10.0	300	0.166	903	14	2.7	0.1826	0.1823	-0.6
10.0	20.0	300	0.095	902	15	3.6	0.1052	0.1039	-0.3
0.6	10.0	300	0.099	902	10	3.1	0.1091	0.1096	-0.4
0.6	20.0	300	0.051	903	14	4.1	0.0551	0.0577	-3.4

5.2.1 Dose delivery transient revisited

The transient behavior of medical linacs at beam start-up has been reexamined in figure 5.6. In this experiment, two probes of 2 mm and 3 mm scintillator length were irradiated at a field size of 10 cm x 10 cm at 10 cm and 20 cm depth, respectively. A dose of 25 MU were delivered at 300 MU/min dose rate.

Figure 5.6 (a) shows the DPP measured by the probe at 10 cm depth for the first 20 gun pulses of the irradiation. The measured target current per gun pulse is also shown, and has been normalized to the same scale as the measured mean DPP. The qualitative similarities between DPP and target current measurements indicate that the dosimetry system is able to accurately measure linac dose delivery on a per-pulse scale.

5.2.2 The beam quality factor

Figure 5.6 (b) shows the measured quality factor of the radiation beam, represented by the $\mathrm{TPR}_{20,10}$ value, obtained from the DPP simultaneously measured using the probe at 10 cm depth and the one at 20 cm depth. The $\mathrm{TPR}_{20,10}$ value is seen to fluctuate with a 5.8 % SD around a constant value of 0.667 for the first 20 pulses. For the total number of pulses, a mean value of 0.666 ± 0.001 was obtained. By comparison, measurements in water using an IBA CC13 ionization chamber (Sjöström et al., 2009) has shown a $\mathrm{TPR}_{20,10}$ value of 0.669 ± 0.001. Hereby, figure 5.6 (b) verifies the assumption that the radiation quality of the 6 MV beam is constant on a per-pulse level for the whole irradiation.

5.2.3 Transient behavior for two different linacs

The transient behavior seen in figure 5.6 (a) is characteristic to the individual Varian 2300 iX linac used for these measurements, and is distinctively different from the transient shown for the Varian 21 EX in section 5.1.1, as depicted in figure 5.1. Figure 5.6 (c) compares the transient behavior of the Varian 2300 iX with that of the Varian 21 EX. The figure shows the normalized DPP at beam start-up for five irradiations using the 2300 iX, compared with one irradiation using the 21 EX. All measurements in part (c) were made at 300 MU/min dose rate. While the Varian 21 EX apparently reaches stable dose per pulse after 20-30 pulses, the 2300 iX reaches a stable level after merely 5-10 pulses. These measurements show a clear dosimetric difference between the linacs concerning dose rate stability, potentially influencing the accuracy of linac dose delivery for small dose segments (on the order of 1 cGy). According to Konnoff et al. (2011), there appears to be general consensus in the literature on the under-delivering of dose for small dose segments, regardless of linac build. However, figure 5.6 (c) indicates that the degree of under-dosing is linac specific. An interesting application

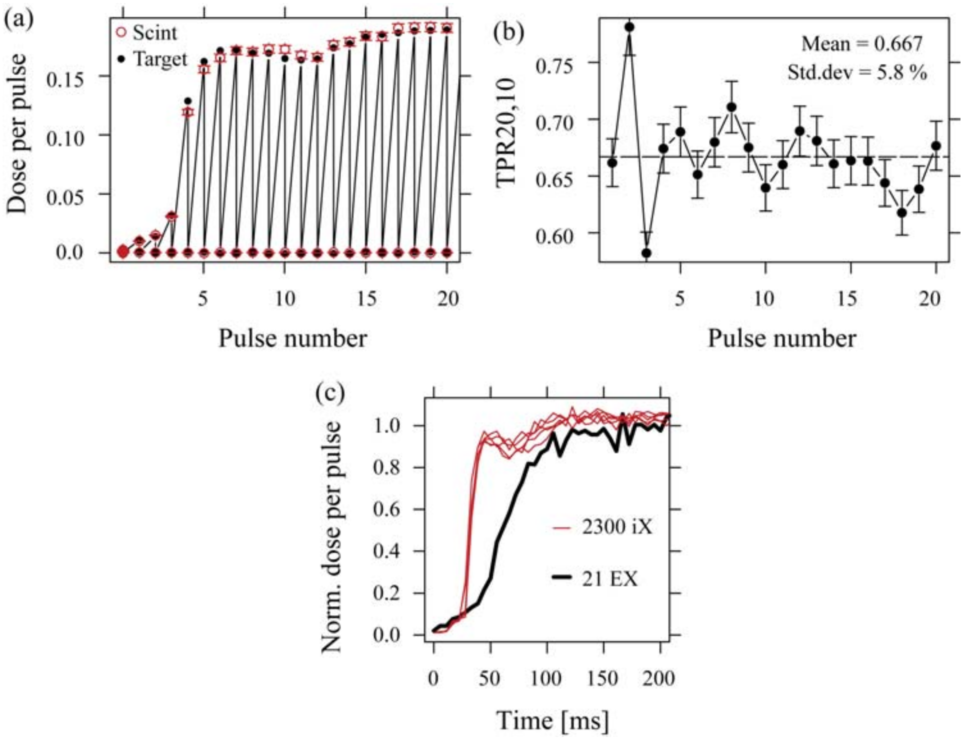

Figure 5.6: Transient behaviour for dose delivery at 300 MU min^{-1} dose rate. (a) DPP measured at 10 cm depth (hollow circles), with the linac target current (filled circles and lines) normalized to the mean DPP of the irradiation. (b) Measured $\text{TPR}_{20,10}$ per pulse, obtained using two fiber-coupled scintillator probes positioned at 10 and 20 cm depth. Error bars (1 SD) correspond to the uncertainty on DPP and $\text{TPR}_{20,10}$ per pulse, respectively. (c) Transient behaviour for the Varian 2300 iX (thin lines) and a Varian 21 EX (thick line).

of the new dosimetry system would be to compare the precision of dose delivery on a pulse scale for a representative assortment of linac builds used in hospitals, not only for static beam delivery but also for small IMRT plan segments. While the organic scintillators lack the great precision of the Scandidos Delta$^{4®}$ system, they exhibit water equivalence and a small size which will be advantageous for single-probe measurements in a well-defined geometry in a solid water phantom or water tank.

5.3 Summary

- Measurements of dose per pulse showed that linacs in general seem to exhibit a transient in dose delivery at the beginning of a static beam delivery. This effect is supported in the literature, but might not have any clinical significance since the under-dosing can be measured by the linac built-in monitor chambers and corrected.

- The dose delivered per pulse at 18 MV beam energy is generally twice as large as for 6 MV.
- Efforts were made to use the new dosimetry system to measure the dose per pulse during a simulated RapidArc® treatment delivery. The total dose measured using the fiber-coupled scintillator probes agreed with the planned dose, and some exciting knowledge about pulse-resolved dose delivery could be extracted from the measurements.
- The improved data acquisition setup of the dosimetry system hardware yielded higher measurement precision and resulted in smaller data files.
- The pulse-resolved measurements of transients at beam start-up were repeated and expanded with target current measurements, yielding good qualitative agreement between the measured dose and the target current.
- The quality factor for the 6 MV beam was measured per pulse and found to agree with the expected value. This confirms that the energy spectrum of the beam is stable during irradiation.
- The transient behavior was compared for two different linac builds, yielding a significant difference. This suggests that irregularities in pulsed dose delivery are linac-specific. Whether this could have any clinical significance remains to be investigated.

Chapter 6

Small-field dosimetry in clinical beams

Highly precise treatments such as stereotactic radiotherapy and IMRT apply small radiation fields and high dose gradients to ensure optimal dose conformity to small or irregular target volumes. Two physical phenomena are significant to the dosimetry of small fields that are not evident at larger fields: source occlusion and absence of lateral CPE.

Source occlusion

As mentioned briefly in section 1.1.1, the clinical x-ray beam is formed as a narrow beam of a few millimeters in diameter at the x-ray target. This is referred to as the direct beam source or spot size, and can be described as a gaussian-shaped blurring of the electron pencil beam hitting the target (IPEM, 2010). The x-ray beam travels through the flattening filter and monitor chambers and is collimated by jaws and MLCs, forming a clinically usable beam normally of 40 cm x 40 cm maximum field size at the linac isocenter. For most field sizes, the narrow direct beam source at the bottom of the x-ray target is fully visible at the point of measurement; however, the direct beam source is partly blocked by secondary collimator jaws, MLCs or cones for small fields. This so-called source occlusion is the cause of a significant drop in direct beam output, and hereby a drop in the delivered dose (see figure 6.1).

Absence of lateral charged particle equilibrium

An MV x-ray beam deposits radiation energy indirectly via secondary electrons generated primarily by Compton scattering. The point at which CPE exists is determined by the range of the secondary electrons - this applies along the propagation direction of the beam, but also in the lateral direction along the beam profile. The secondary electron range increases with beam

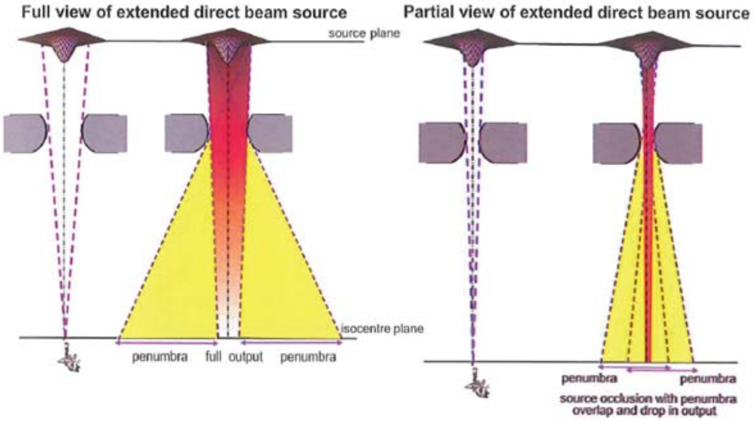

Figure 6.1: Partial occlusion of the direct-beam source for a small field. The partial blocking of the source when viewed at the point of measurement leads to a decrease in the delivered dose and a change in the lateral dose profile. Source: IPEM (2010).

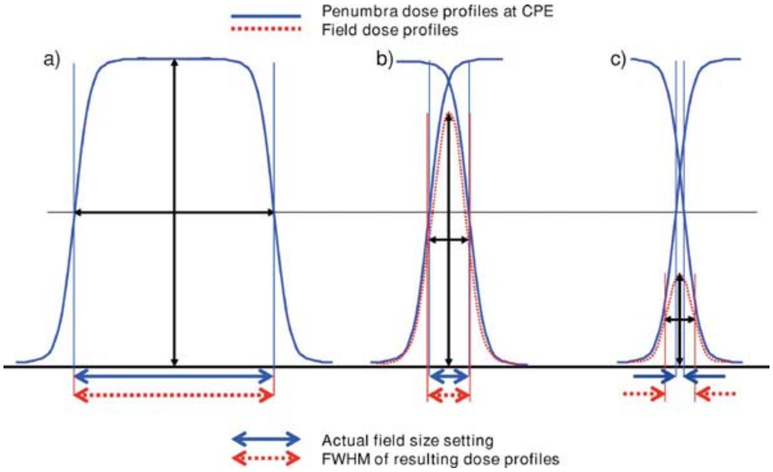

Figure 6.2: Illustration of how the field profile is affected by source occlusion and absence of CPE for a small field. Field penumbras overlap and the dose delivered at the field center is decreased. As a result, the "actual field size" defined by collimators will be smaller than the full width half maximum (FWHM). The determination of field size by FWHM will therefore overestimate the field size. Source: Das et al. (2008).

energy, and therefore the minimum field dimension required for lateral CPE increases with beam energy. For 6 MV beams, the lateral range of secondary electrons is approximately 1.3 cm in water (Li et al., 1995). Lateral CPE is not fulfilled for small fields, as the lateral extent of the field becomes smaller than the range of secondary electrons. As a result, the lateral field profile is dominated by penumbra with no plateau region of uniform dose, as seen in figure 6.2.

Dosimetric challenges of small-field radiotherapy

Dose measurements in small treatment fields put high demands on the dosimeters used - for instance, the use of standard ionization chambers are not recommended for use in fields smaller than 3 cm x 3 cm. Because of the small spatial extent of the field, dosimeter response will be subject to volume averaging-induced errors due to the large lateral dose gradients of the field profile. Therefore, a dosimeter that is large compared to the dimensions of the field will systematically estimate an erroneous central axis dose and overestimate the width of the field penumbra. In addition, the perturbation of the beam fluence due to the air-filled chamber becomes severe for a dosimeter of a size comparable to or larger than the size of the field. The main challenge of small-field dosimetry is therefore to use a dosimeter which consists of materials that minimize the perturbation of the radiation beam fluence, and is small enough to minimize volume averaging. Because of the lack of lateral CPE, the radiation spectrum of the beam differs from that of a reference beam, and a dosimeter calibrated at reference conditions will therefore give an erroneous dose estimate if the dosimeter signal is dependent on the constancy of the radiation spectrum.

Because of the current lack of reference data for small fields, the dose reading of a dosimetry system must be compared with Monte Carlo simulations and with other dosimetry systems to further the knowledge of highly localized dose delivery in small treatment fields. A new formalism for a small-field reference dosimetry protocol was suggested by Alfonso et al. (2008).

6.1 Small-field measurements with the IAEA

In May 2010, our research group participated in a small-field dosimetry study conducted by the IAEA, involving dose measurements in small static fields using the modified ME04 dosimetry system. The resulting measurements can be considered a preceding study to the small-field measurements and simulations presented in section 6.2.

Dose measurements in solid water for small static photon fields were performed at AKH in Vienna as part of a study conducted by the IAEA. The study had the following aims:

Figure 6.3: Measurement setup at AKH. The dosimeters were irradiated in solid water using 6 MV x-rays from an Elekta Precise® fitted with Brainlab M3™ μMLCs. The improvised fixation mount for the phantom was used to minimize alignment errors.

- To produce a good set of data on small-field output factors, especially for dosimeters for which few data exist: alanine pellets, TLDs, OSL dosimeters and possibly others.

- To derive relative correction factors for the respective detectors and compare those with Monte Carlo calculated correction factors. Full Monte Carlo simulations of the beam and dosimeters will be performed by the IAEA.

- To help decide what detectors would be suitable for reference dosimetry in composite fields. A follow-on project regarding composite field dosimetry is planned.

6.1.1 Measurement setup at AKH

As our contribution to the IAEA study, we performed small-field output factor measurements using a fiber-coupled organic scintillator, fiber-coupled Al_2O_3:C, and alanine pellets. Output factor measurements for 6 MV x-rays were performed using an Elekta Precise® linac fitted with a Brainlab M3™ add-on μMLC collimator system of 3 mm leaf width. All measurements were made at 95 cm SSD and 5 cm depth. Output factors were measured for field sizes of 0.6 cm x 0.6 cm, 0.9 cm x 0.9 cm, 1.2 cm x 1.2 cm, 1.8 cm x 1.8 cm, 2.4 cm x 2.4 cm, 3.0 cm x 3.0 cm and 10.0 cm x 10.0 cm. Field profiles were obtained using Gafchromic™ EBT2 radiochromic film. For every irradiation, a supplementary measurement was performed by one of our IAEA collaborators using a PTW Bragg Peak plane-parallel ionization chamber. This was done to correct for potential fluctuations in linac dose delivery.

A critical point of small-field measurements is to ensure correct alignment of the dosimeter with the center of the field. To position each dosimeter in the field center, a small piece of lead was placed in the center of the slab housing the probe, and the phantom was subsequently aligned with the field center using the linac positioning lasers and projected light field. A portal image was then acquired using the on-board imaging device of the linac to determine the real position of the field center. After image acquisition, the phantom was realigned and a new portal image was acquired to verify satisfactory centering of the lead marker. Finally, the lead marker was replaced by the dosimeter radiosensitive part. The solid water slabs were held in place by an improvised fixation mount (see figure 6.3).

Because of the configuration of the μMLCs, all 0.9 cm x 0.9 cm field irradiations had to be set up with an offset relative to the field center, and the dosimeter setup procedure was modified accordingly. All dosimeters were calibrated at 10.0 cm x 10.0 cm reference field size. For each irradiation involving the fiber-coupled organic scintillator, 25 MU were delivered at a dose rate of 400 MU/min; each output factor measurement was repeated at least 10 times. The length of the scintillator was 1 mm.

Table 6.1: Measured output factor (OF) versus field size (FS) for an organic scintillator probe, an Al_2O_3:C probe and alanine pellets.

FS (cm x cm)	Scintillator OF	Al_2O_3:C OF	Alanine OF
0.6	0.6399 ± 0.0001	0.6671 ± 0.0001	0.6387 ± 0.0022
0.9	0.7391 ± 0.0001	0.7606 ± 0.0002	0.7452 ± 0.0063
1.2	0.8035 ± 0.0001	0.8177 ± 0.0003	0.8094 ± 0.0022
1.8	0.8729 ± 0.0002	0.8803 ± 0.0003	0.8757 ± 0.0031
2.4	0.9077 ± 0.0001	0.9124 ± 0.0002	0.9184 ± 0.0042
3.0	0.9272 ± 0.0001	0.9304 ± 0.0003	0.9338 ± 0.0046
10.0	1.0000 ± 0.0002	1.0000 ± 0.0002	1.0000 ± 0.0036

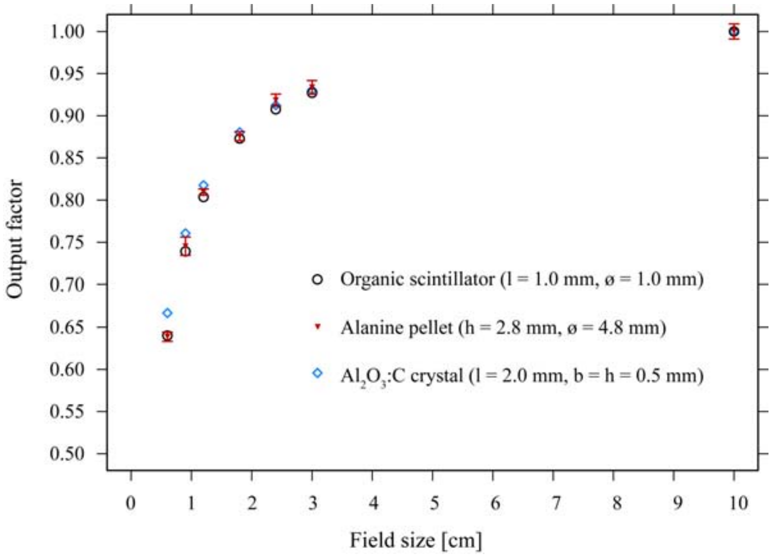

Figure 6.4: Measured output factors for selected field sizes between 0.6 cm x 0.6 cm and 10.0 cm x 10.0 cm. Measurements were performed using a fiber-coupled organic scintillator probe, an Al_2O_3:C probe and alanine pellets. Error bars (1 SD) are indicated, but are smaller than the symbols for the scintillator and Al_2O_3:C measurements.

6.1.2 Results

The output factor measurements for different dosimeters are presented in figure 6.4. For each dosimeter and field size, the output factor mean value and the SD of the mean is given in table 6.1. The measured output factors for the three dosimetry methods agreed to within 1.2 % down to 1.8 cm x 1.8 cm field size. For smaller fields, the Al_2O_3:C probe measured a higher output factor than the scintillator and the alanine pellet; for the 0.6 cm x 0.6 cm field, the discrepancy between the Al_2O_3:C and scintillator probes was 4.3 %. The scintillator and alanine measurements were in good agreement for all fields, the largest discrepancy being 1.2 %.
Because no reference data are available for small fields, it is not possible to determine which dosimeter that presents the best accuracy. The sensitive volume of the Al_2O_3:C crystal was half of the scintillator volume; this might lead to the assumption that volume averaging caused a lower measurement for the scintillator probe and the alanine pellets. However, Al_2O_3:C is not a water equivalent material, and the perturbation of the radiation field and the decreased electron range in the material compared to that in water might have caused a higher output factor measurement compared with lesser perturbing dosimeter materials. Only Monte Carlo simulations can provide an answer to this question.

6.2 Small-field dosimetry vs. Monte Carlo

Monte Carlo has become a powerful tool in radiotherapy and medical physics, and holds great potential for small-field dosimetry where methods for reference dosimetry have proven difficult. Simulated dose to water or tissue for a fully modeled linac could in principle provide a reference set of dose measurements for small and complex treatment fields. As pointed out by Das et al. (2008), Monte Carlo simulations must however not be considered a "golden standard" without careful experimental validation. To determine which dosimetry methods are the most suitable for small-field dosimetry, the dosimeters must therefore be carefully simulated and compared to simulated dose to water as well as to measured and simulated dose values for other dosimetry methods. This is beyond the scope of this thesis, and we have therefore limited this comparison to the case of fiber-coupled organic scintillators.

Small-field dose measurements were performed using 6 MV x-rays delivered by a Varian Clinac® 2300 iX at Herlev Hospital. As emphasized in the studies by Chow et al. (2005) and Klein et al. (2010), the dosimetric characteristics of a small field depends on the beam-shaping geometry. In this study, the square field size was varied between 0.6 cm x 0.6 cm and 10 cm x 10 cm using the secondary collimator jaws. All irradiations were performed at 100 cm SSD. The dose delivered was 25 MU per irradiation, at a dose rate of 300 MU/min. Output factor and percentage depth dose measurements were made using a probe of 1 mm scintillator length, while volume averaging measurements were performed with several probes of different scintillator size. For alignment of the scintillator to the beam isocenter, we used the same method as in section 6.1.1. The fiber-coupled organic scintillators were calibrated at 10 cm depth; the out-of-field dose to the scintillators during calibration was measured using LiF TLDs.

Monte Carlo dose calculations were made using a linac model developed using the BEAMnrc user code (Ottosson et al., 2010). Dose was scored to a scintillator voxel surrounded by solid water using the DOSXYZnrc user code, with a precision of approximately 0.5 %.

6.2.1 Output factors

The output factors for 10 cm x 10 cm down to 0.6 cm x 0.6 cm fields were measured at 10 cm depth, since this is the reference depth in water defined by the hospital. Figure 6.5 show the measured output factors compared with Monte Carlo simulations of a 1 mm x 1 mm x 1 mm polystyrene scintillator in solid water. Standard-field output factors (i.e. 3 cm x 3 cm field sizes and larger) were also compared with hospital reference measurements made with a PTW Farmer® ionization chamber in a water tank. The scintillator measurements agreed with Monte Carlo calculations with a maximum de-

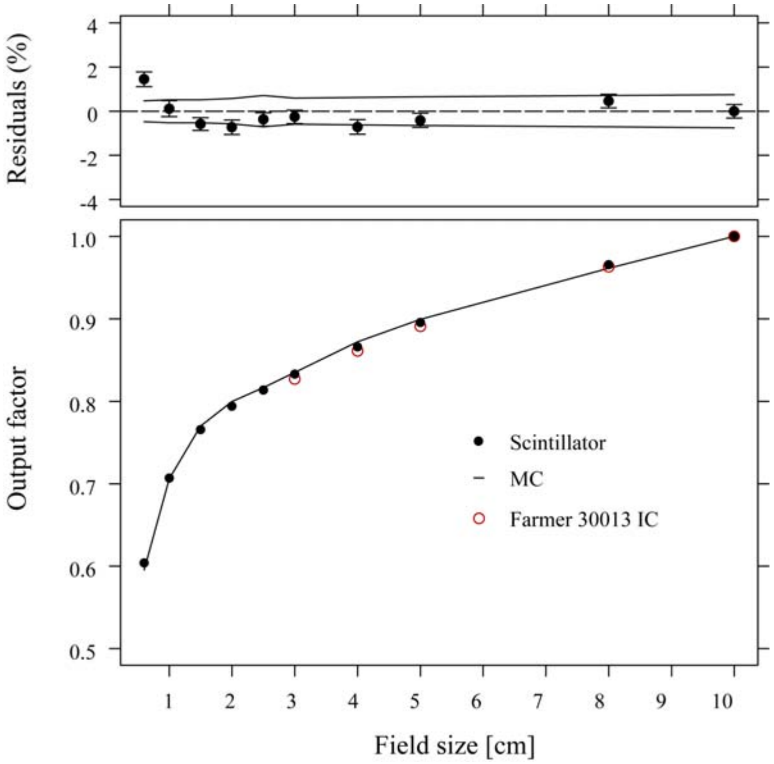

Figure 6.5: OF measurements for field sizes of 10 cm x 10 cm down to 0.6 cm x 0.6 cm at 10 cm depth. Filled circles: organic scintillator probes in solid water. Solid line: MC calculated dose to the scintillator in solid water. Hollow circles: reference IC measurements in water. Solid lines in residual plot represent uncertainties on MC simulations. Error bars (1 SD) correspond to the accumulated dose uncertainty.

viation of 1.5 %, and with reference ionization chamber measurements with 0.7 % maximum deviation. The Monte Carlo simulations differed from the ionization chamber measurements by maximally 1.3 %.

6.2.2 Percentage depth dose

Measurements of percentage depth dose were made for a 10 cm x 10 cm reference field and a 0.6 cm x 0.6 cm small field, for depths of 1 cm down to 20 cm in solid water. Measurements were normalized to the values at 1.5 cm depth. Monte Carlo simulations were again performed for a 1 mm x 1 mm x 1 mm polystyrene scintillator in solid water and compared with the scintillator measurements. The results are shown in figure 6.6. For both field sizes, most measurements agreed with Monte Carlo to within 0.9 %. The only exception was the depth-dose measurement for the small field at 20 cm depth, which was 3.2 % lower than the simulated value. This discrepancy

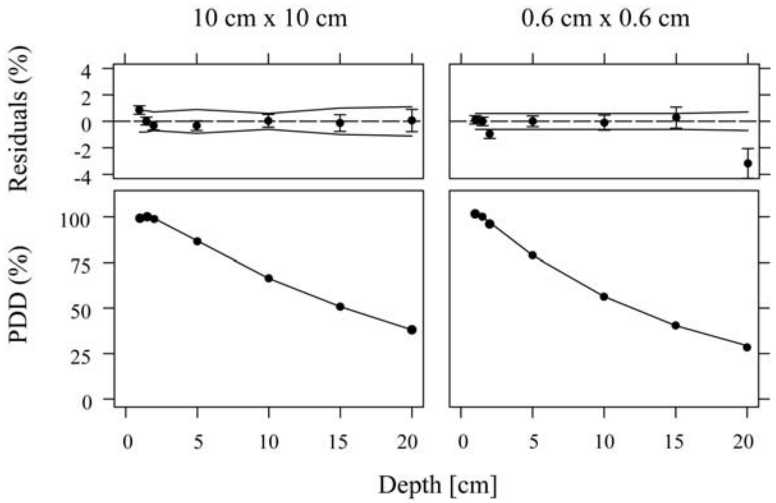

Figure 6.6: PDD measurements for an organic scintillator probe in solid water for 10 cm x 10 cm field size (left), and for 0.6 cm x 0.6 cm field size (right). Solid line: MC simulated dose to the scintillator in solid water. Measurements have been normalized to the values at 1.5 cm depth. Solid lines in residual plot represent uncertainties on MC simulations. Error bars (1 SD) correspond to the accumulated dose uncertainty.

was believed to be caused by an alignment error.

6.2.3 Volume averaging

To assess the degree of dose underestimation due to volume averaging, dose was measured for the 0.6 cm x 0.6 cm field at d_{max} as a function of scintillator size, for dosimeter probes of scintillator length between 1 mm and 10 mm. The measurements were compared with Monte Carlo simulations and radiochromic film measurements. The simulations were carried out for scintillator voxels of sizes between 1 mm x 1 mm x 1 mm and 10 mm x 1 mm x 1 mm. In the case of film measurements, the lateral dose profile of the 0.6 cm x 0.6 cm field was obtained using Gafchromic^{TM} EBT2, calibrated in the 1-5 Gy dose range and read out using a commercial flatbed scanner and Risøscan software. The estimated output factor was obtained from the field profile in the following manner: For a 1 mm long scintillator, the dose estimate was averaged over a 1 mm interval around the central axis (i.e. dose maximum) of the profile. For a longer scintillator, the dose estimate was obtained over a larger interval of the profile, resulting in a lower average dose estimate. This was done for averaging intervals from 1 mm to 10 mm to give a simplified impression of the volume averaging.

The normalized dose estimates are shown for fiber-coupled organic scintillators, Monte Carlo and film in figure 6.7. The use of scintillators longer

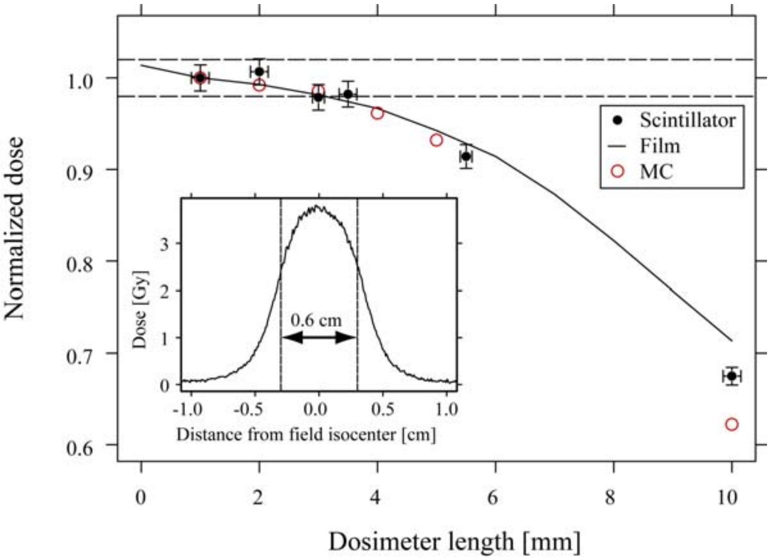

Figure 6.7: Estimated isocenter dose in a 0.6 cm x 0.6 cm field at d_{max} as a function of dosimeter size. Data are normalized to values corresponding to 1 mm dosimeter length. Solid circles: dose measured with organic scintillator probes in solid water. The x and y error bars are the uncertainty estimates of the scintillator length and probe-isocenter alignment, respectively. Hollow circles: MC calculated dose for a scintillator in solid water. Error bars are smaller than the symbols. Solid line: dose measured with radiochromic film. The dashed lines indicate the ± 2 % deviation from the normalization point. Insert: lateral dose profile of the 0.6 cm x 0.6 cm field, measured with radiochromic film subjected to a 500 MU irradiation at d_{max}.

than 2 mm is seen to induce a dose underestimation of 2 % or higher, and dosimeters this large are therefore not recommended for use in small-field dosimetry. Large discrepancies between the scintillator, Monte Carlo and film are evident when the dosimeter is comparable to or much larger than the size of the field; for lengths shorter than 5 mm, however, the dose estimates obtained with the scintillator, film and Monte Carlo agree within 2.1 %.

By comparison with Monte Carlo, the experiments presented in this section showed that fiber-coupled organic scintillators are able to measure the dose delivered in small fields with high accuracy. It should be emphasized that the comparison with Monte Carlo does not alone provide the true value of measurement accuracy, since the Monte Carlo model is not entirely independent of input obtained from measurements. The particular Monte Carlo model used was however commissioned for standard fields, and was therefore built on reference dose measurements performed in 3 cm x 3 cm to 30 cm

x 30 cm fields. In the context of small fields, the Monte Carlo model could therefore be considered independent of measurements.
For a complete Monte Carlo model of small fields, built from first principles, parameters such as electron beam spot size and cut-off energy must be carefully considered (Scott et al., 2008). Especially the spot size is important, as the simulated output of small fields is directly related to source occlusion, which depends on the size of the source.

6.3 Summary

- Small fields in radiotherapy are characterized by source occlusion and absence of lateral charged particle equilibrium, resulting in a drop in output and a narrow lateral field profile.

- There is no clear consensus on the definition of what field sizes can be considered "small". Lateral electronic equilibrium is not fulfilled for lateral lengths smaller than roughly 1.3 cm for 6 MV beams. Standard ionization chambers are not recommended for use in fields smaller than 3 cm x 3 cm due to their large size.

- The dose profile of a small field depends on how the field is collimated. As such, fields shaped using MLCs differ from those shaped by cones or jaws.

- Small-field output factor measurements were performed at AKH in Vienna, using fiber-coupled organic scintillators and Al_2O_3:C crystals as well as alanine pellets. The resulting output factors agreed for the scintillator probe and alanine pellets within 1.2 %, but were significantly lower than Al_2O_3:C values for small fields.

- Additional small-field measurements using scintillator probes were performed at Herlev Hospital and compared with Monte Carlo simulations. Measurements and simulations of output factors, percentage depth dose and volume averaging were performed.

- The output factor measurements agreed with simulations to within 1.5 % down to 0.6 cm x 0.6 cm field size.

- The percentage depth dose measurements for the 0.6 cm x 0.6 cm field agreed with simulations to within 0.9 % except for one measurement.

- The volume averaging effect was demonstrated using fiber-coupled organic scintillators, radiochromic film and Monte Carlo for the 0.6 cm x 0.6 cm field. The measurements and simulations showed that dosimeters should not be longer than 2 mm on the longest axis to prevent significant dose estimation errors due to volume averaging.

Chapter 7

Conclusions

Summary

This thesis summarizes the development, adaptation and applications of a fast-acquisition dosimetry system based on fiber-coupled organic scintillators, developed at the Radiation Research Division from 2008 to 2011. The idea of such a system was conceived in the period 2006-2007; this PhD project is built upon that study, expanding and refining it to reach the presented result.

The method has been tested using clinical x-ray beams from medical linacs at Rigshospitalet, Herlev Hospital and AKH. The measurements have covered basic experimental parameters such as measurement reproducibility, linearity and dose rate independence, to standard dosimetric evaluation of output factors and percentage depth dose, and finally progressing to pulse-resolved measurements of dynamic dose delivery and comparisons with Monte Carlo simulations in small static fields. The development and measurement process is summarized in table 7.1, which can be seen as the ”spec sheet” of the new dosimetry system.

At the beginning of this project, an important objective was to find the optical fiber most suitable for the new detector system. In-house made organic scintillators for temporal stem removal were also investigated. However, it was the continued development of the original scintillator-based dosimetry system that showed the way to the pulse-resolved dosimetry experiments presented in chapter 5. The change from a blue to a green scintillator has evidently and significantly improved the accuracy of stem removal. The Perkin-Elmer PMTs were replaced by the Hamamatsu modules, resulting in higher dynamic range of the dose measurements as well as allowing a smaller detection system form factor.

The fast data acquisition is an entirely new development of the scintillator-based dosimetry system, enabling time-resolved measurements of dose delivery with high temporal resolution. Measurements of dose per pulse for static as well as dynamic beam delivery have uncovered dosimetric characteristics that might prove relevant in dose verification and QA of modern radiotherapy. The refined voltage readout design of the system has improved the measurement precision, allowing the use of smaller scintillator probes of better spatial resolution. The method therefore also holds promise in the context of small-field measurements; the experiences at AKH and Herlev show that fiber-coupled organic scintillators can measure dose delivery in small static fields with high accuracy.

Main conclusions

- Applying the chromatic removal method (Fontbonne et al., 2002; Frelin et al., 2005) was found to be an effective and robust method for removing the parasitic stem signal generated in the optical fibers. Alternative methods, such as hollow-core photonic crystal fibers and long luminescent lifetime scintillators, were also evaluated but found to be insufficient.

- The accuracy and precision of dose measurements was evaluated in static MV photon beams, and was found to be sufficient for the new system to be used for pulse-resolved dosimetry applications in modern radiotherapy. The precision of dose-per-pulse measurements was in the 1-4 % range, and good agreement with linac target current measurements was found.

- A comparison between small-field dose measurements and Monte Carlo simulations was made for static MV photon beams down to 0.6 cm x 0.6 cm field size. This comparison showed that there was good agreement between dose measurements performed with the new dosimetry system and Monte Carlo simulated dose for small fields. The high measurement accuracy indicates that the dosimetry system is a candidate for small-field reference dosimetry.

- Time-resolved dose measurements of a dynamic radiotherapy treatment exhibited good agreement with Al_2O_3:C measurements, concerning total dose as well as time-resolved dose delivery. Furthermore, the pulse resolution of the new system provided additional qualitative information about dynamic dose delivery that could not be obtained with Al_2O_3:C.

In view of these main conclusions, the new pulse-resolved dosimetry system is found to hold great potential for modern radiotherapy applications, such as stereotactic radiotherapy and intensity-modulated radiotherapy.

Future work

As evident from table 7.1, some dosimetric characteristics of the scintillator system were not evaluated in this project. This regards the dependence of dosimeter response on temperature, energy and irradiation angle, as well as the resistance of the fiber-coupled scintillators to radiation-induced damage. However, these matters have been discussed in the literature (Beddar et al., 1992c; Archambault et al., 2007; Frelin et al., 2008a); we have therefore assumed that our system exhibits the same degree of independence of temperature, energy, angle and radiation damage as stated in the studies listed here. However, the validity of these assumptions must be verified to ensure that the system is sufficiently well characterized for potential clinical implementation.

The measurements of dynamic radiotherapy delivery and the performance of the dosimetry system regarding small static fields have shown the future applications of this method. The next move could therefore be i) an extensive measurement vs. Monte Carlo study of non-equilibrium dosimetry, such as encountered in small-field radiotherapy, and ii) dose verification of advanced dynamic treatments such as IMRT and/or arc therapy.

Table 7.1: Specifications of the new dosimetry system.

System characteristics		
Dosimeter material	BCF-60 polystyrene-based organic scintillator	
Dosimeter size	1 mm diameter, 1 to 10 mm length	
Dose response signal	Scintillation (green light)	
Light guide	GH4001-P PMMA-based optical fiber	
Dosimeter-hardware connection	SMA	
Data acquisition software	MEView v.361	
Detection hardware	ME04 (Risø DTU)	
Stem signal removal	Chromatic	
Measured wavelengths (approx.)	400-465 & 635-725 nm	520-580 nm
Photodetectors	Hamamatsu H5784	Hamamatsu H5784-02
PMT voltage readout	ACF2101 switched integrator circuits	
Target current measurement	ACF2101 switched integrator circuit	
Temperature measurement	Thermistor inside hardware casing	
Data acquisition	(1 + 2) x NI US-6218 DAQ	
Data sampling rate	50 kHz maximum	
Data sampling source	a) Internal (i.e. uniform sampling) or b) External (e.g. linac sync signal)	
Dosimetric performance		
Total dose precision	0.3 %	
DPP precision	2.1 %	
Dose rate dependence	Negligible (Measured for 100-600 cGy/min in sec. 4.3.2)	
Linearity with absorbed dose	Yes (measured for 1-100 cGy in sec. 4.3.3)	
Energy dependence	Negligible (not measured, see sec. 2.2.2)	
Temperature dependence	Negligible (not measured, see sec. 2.2.3)	
Radiation damage resistance	Up to approx. 1 kGy (not measured, see sec. 2.2.4)	
Angular dependence	Negligible (not measured, see sec. 2.2.5)	
Measurement agreement		
Output factors 4 x 4 to 20 x 20 cm^2	Within 0.5 % (Compared with reference IC)	
Output factors 0.6 x 0.6 to 4 x 4 cm^2	Within 1.5 % (Compared with MC simulations)	
Percentage depth dose 10 x 10 cm^2	Within 0.9 % (Compared with MC simulations)	
Percentage depth dose 0.6 x 0.6 cm^2	Within 0.9 %* (Compared with MC simulations)	

Chapter 8

Paper I: Investigation of linear accelerator pulse delivery using fast organic scintillator measurements

A.R. Beierholm, C.E. Andersen, L.R. Lindvold and M.C. Aznar

Abstract

Fiber-coupled organic plastic scintillators present an attractive method for time-resolved dose measurements during radiotherapy. Most organic scintillators exhibit a fast response, making it possible to use them to measure individual high-energy X-ray pulses from a medical linear accelerator. This can be used in complex treatment procedures such as gated intensity-modulated radiotherapy (IMRT), where the advantage of dose rate measurements of high temporal resolution is highly emphasized. We report on development of a fast data acquisition scintillator-based system as well as measurements performed on Varian medical linear accelerators, delivering 6 MV X-ray beams. The dose delivery per radiation pulse was found to agree with expectations within roughly 1%, although minor discrepancies and transients were evident in the measurements.

8.1 Introduction

Ionization chambers, semiconductor diodes and MOSFET detectors are commonly used to effectively measure the doses delivered by medical linear accelerators (linacs) in external beam radiotherapy. However, few studies concern dose delivery on the actual timescale of accelerator output (Clift et al., 2002;

Benoit et al., 2008b). Modern linacs for radiotherapy, such as the Varian 2100 series, deliver pulsed beams of high-energy X-rays. The duration of each pulse is typically around 5 ms, whereas the time between pulses is on the scale of 3 ms; thus, the radiation is delivered with very high instantaneous dose rates. Benoit et al. (2008b) used cerium-doped optical fibers to study linac pulse characteristics through the fast radioluminescence (RL) from the SrS:Ce,Sm phosphor, but did not calibrate the RL response to perform actual dose measurements. Fiber-coupled organic scintillators can be used for dose measurements in radiotherapy beams, and the dosimetric characteristics of a scintillator-based system have been tested elsewhere (Archambault et al., 2006a; Beierholm et al., 2008). In dynamic treatments such as gated IMRT, where accelerator pulses are turned on and off synchronized with the breathing cycle of the patient, it is advantageous to be able to measure the delivered dose on a fast timescale. One of the most advanced quality assurance systems presently on the market, the Delta 4 (Scandidos, Sweden), can measure linac dose per pulse to an accuracy of 0.6% standard deviation, using an array of 1069 p-Si diode detectors (Sadagopan et al., 2009). However, such a system does not exhibit the water equivalence and possibility for in vivo applications that fiber-coupled organic scintillators can offer. As commercial organic scintillators exhibit nanosecond-scale scintillation decay, a system for fast data acquisition can be constructed and used to measure dose per pulse delivered by a linac. In this paper, we report on the development of such a data acquisition setup. Measurements using hospital linacs have been performed to test the dose per pulse measuring ability of this new dosimetry system.

8.2 Experimental setup

Organic scintillator fibers of 1 mm diameter (BCF-60, Saint- Gobain, France) were coupled to Mitsubishi Rayon GH-4001 PMMA optical fibers in a manner similar to the one described by Marckmann et al. (2006) and Beierholm et al. (2008). Careful polishing of the scintillator and fiber end faces was performed before coupling using 0.3 mm grain size polishing sheets (Thorlabs, Germany). The scintillator was bonded to the distal end of the fiber using Norland 68 refractive index-matching glue. The light signal from the fiber probe was detected using Hamamatsu H5784 photomultiplier tubes (PMTs) operated in current mode. Parasitic light generated in the fiber during irradiation, the so-called stem effect, was corrected for using the chromatic removal method described in Frelin et al. (2005) and Beierholm et al. (2008), using optical components similar to the ones used in Frelin et al. (2005). Time-resolved dose measurements were performed using pulsed 6 MV X-ray beams delivered by a Varian 21EX at the Copenhagen University hospital. For each irradiation session, the dose was measured in a 30 x 30 x 30 cm^3

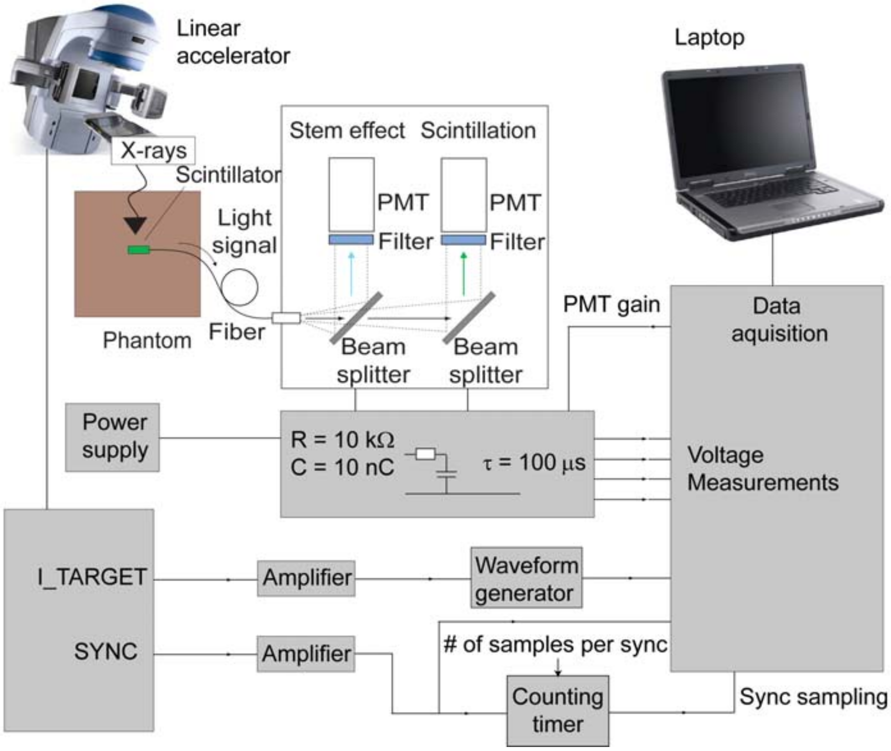

Figure 8.1: Schematic view of the data acquisition setup. Voltage measurements from the PMTs are acquired on a laptop PC, and data acquisition coincides with the synchronization pulses of the linac itself.

solid water phantom using two fiber probes, each coupled to its own detector system. The data acquisition setup is shown schematically in figure 8.1; the two PMTs of the detector system are connected to an RC circuit with a resistance of 10 kU and a capacitance of 10 nC, giving the system a characteristic time constant of 100 ms. This is a sufficient time resolution for us to distinguish each pulse, since the RC circuit capacitor charge decays completely before the next pulse. While measuring the voltage signals from the PMTs, the linac synchronization pulses (SYNC output) and radiation-induced target current pulses (ITARGET output) were also recorded. For the Varian 21EX linac used in this study, the synchronization (sync) signal occurs with a fixed frequency (320 Hz), regardless of whether the radiation beam is on or not. The accelerator radiation (gun) pulses coincide with the synchronization pulses, but their frequency depends on the given repetition rate (100-600 monitor units (MUs) per minute). The PMT voltages are recorded using a National Instruments NI6218 data acquisition card and customized LabVIEW software. To optimize data acquisition, the system was designed to record voltages in a non-continuous manner. Specifically, we sampled the PMT voltages only during the 400 ms following each sync pulse (20 samples per sync at 50 kHz). By synchronizing our data sampling with the signal from the SYNC output, we only acquire data shortly after each synchronization pulse. This provides us with the same dose information while recording less data.

8.3 Results and discussion

The detector system was calibrated at 100 cm source-to-surface distance (SSD) and 1.5 cm depth in solid water. Field sizes between 3 x 3 cm^2 and 20 x 20 cm^2 were used to irradiate different lengths of straight fiber, with and without the scintillator in the beam isocenter, hereby minimizing and maximizing the stem effect at known delivered dose. To assess the ability of the system to measure the dose per pulse, an irradiation of 100 MUs at a repetition frequency of 600 MU/min and a 10 x 10 cm^2 field size was used. For this irradiation, the expected dose per pulse was calculated by dividing the total delivered dose with the number of counted target current pulses. The uncertainty on the number of delivered pulses was estimated through 10 identical irradiations. The measured dose per pulse was found by summing the dose over all samples for each pulse in the plateau region, and then obtaining the mean and standard deviation for all pulses. The measured and expected dose per pulse estimates are compared in table 8.1. The dose measurements are seen to be in general good accordance with expectations, with a dose per pulse of approximately 0.3 mGy for a 1 Gy irradiation delivered in 10 s. As each pulse is delivered in 5 ms, this corresponds to an actual dose rate of 60 Gy/s within each pulse, regardless of repetition frequency. The large uncertainties on dose estimates (respectively 3 and 6% standard deviation) are with great certainty due to intrinsic variation of the voltage measurements. The light yields of the two probes are comparable. The difference in precision between the two probes is a result of lower cathode luminous sensitivity of the PMTs used for detection of light from probe 2. Figure 8.1 shows the measured dose per pulse for the two scintillator probes, at the beginning of a 100 MU irradiation. A transient in the dose delivery is clearly evident, with the dose per pulse slowly reaching the expected con-

Table 8.1: Dose estimates.

	Expected	Probe 1	Probe 2
Mean dose/pulse[mGy]	0.285	0.286	0.287
% Standard Deviation	0.120	2.843	5.806
% Dev. from expected	–	0.128	0.492
Total dose [mGy]	1000	1001	1005

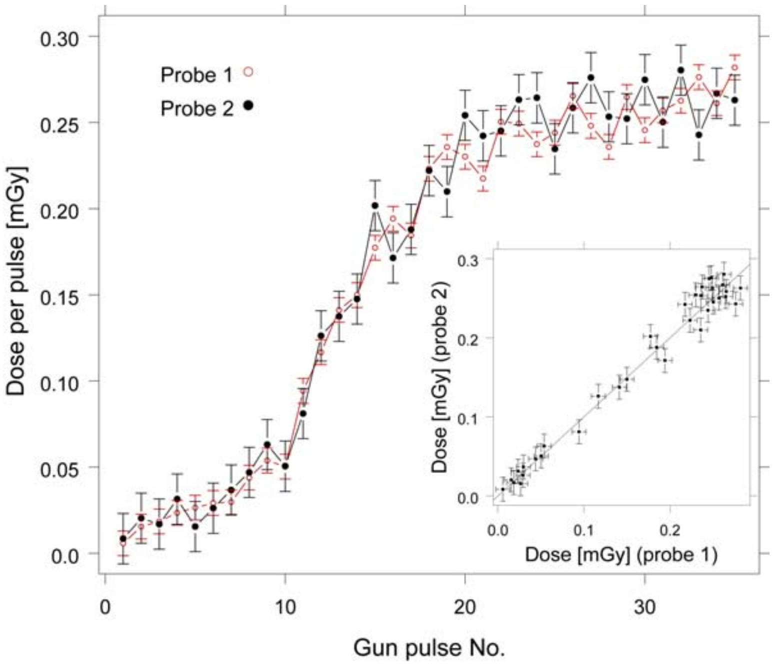

Figure 8.2: Dose delivery transient for the first 35 gun pulses of a 100 MU irradiation. Error bars indicate the predicted uncertainty on the dose per pulse estimate (1 SD). Insert: Correlation between scintillator probe 1 and probe 2.

stant value. The insert shows that apart from the large uncertainties on the dose per pulse estimates, the estimates from the two fiber probes are highly correlated in the transient region. The dose delivery transient can be observed as a variation in the dose rate displayed on the treatment console at beam start-up, indicating that the observed transient is indeed caused by the linac and not the detector system. The transient behavior of medical linacs has also been seen in measurements using fiber-coupled Al_2O_3:C probes (Aznar et al., 2004).

8.4 Conclusion

As radiotherapy treatment procedures such as arc therapy and gated radiotherapy are getting more common, a need for time-resolved dosimetry methods arises to verify the dose delivery of a medical linac on a pulse timescale. This study shows that the scintillator-based detector system is able to resolve the dose per pulse delivered by a medical linac. For such fast dose measurements, it is favorable to use synchronized data sampling compared to uniform sampling, since the amount of data is drastically reduced while providing the same information. While the organic scintillators lack the great accuracy of the Delta 4 system, they exhibit water equivalence and small size, enabling them to be used in vivo or in anthropomorphic phantoms. The uncertainties of dose per pulse measurements ($3-6\%$ standard deviation) could be minimized by optimizing the detector system electronics, in order to suppress intrinsic fluctuations of the dosimeter voltage signals. However, the current accuracy of the system is more than sufficient for qualitative observations of accelerator-specific dose delivery transients. When taking the mean dose estimate for all pulses of a 1 Gy irradiation, the measured dose per pulse values for the two scintillator probes were seen to agree with the theoretical value of approximately 0.3 mGy with a deviation less than 1%, well within the measurement uncertainties.

Chapter 9

Paper II: Characterizing a pulse-resolved dosimetry system for complex radiotherapy beams using organic scintillators

A. R. Beierholm, R. O. Ottosson, L. R. Lindvold, C. F. Behrens and C. E. Andersen

Abstract

A fast-readout dosimetry system based on fibre-coupled organic scintillators has been developed for the purpose of conducting point measurements of absorbed dose in radiotherapy beams involving high spatial and temporal dose gradients. The system measures the dose for each linac radiation pulse with millimetre spatial resolution. To demonstrate the applicability of the system in complex radiotherapy fields, output factors and per cent depth dose measurements were performed in solid water for a 6 MV photon beam and compared with Monte Carlo simulated doses for square fields down to 0.6 cm x 0.6 cm size. No significant differences between measurements and simulations were observed. The temporal resolution of the system was demonstrated by measuring dose per pulse, beam start-up transients and the quality factor for 6 MV. The precision of dose per pulse measurements was within 2.7 % (1 SD) for a 10 cm x 10 cm field at 10 cm depth. The dose per pulse behaviour compared well with linac target current measurements and accumulated dose measurements, and the system was able to resolve transient dose delivery differences between two Varian linac builds. The system

therefore shows promise for reference dosimetry and quality assurance of complex radiotherapy treatments.

9.1 Introduction

The use of organic scintillators for dosimetry in complex radiotherapy fields, such as the ones used in stereotactic radiotherapy or intensity-modulated radiotherapy (IMRT), has been studied extensively (Létourneau et al., 1999; Beddar et al., 2001; Lambert et al., 2010; Klein et al., 2010). However, no experimental studies have so far verified the use of organic scintillators by direct comparison with Monte Carlo (MC) simulations of beam output in small fields, nor taken advantage of the fast response of commercial organic scintillators to measure doses delivered in radiotherapy beams on the actual timescale of the pulsed linac output. Dose measurements in small fields put high demands on the dosimeters used, and present a rapidly evolving field of research (IPEM, 2010). Because of the lack of reference data for small fields, the best way to verify dose measurements seems to be a comparison between different dosimetry methods and MC simulations, as demonstrated in e.g. Das et al. (2008), Cheng et al. (2007) and Scott et al. (2008).

As for the temporal structure of dose delivery, detailed knowledge of the dose deposition with time is of potential relevance for quality assurance (QA) purposes - especially for dynamic treatments like IMRT, where small dose segments on the order of a cGy are not uncommon. In general, the instantaneous dose rate within the μs duration linac radiation pulses is very high, easily reaching 50 Gy s^{-1} for normal beam delivery and well over 100 Gy s^{-1} for flattening-filter-free delivery (Vassiliev et al., 2006). Therefore, pulse-resolved dose measurements will arguably provide physical insight into modern radiotherapy beam delivery. Also, some microdosimetric and spectroscopic information about the irradiation process might be uncovered, as suggested by Illemann (2009). An array of organic scintillators using charge-coupled device (CCD) and electron multiplying charge-coupled device (EMCCD) cameras has recently been developed for radiotherapy QA (Lacroix et al., 2008), *in vivo* dosimetry (Archambault et al., 2010), and small field dosimetry (Klein et al., 2010). To accumulate a satisfactory signal-to-noise ratio, dose measurements have been performed with an integration time of approximately 5 s (for the CCD) or 150 ms (for the EMCCD). However, such data acquisition times cannot resolve the ìs duration pulsed dose delivery of a medical linac, which typically has a frequency of 300-400 Hz. Studies of the theoretical precision limits of these CCD-based systems (Lacroix et al., 2010a) reveal that integration times as low as 0.1 ms can be achieved while maintaining a precision within 2 %.

This study presents further development on the fast-readout dosimetry system introduced by Beierholm et al. (2010). The system is based on two fibre-coupled organic scintillators coupled to photomultiplier tubes (PMTs). Our approach was to focus on the basic dosimetric challenges presented by small fields and non-continuous dose delivery by making measurements with a small number of point dosimeters. Our claim is that a thorough study of the basic mechanisms of spatial and temporal dose delivery will further the knowledge of the dosimetric challenges associated with modern radiotherapy. The purpose of the work was to support that the method provides detailed and highly accurate dose measurements in modern radiotherapy applications involving small fields and dynamic dose delivery. This was achieved in a twofold process: first, we critically examined the accuracy that can be obtained with organic scintillators in small field dosimetry by comparing dose measurements with MC simulations in small static fields. Secondly, we demonstrated that new dosimetric information can be uncovered with pulse resolution. We also provided experimental determination of the uncertainties associated with pulse-resolved dose measurements.

9.2 Materials and methods

9.2.1 Organic scintillator probes

The organic scintillators employed in this study were 1 mm diameter, polystyrene-based scintillating fibres (BCF-60, Saint-Gobain Ceramics & Plastics Inc., France). This type of a plastic scintillator is well characterized and has been used for similar purposes in the studies by Fontbonne et al (2002) and Frelin et al (2005). The scintillating fibres were cut to a desired length and coupled to PMMA-based optical fibres (ESKA GH-4001P, Mitsubishi-Rayon Co., Japan) of 1 mm core diameter, 2.2 mm outer jacket diameter and approximately 10 m length, terminated by an SMA connector. Before coupling, the exposed ends of the scintillator and the optical fibre were polished using aluminium oxide polishing paper of 5, 3, 1 and 0.3 μm grain size (Thorlabs Sweden AB) and cleaned using water and pressurized air. The two components were aligned using a mechanical fixation mount and a stereo microscope, before making the coupling permanent using UV-curing, refractive index-matching glue (NOA68, Norland Products Inc., USA). Finally, a jacket of black epoxy cement (EPOTEK 320, Epoxy Technology Inc., USA) was moulded around the exposed junction to light-tighten the probe. The scintillators used for probes in this study were between 1 mm and 10 mm in length.

9.2.2 ME04 detector system

The ME04 dosimetry system (Risø DTU, Denmark) is designed as a hardware basis for the fibre-coupled organic scintillators. The ME04 hardware handles the input of two dosimeter probes. The optical fibres are long

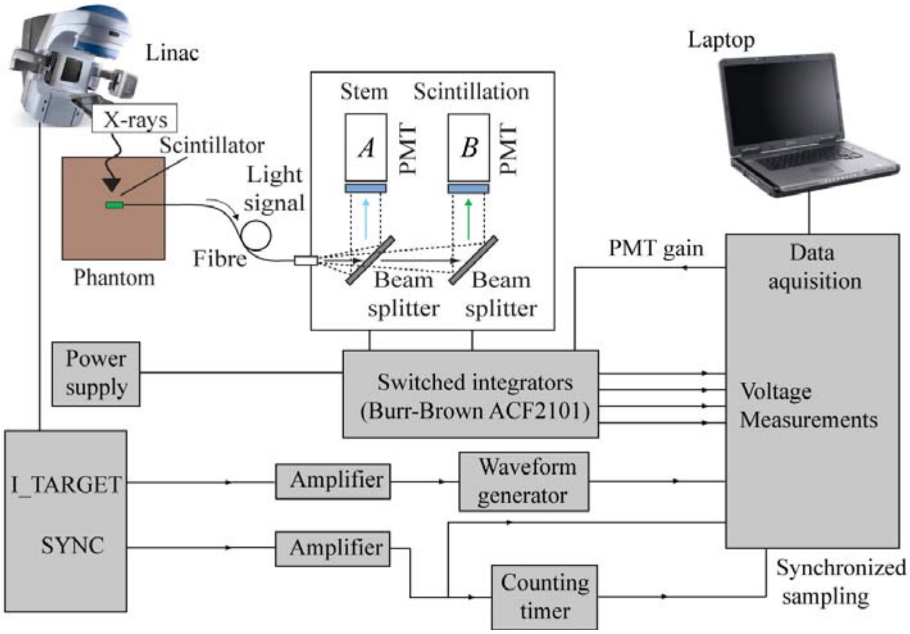

Figure 9.1: Flow chart of light detection and linac-synchronized data acquisition. For each linac SYNC pulse, the light from fibres and scintillators is chromatically discriminated and converted into voltage readings using Burr-Brown switched integrator circuits.

enough for the detection equipment to be placed outside the main treatment room. This prevents interference from stray radiation on the detector electronics. Parasitic fibre luminescence and Cerenkov radiation (the so-called stem signal) was suppressed using the chromatic removal method originally introduced by (Fontbonne et al., 2002). For each probe, light of wavelengths corresponding to mostly stem signal (designated A) and scintillation (designated B) is chromatically separated using yellow and magenta 45° dichroic mirrors (Edmund Optics Ltd, UK) and subsequently detected using two Hamamatsu H5784 PMT modules (Hamamatsu GmbH, Germany) operated in current mode at 0.3 V gain. Calibration links the absorbed dose, D, to the stem signal contribution, A, and the scintillator signal contribution, B. The data acquisition is synchronized with the pulsed synchronization output of the linac. The ME04 system makes use of a "sample-hold" setup using Burr-Brown ACF2101 switched integrator circuits (Mountford et al., 2008). The charge built up in the 100 pF capacitor is held, integrated, and read out before it is reset at the onset of the next synchronization pulse. The system handles five input channels, with four of these being used by the PMTs. The fifth is used for measuring the linac target current, which is the current required to keep the linac gun target electrically neutral when the target is hit by the accelerated electron bunches during irradiation. The temperature inside the hardware casing is measured by a thermistor to correct for the temperature-dependent sensitivity of the PMTs (approximately 0.1 % per °C). The voltage signals are acquired using a NI 6218 DAQ card and a data acquisition software interface in-house developed in LabVIEW (National Instruments Inc., USA).

9.2.3 Setup for irradiation and dose measurement

A flow chart of the measurement setup is shown in figure 9.1. Dose measurements were made using 6 MV x-rays delivered by a Varian 2300 iX medical linac at Copenhagen University Hospital, Herlev. The linac was calibrated to deliver a dose to water of 1 cGy per monitor unit (MU) for a 10 cm x 10 cm field at 100 cm source to surface distance (SSD), at the depth of maximum dose delivery (d_{max}) which is approximately 1.5 cm at this energy. The details of linac calibration can be found in Sjöström et al. (2009). The ME04 system was connected to the SYNC and I_TARGET BNC output of the linac to enable synchronized pulse counting of the synchronization signal and target current. In this way, the synchronization pulses as well as the target current pulses of the linac were recorded. The time structure of the Varian 2300 iX linac was determined using an oscilloscope as well as the ME04 system in non-synchronized (continuous) sampling mode. Using the oscilloscope, the duration of the linac gun pulse was measured to be 4 μs long and starting approximately 12.5 μs after the synchronization signal leading edge. As expected, the pulse period was seen to change with dose rate, with the pulse width being constant. Based on this, a sampling time of 80 μs was chosen. The charge integration started 6 μs after the synchronization pulse leading edge and terminated after 86 μs.

As emphasized in the studies by Chow et al. (2005) and Klein et al. (2010), the dosimetric characteristics of a small field depends on the beam-shaping geometry. In this study, the linac was operated in service mode with the multi-leaf collimators parked, and the square field size varied between 0.6 cm x 0.6 cm and 10 cm x 10 cm using the secondary collimator jaws. All irradiations were performed at 100 cm SSD with the linac gantry and collimators at 0° and 90° rotation, respectively. The probes were irradiated in a 30 cm x 30 cm x 21 cm solid water phantom (CTG-457, Gammex Ltd, UK). 2.5 mm x 2.5 mm x 300 mm grooves were drilled along the centre of some of the slabs for a tight housing of the dosimeter probes.

A critical point of small field measurements is to ensure correct alignment of the dosimeter with the beam isocentre. In the case of scanning water tanks, this can be achieved by scanning the dosimeter through the tank until the signal is at a maximum in the lateral and longitudinal directions. This cannot be done in a solid water phantom, where the position of the dosimeter is fixed. In the present case, we used a lead piece of the same dimensions as the scintillator. The lead piece was aligned with the apparent beam isocentre using the positioning lasers and alignment light field. A portal image was then obtained using the linac on-board imaging device, confirming the actual position of the beam isocentre. In case of an offset, the solid water phantom was carefully repositioned to correct for the offset and another portal image was obtained to verify correct positioning of the dosimeter probe. For most irradiations, 25 MU were delivered at a dose rate of 300 MU min^{-1}. The only exceptions were irradiations performed at different dose rates, made to investigate the dose per pulse dependence on dose rate. Dosimeter calibration was carried out for each scintillator probe using the same 10 cm x 10 cm field size, but for two distinct measurement configurations: (i) an irradiation with the scintillator positioned in the field isocentre; (ii) an irradiation with the fibre going straight through the beam and the scintillator positioned approximately 20 cm outside the beam and phantom. The shift in fibre position is minimized to ensure that the optical spectra of the two channels are not changed significantly, since the chromatic removal method depends on a constant stem signal spectrum (Frelin et al., 2005; Beierholm et al., 2008). The dosimeter probes were calibrated at 10 cm depth, to follow the standards of the TRS-398 protocol (IAEA, 2000). A water-to-solid water depth correction factor of 1.011 was applied to account for differences in electron density (Seuntjens et al., 2005). Three consecutive measurements were used for each of the two calibration configurations.

To demonstrate the spatial resolution of our dosimeter probes in the context of small radiation fields, we used a probe of 1 mm scintillator length to measure output factors (OFs) for collimator settings from 10 cm x 10 cm down to 0.6 cm x 0.6 cm, as well as per cent depth dose (PDD) for the largest and smallest field. The OF for a given field is a measure of the dose absorbed at the field isocentre per delivered MU, relative to a reference field which is typically 10 cm x 10 cm. The OFs are normally defined at d_{max}, but to avoid electron contamination, it is common practice to perform the measurements at a larger depth, and then extrapolate to d_{max} using PDD reference measurements (Dutreix et al., 1997). However, this cannot be done for small fields, as reference measurements are normally not available for fields smaller than 3 cm x 3 cm. In this study, the hospital reference depth was 10 cm, and therefore we conducted our OF measurements at that depth. PDD measurements were performed by moving the dosimeter slab down the stack for each measurement depth. A portal image was taken at each depth using the lead piece to improve the dosimeter-isocentre alignment. The normalization depth was 1.5 cm (d_{max}). An additional 9 cm solid water stack was added to the phantom to ensure satisfactory backscatter conditions for measurements at 20 cm depth. To assess the degree of dose underestimation due to volume averaging, dose was measured for the 0.6 cm x 0.6 cm field at d_{max} as a function of scintillator size, for scintillators of 1 mm to 10 mm length.

9.2.4 Additional dosimetry methods

Independent dose measurements using LiF thermoluminescence dosimeters (TLDs) were made for the out-of-field calibration configuration, to measure the out-of-field dose to the scintillator. The TLDs were subsequently read out using a Dosacus TLD-reader (Alnor Oy, Finland) at the Radiation Research Division, Risø DTU. Reference OF measurements, performed in a water tank using a waterproof standard ionization chamber (IC) of the Farmer 30006/30013 type (PTW Freiburg GmbH, Germany) were included in the OF study for verification of the MC model. These reference measurements were originally presented by Sjöström et al. (2009). Because of large cavity volume (0.6 cm^3), the IC was however not used for fields smaller than 3 cm x 3 cm. For the volume averaging experiment, lateral profiles of the 0.6 cm x 0.6 cm field were measured at d_{max} using GAFchromic EBT2 film (Radiation Products Design Inc., USA), which was calibrated in the 1-5 Gy dose range and read out using a Canon LiDE 90 scanner and RisøScan (Helt-Hansen and Miller, 2004).

9.2.5 Monte Carlo simulations

The OF measurements were compared with MC simulations of (i) a 1.0 mm x 1.0 mm x 1.0 mm polystyrene scintillator in a 30 cm x 30 cm x 21 cm solid water volume and (ii) a 1.0 mm x 1.0 mm x 1.0 mm water voxel in a homogenous 30 cm x 30 cm x 21 cm water volume. For the volume averaging experiment, dose was calculated for 1-10 mm long scintillators in a 0.6 cm x 0.6 cm field at d_{max}. For MC calculations of PDD, an additional 9 cm of solid water was included to allow for sufficient backscatter conditions. The linac was modelled (Ottosson et al., 2010) using the BEAMnrc user code (Rogers et al., 1995, 2009), and the MC model was commissioned for field sizes between 3 cm x 3 cm and 30 cm x 30 cm. Dose to scintillator/water was scored using DOSXYZnrc (Walters et al., 2009) with a precision of approximately 0.5 % for 10 cm x 10 cm at 10 cm depth. Collimator jaw positioning uncertainty was not evaluated, and the cladding and jacket of the scintillator probe were not included in the MC simulations. The MC data included corrections for collimator backscatter in the linac monitor chambers, in accordance with the method described by (Lam et al., 1998).

9.3 Results and discussion

9.3.1 Measurement precision

Because the number of scintillation photons detected by the ME04 system is linearly related to the dose absorbed in the scintillator, measurement precision depends on the accumulated dose. The precision of pulse-resolved dose measurements was defined as the relative standard deviation of the dose per pulse (DPP). Although a 25 MU irradiation typically consists of approximately 900 radiation pulses, we used a subset consisting of the last 500 pulses to establish a plateau value where accelerator dose rate fluctuations were minimized. In this way, the precision of individual DPP measurements was found to be 2.7 % (1 SD) at 10 cm depth (approximately 0.182 mGy per pulse), using the smallest scintillator (1 mm length). The reproducibility obtained from consecutive irradiations was found to be within 0.4 % (1 SD) for a 16.6 cGy accumulated dose. It should be emphasized that linac-inherent DPP fluctuations always contribute to the uncertainty of dose estimates. Measuring the target current within the 500 pulse interval revealed fluctuations of approximately 1.5 % (1 SD).

The feasibility of dose-per-pulse measurements in medical dosimetry requires sufficient signal per pulse to provide high sensitivity and dosimetric precision. The DPP precision depends on the overall system throughput and therefore on the size of both detected signal contributions (A and B). Parameters such as the PMT cathode luminous sensitivity, the attenuation through the optical fibre, the scintillator size and the fibre-scintillator coupling efficiency all affect the system throughput and must all be optimized to enhance the system sensitivity and DPP precision. Depending on the scintillator length, fibre length, coupling efficiency, field size and irradiation depth, the uncertainty of DPP measurements presented in this study varied between 0.9 % and 4.1 % (1 SD). A clear correlation between the magnitude of the detected signal and the relative standard deviation was evident from measurements for arbitrary depths, field sizes and probes of different scintillator sizes, emphasizing the importance of optimizing the light collection efficiency through the entire dosimetry system. While the first version of the ME04 system sampled the decay of an RC circuit at 50 kHz sampling rate with several samples per pulse (Beierholm et al., 2010), the new switched-integrator method has reduced timing errors and intrinsic voltage fluctuations of the hardware. This development has improved the measurement precision of the system by approximately a factor 2. In addition, since each synchronization pulse is only sampled once, the amount of data is reduced while maintaining the same pulse-inherent information.

9.3.2 Stem signal removal accuracy and calibration stability

When using fibre-coupled organic scintillators, the largest source of systematic measurement errors is the parasitic stem signal originating from the optical fibre itself. Therefore, the accuracy of such a dosimetry system is critically dependent on the ability to suppress the stem signal. If correctly calibrated, the signal contribution from the optical fibre should be completely suppressed and the dose measurements should be independent of the orientation of the optical fibre, the length of irradiated fibre, or the irradiation depth. Lambert et al. (2009) suggested a dependence of the stem signal

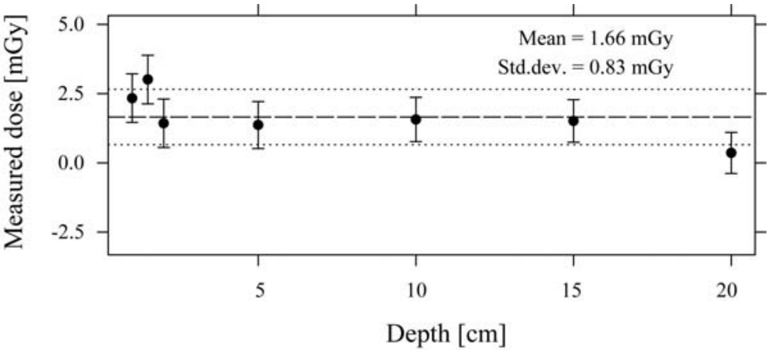

Figure 9.2: Measured dose versus depth for a maximal stem signal configuration of a 25 MU irradiation. Assessment of the success of stem signal removal. Only the fibre is in the beam; for an ideal dosimeter, the dose measured would be equal to the out-of-field dose at the point of measurement. Error bars (1 SD) correspond to the accumulated dose uncertainty.

spectrum on the incident energy spectrum in a water phantom, and recommended that any stem signal removal procedure that relied on the constancy of the stem signal spectrum be tested as a function of depth. This test was performed and the results are shown in figure 9.2, where estimated dose to the scintillator is plotted against depth. The scintillator was in this case outside the main radiation field with the fibre going straight through the field. Therefore, the dose absorbed in the scintillator should be independent of the position of the fibre in the phantom. No significant deviation from the mean value was seen with depth, and the standard deviation of 0.8 mGy was comparable to the overall 0.6 mGy measurement reproducibility.
The dose to the TLDs out-of-field was measured to be 1.3 ± 0.4 mGy for a 10 cm x 10 cm field. The uncertainty on the out-of-field dose during calibration hereby induces a 0.4 mGy systematic uncertainty on dose estimates. This is not significant compared with measurement reproducibility, although measurements of doses out-of-field would be more severely affected than in-

Table 9.1: Uncertainty budget for pulse-resolved and accumulated dose measurements. All uncertainties are given as 1 SD.

Depth (cm)	Measurement	Delivered dose (mGy)	Reproducibility (%)	Calibration (%)	PMT (%)	Total uncert. (%)	Total uncert. (mGy)
1.5	Per pulse	0.277	2.13	0.17	0.10	2.14	0.006
1.5	Accum.	250.0	0.28	0.17	0.10	0.34	0.850
10.0	Per pulse	0.182	2.72	0.26	0.10	2.73	0.005
10.0	Accum.	166.0	0.40	0.26	0.10	0.49	0.807

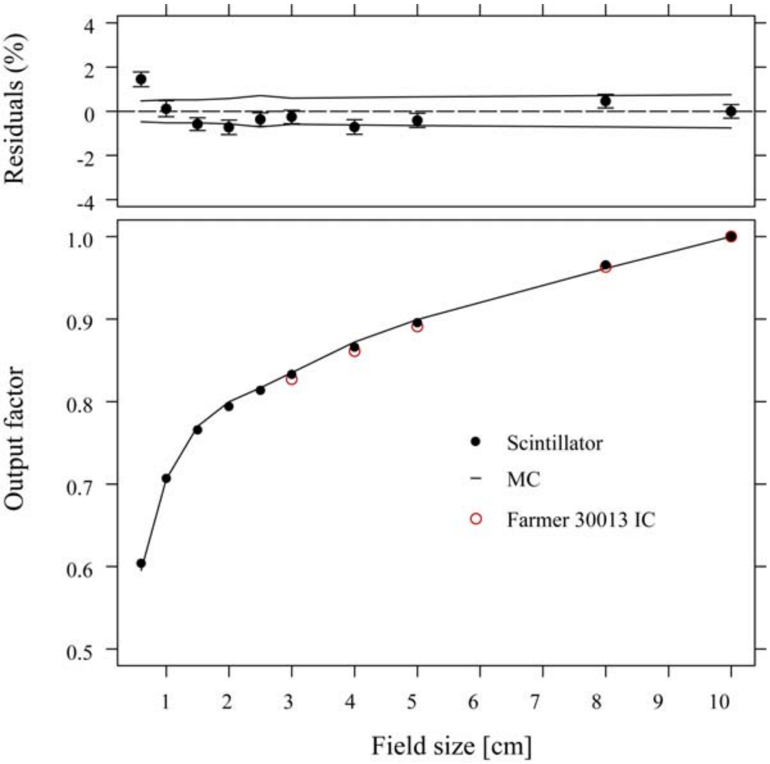

Figure 9.3: OF measurements for field sizes of 10 cm x 10 cm down to 0.6 cm x 0.6 cm at 10 cm depth. Filled circles: organic scintillator probes in solid water. Solid line: MC calculated dose to the scintillator in solid water. Hollow circles: reference IC measurements in water. Solid lines in residual plot represent uncertainties on MC simulations. Error bars (1 SD) correspond to the accumulated dose uncertainty.

field measurements. This error is circumvented if applying the calibration configuration described in Lacroix et al. (2008) and Beierholm et al. (2010), which however requires irradiations at known doses at small and large field sizes.

Measurement reproducibility, calibration uncertainty and PMT temperature correction uncertainty all contribute to the overall measurement uncertainty of the ME04 system. An uncertainty budget, giving approximate values of the combined uncertainties of pulse-resolved as well as accumulated dose measurements, is presented in table 9.1 for a 1 mm length scintillator in a 10 cm x 10 cm field, at 1.5 and 10 cm depths.

9.3.3 Small static field measurements

OF measurements for 10 cm x 10 cm down to 0.6 cm x 0.6 cm fields at 10 cm depth are presented in figure 9.3, where they are compared with MC

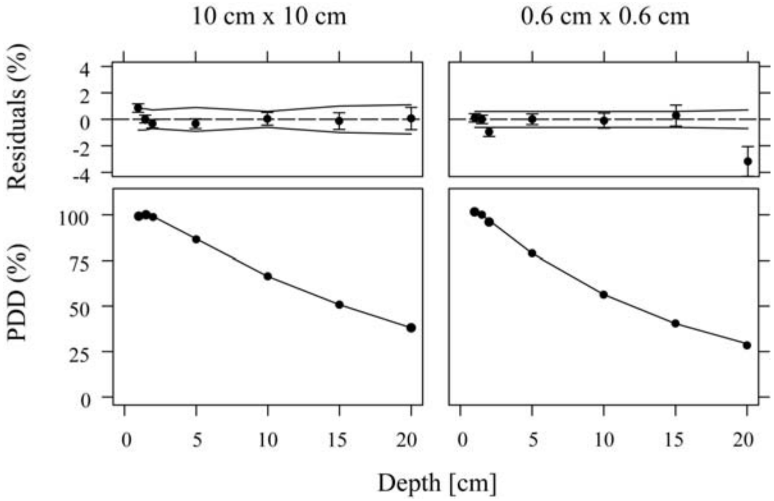

Figure 9.4: PDD measurements for an organic scintillator probe in solid water for 10 cm x 10 cm field size (left), and for 0.6 cm x 0.6 cm field size (right). Solid line: MC simulated dose to the scintillator in solid water. Solid lines in residual plot represent uncertainties on MC simulations. Error bars (1 SD) correspond to the accumulated dose uncertainty.

simulations of a scintillator in solid water as well as to IC measurements in water. The scintillator measurements agreed with MC calculations with a maximum deviation of 1.5 %. Considering the IC measurements, the scintillator measurements agreed to within 0.7 %, while the MC simulations differed from the IC measurements by maximum 1.3 %. An agreement within 1.4 % was observed between measurements and MC calculated dose to water (plot not shown). It should be noted that the scintillator OF measurements also compared well with the ones recently presented by Klein et al. (2010). PDD measurements for the 10 cm x 10 cm and 0.6 cm x 0.6 cm fields are presented in figure 9.4, for depths of 1 cm down to 20 cm. For both field sizes, measured dose to the scintillator is compared with MC calculated dose. For the 10 cm x 10 cm field, measurements agreed with MC simulations to within 0.9 %. For the 0.6 cm x 0.6 cm field, most measurements were within 0.9 % agreement with MC while the measurement at 20 cm depth displayed a 3.2 % lower PDD value compared with MC. Similarly, the measurements agreed within 1.8 % with MC-simulated PDD for water, except for the measurement at 20 cm depth which was 5.0 % too low compared with MC (plot not shown). The discrepancy at 20 cm depth was likely caused by erroneous probe-isocentre alignment, as a probe in solid water is hard to align with the field isocentre compared with a probe in a water tank for small fields, especially at large depths. Measurements using radiochromic film as well as MC simulations suggested that a misalignment between the scintillator and the beam isocentre of 1 mm in either direction leads to a dose underestimation of approximately 6 %.

The volume averaging effect was examined by using scintillators of 1-10 mm lengths to measure isocentre dose as a function of dosimeter size in a 0.6 cm x 0.6 cm field at d_{max}. The measurements were compared with MC calculations and radiochromic film measurements, and are shown in figure 9.5. The insert of figure 9.5 shows the lateral dose profile of the field, measured with radiochromic film. For a 1 mm long scintillator, the dose estimate is averaged over a 1 mm interval around the central axis of the field profile; for a longer scintillator, the dose is averaged over a larger area and the peak dose is underestimated accordingly. The use of scintillators longer than 2 mm was found to induce a dose underestimation of 2 % or higher. The use of dosimeters this large is therefore strongly discouraged in small field dosimetry, since the enhancement in signal magnitude and precision comes at the expense of systematic measurement errors due to volume averaging. Large discrepancies between the scintillator, MC and film are evident when the dosimeter is comparable to or much larger than the size of the field. For lengths shorter than 5 mm, the OF estimates obtained with the scintillator, film and MC agree within 2.1 %.

9.3.4 Pulse-resolved measurements

Figures 9.6(a) and (b) show an example of DPP measurements for the first 20 gun pulses of beam delivery, performed using two probes at 10 cm and 20 cm depth. Part (a) shows the response of the probe at 10 cm depth for the first 20 gun pulses of beam delivery. For each synchronization pulse, the response of the scintillator is compared with the measured target current, which has been normalized to the same scale as the measured mean DPP. Every second measurement yields zero DPP because the pulse repetition frequency (dose rate) is half of the maximum value, meaning that there is no gun pulse for every second synchronization pulse. The transient behaviour is evident and comparable for both the scintillator and target current measurements. Part (b) shows the measured quality factor of the radiation beam, represented by the $TPR_{20,10}$ value, obtained from the DPP simultaneously measured using the probe at 10 cm depth and the one at 20 cm depth. The $TPR_{20,10}$ value is seen to fluctuate with a 5.8 % standard deviation around a constant value of 0.667 for the first 20 pulses. For the total number of pulses a mean value of 0.666 ± 0.001 was obtained, being comparable to the expected value of 0.669 measured using a Farmer chamber (Sjöström et al., 2009). This shows that the radiation quality of the beam can be considered constant on the per-pulse level, for the whole irradiation as well as in the transient. The transient behaviour is characteristic to the individual Varian 2300 iX linac used in this study, and is distinctively different from previous experiments performed on an older linac model (Varian 21 EX), as depicted

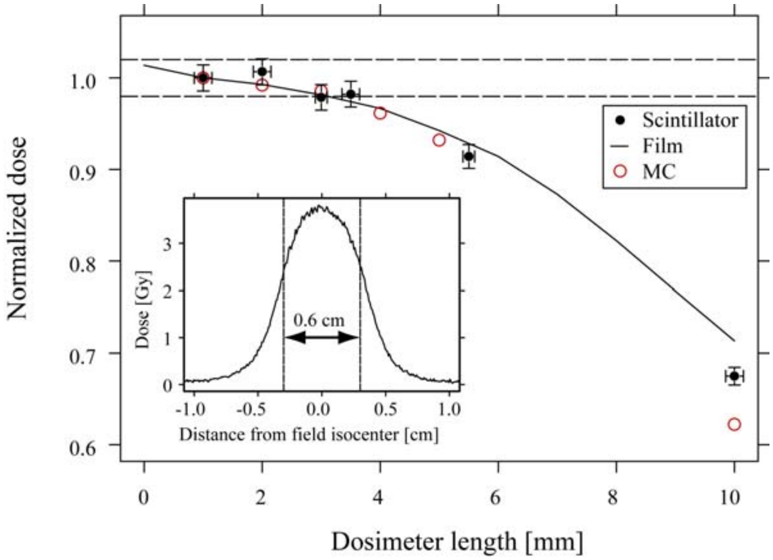

Figure 9.5: Estimated isocentre dose in a 0.6 cm x 0.6 cm field at d_{max} as a function of dosimeter size. Data are normalized to values corresponding to 1 mm length. Solid circles: dose measured with organic scintillator probes in solidwater. The x and y error bars are the uncertainty estimates of the scintillator length and probe-isocentre alignment, respectively. Hollow circles: MC calculated dose for a scintillator in solid water. Error bars are smaller than the symbols. Solid line: dose measured with radiochromic film. The dashed lines indicate the ± 2 % deviation from the normalization point. Insert: lateral dose profile of the 0.6 cm x 0.6 cm field, measured with radiochromic film subjected d to a 500 MU irradiation at d_{max}.

in figure 9.6, part (c).
The figure shows the start-up transient (normalized DPP) for five irradiations using the 2300 iX compared with an irradiation using the 21 EX, all at 300 MU min^{-1} dose rate. The data for the 21 EX were part of the study presented in Beierholm et al (2010). While the 21 EX apparently reaches stable dose per pulse after 20-30 pulses, the 2300 iX reaches a stable level after merely 5-10 pulses. These measurements show a clear dosimetric difference between the linacs concerning dose rate stability, potentially influencing the accuracy of linac dose delivery for small dose segments (on the order of 1 cGy). According to Konnoff et al. (2011), there appears to be general consensus in the literature on the under-delivering of dose for small dose segments, regardless of linac build. However, figure 9.6 indicates that the degree of under-dosing is linac specific. An interesting application of the new dosimetry system would be to compare the precision of dose delivery on a pulse scale for a representative assortment of linac builds used in hospitals, not only for static beam delivery but also for small IMRT plan segments.

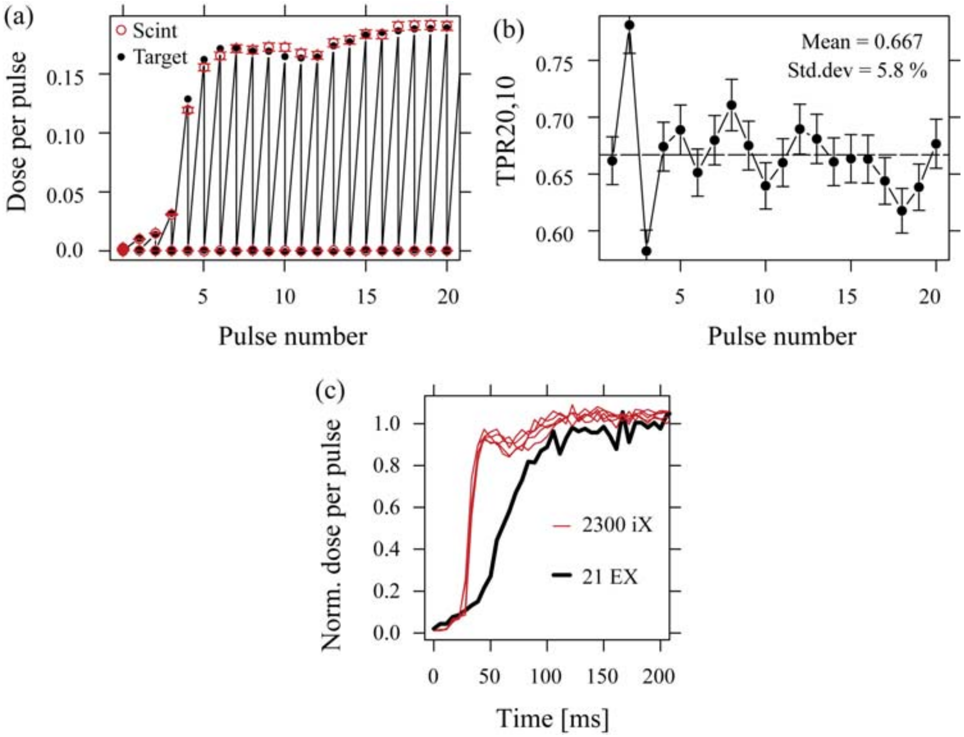

Figure 9.6: Transient behaviour for dose delivery at 300 MU min^{-1} dose rate. (a) DPP measured at 10 cm depth (hollow circles), with the linac target current (filled circles and lines) normalized to the mean DPP of the irradiation. (b) Measured TPR$_{20,10}$ per pulse, obtained using two scintillator probes positioned at 10 and 20 cm depth. Error bars (1 SD) correspond to the uncertainty on DPP and TPR$_{20,10}$ per pulse, respectively. (c) Transient behaviour for the Varian 2300 iX (thin lines) and a Varian 21 EX (thick line).

Table 9.2 shows examples of beam characteristics for various dose-per-pulse values (i.e. field sizes and depths) and pulse repetition frequencies (i.e. dose rates). The transient pulses at the start of irradiation were defined as the pulses exhibiting a dose value being lower than the mean plateau value by more than two standard deviations. For each irradiation, the expected DPP was calculated from the MC simulations of the scintillator in solid water and the total number of pulses. A small change in the total number of pulses was seen with dose rate. The DPP values for different field sizes and depths were comparable to the PDD values presented in section 9.3.3, confirming the correlation between pulse-resolved dose and accumulated dose.

9.4 Conclusion

We present a dosimetry system based on fibre-coupled organic scintillators to be used for dose measurements in dynamic and stereotactic radiotherapy. Due to 0.1 ms readout time, the system can measure the dose delivered for each individual linac radiation pulse, enabling detailed time-resolved QA of small dynamic radiotherapy dose increments. The presented system configuration measures the absorbed dose with an uncertainty within 2.7 % per pulse and within 0.5 % for the accumulated dose (1 SD) at 10 cm x 10 cm field size and 10 cm depth. No significant discrepancies were found between measurements and MC simulations for field sizes down to 0.6 cm x 0.6 cm. The significance of the pulse-resolution capability of the system can be further explored by comparing the fluctuations in dose rate during irradiations for different linacs and beam energies, and ultimately by performing pulse-resolved QA of gated 4D radiotherapy and IMRT segments. This study therefore shows that the system presents a suitable and promising choice for reference dosimetry and quality assurance in advanced radiotherapy.

Acknowledgements

This work was supported by the Danish Cancer Society and CIRRO - Center for Interventional Research in Radiation Oncology, supported by the Lundbeck Foundation. The hardware used for the MC calculations was donated by the Toyota Foundation, Denmark.

Table 9.2: Transient behaviour, number of pulses, DPP precision (1 SD), and the difference between measured and excepted DPP for irradiations at different field sizes, depths and dose rates.

Field side (cm)	Depth (cm)	Dose rate (MU/min)	Total dose (Gy)	Total no of pulses	Trans. no of pulses	DPP prec. (%)	Meas. DPP (mGy)	Exp. DPP (mGy)	DPP diff. (%)
10.0	1.5	100	0.250	896	16	2.2	0.2792	0.2790	0.1
10.0	1.5	200	0.250	899	18	2.3	0.2784	0.2781	0.1
10.0	1.5	300	0.250	900	15	2.1	0.2773	0.2778	-0.2
10.0	1.5	400	0.250	903	17	2.2	0.2769	0.2769	0.0
10.0	1.5	500	0.250	903	15	2.3	0.2757	0.2769	-0.4
10.0	1.5	600	0.250	905	20	2.2	0.2760	0.2762	-0.1
10.0	10.0	300	0.166	903	14	2.7	0.1826	0.1823	-0.6
10.0	20.0	300	0.095	902	15	3.6	0.1052	0.1039	-0.3
0.6	10.0	300	0.099	902	10	3.1	0.1091	0.1096	-0.4
0.6	20.0	300	0.051	903	14	4.1	0.0551	0.0577	-3.4

Chapter 10

Paper III: Organic scintillators with long luminescent lifetimes for radiotherapy dosimetry

A. R. Beierholm, L. R. Lindvold and C. E. Andersen

Abstract

Organic scintillators with long luminescent lifetimes can theoretically be used to temporally filter out radiation-induced luminescence and Cerenkov light (the so-called stem signal) when used as fibre-coupled radiotherapy dosimeters. Since the medical linear accelerators (linacs) used for radiotherapy treatments deliver pulsed beams, the stem signal can be suppressed using dosimeter materials with luminescent lifetimes much longer than that of the stem signal. However, producing organic scintillators with long luminescent lifetimes has proven difficult in practice. We report on the results of experiments performed using two organic scintillators, one commercially available and one custom made. The luminescent lifetimes of the scintillators have been measured using i) optical excitation by pulsed UV light, and ii) irradiative excitation using high-energy X-rays from a linac. A luminescent lifetime component on the order of 20 μs was estimated for the custom-made organic scintillator, while the commercial scintillator exhibited a fast component of approximately 5 ns lifetime (7 ns as stated by the manufacturer) and an approximate 10 μs lifetime slow component. Although these lifetimes are not long enough for practical applications in radiotherapy dosimetry, this study supports that the stem signal can be greatly reduced by applying a temporal gating.

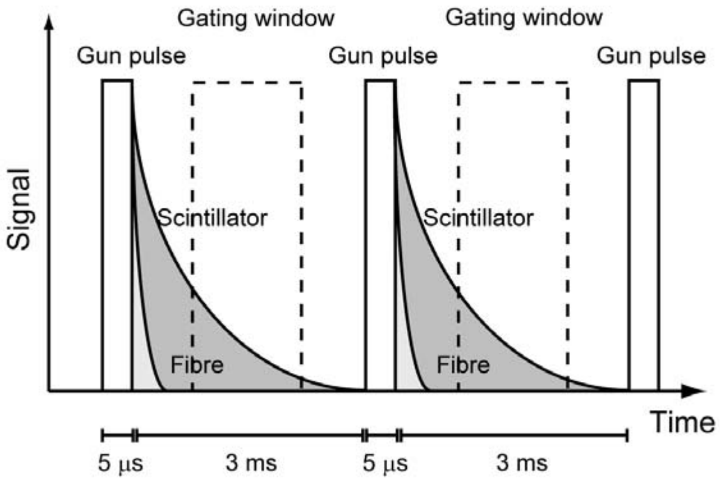

Figure 10.1: Illustration of the temporal stem signal removal method. If the decay of the scintillator signal is considerably longer than that of the stem signal, the gating will remove most of the stem signal at the expense of a reduction in the detected scintillator signal.

10.1 Introduction

For fibre-coupled optical dosimeters to be used in radiotherapy beams, the removal of parasitic fluorescence and Cerenkov radiation generated in the optical fibre (the stem signal) is imperative. Several methods have been suggested previously: the dual-fibre subtraction method (Beddar et al., 1992b), spectral filtration (de Boer et al., 1993), chromatic removal (Fontbonne et al., 2002), and temporal removal (Clift et al., 2002). The latter method can be used if the luminescent lifetime of the dosimeter material is significantly longer than the lifetime of the stem signal, which is in the picosecond to nanosecond range. For most linacs, the pulse width is a few microseconds; by applying a temporal gating mechanism, detection of light generated immediately after each pulse can be effectively excluded (see Fig. 10.1). This approach has been successfully achieved for inorganic materials (Justus et al., 2004; Marckmann et al., 2006; Tanyi et al., 2010). For organic scintillators, however, ensuring sufficiently high signal-to-noise ratios proves difficult. This is either due to a luminescent lifetime not sufficiently long, resulting in a large signal loss when applying the temporal gating, or because of low scintillator sensitivity (i.e. low light output). Clift et al. (2002) used a commercial scintillator (BC- 444G, Bicron Inc.) of 264 ns lifetime for temporal removal, but the scintillator probe lacked sufficient sensitivity to be used for standard radiotherapy beams. Thus, the challenge is to fabricate an organic scintillator with a long luminescent lifetime - preferably on the order of 1 ms - and high light output. Experiments presented recently (Lindvold et al., 2010) suggest that the creation of organic scintillators with individually customised emission spectra and luminescent lifetimes can be achieved in the laboratory, by choosing a suitable polymer matrix, primary scintillator, and organic dye (wavelength shifter). This study presents measurements performed with i) an in-house developed organic scintillator, and ii) a commercial organic scintillator.

10.2 Materials and methods

10.2.1 Fibre-coupled organic scintillators

The custom-made scintillator (designated Scintillator 73) consisted of a Trimethylol propane benzoatediacrylate photo-curable monomer base doped with a 2,5-Diphenyloxazole (PPO) primary scintillator (6.3 % wt) and a Perylene wavelength shifter. The wavelength shifter concentration was 1:250 of that of the primary scintillator. The doped monomer was moulded onto a 1 mm diameter PMMA-based optical fibre (ESKA GH-4001P, Mitsubishi-Rayon Co.). The commercial scintillator was a polystyrene-based BCF-60 (Saint-Gobain Ceramics & Plastics Inc.) coupled to an ESKA GH-4001P fibre using the method described in Beierholm et al. (2010). In both cases, the optical fibres were approximately 10 m long. Both scintillators emit visible light in a broad spectrum, with maximum emission wavelength (λ_{max}) at approximately 490 nm and 530 nm for Scintillator 73 and BCF-60, respectively.

10.2.2 Laboratory measurements

Scintillator lifetime measurements were performed using a spectrofluorimeter (FLS920, Edinburgh Instruments Ltd.). Pulsed 380 nm light from an LED (PLS370 with PDL800-D driver, Picoquant GmbH, pulsed at 40 MHz with 600 ps pulse width) was used for optical excitation. The scintillator light was detected using the build-in photomultiplier tube (PMT) of the spectrofluorimeter. The lifetime measurements on this instrument were achieved using a time correlated single photon counting (TCSPC) plug-in PC card (Model TCC900). However, lifetime measurements of the fibre stem signal could not be performed, since the 370 nm pulsed LED could not generate the stem signal.

10.2.3 Hospital measurements

Irradiation measurements were performed using either a Varian 2300iX or an Elekta SLI linac, delivering 6 or 8 MV X-rays, respectively. The fibre-coupled organic scintillators and blank fibres were irradiated in a 30 cm x 30 cm x 26 cm solid water phantom (CTG- 457, Gammex Inc.). All irradiations were carried out at a source to surface distance of 100 cm. The scintillator lifetime measurements were performed at 10 cm x 10 cm field size with the scintillators positioned at the depth of maximum dose deposition (being approximately 1.5 cm for 6 MV X-rays and 2 cm for 8 MV), while dose measurements performed with Scintillator 73 were made at various depths and field sizes. The radiation-induced light from scintillators and fibres was guided to a PMT operated in photon-counting mode (MP983, Perkin-Elmer Inc.), equipped with a 460-540 nm band pass filter. The PMT was positioned outside the main treatment room to prevent interference from stray radiation on the detector electronics. Gating of the detected signal was carried out using a TTL 7408 gate controlled by the linac SYNC/ST synchronization signal, and data acquisition was conducted using an NI 6218 DAQ card and a laptop PC equipped with a software interface in-house developed in LabVIEW (National Instruments Inc.).

10.3 Results and discussion

10.3.1 Laboratory measurements

A fast lifetime component of approximately 4.5 ns was measured for the BCF-60. By comparison, the lifetime stated by the manufacturer was 7.0 ns. A weak, long-lived luminescence component was also measured. Luminescent lifetime measurements, obtained using the Timemap function of the spectrofluorimeter, are shown on μs-scale in Fig. 10.2 for BCF-60 and in Fig. 10.3 for Scintillator 73. Each decay curve was obtained for a 1 nm wavelength bin. The luminescence lifetime seems to be caused by several independent processes: prompt fluorescence, delayed fluorescence and phosphorescence. In the 520-540 nm interval around λ_{max}, the measured 1/e lifetime was 12.6 ± 1.9 μs for BCF-60. This unexpected long-life component was probably caused by delayed fluorescence. The Scintillator 73 measurements gave a 1/e lifetime of 5.67 ± 0.02 μs at 480 nm, caused by delayed fluorescence, along with a 21.9 ± 0.7 μs lifetime at 540 nm, caused by phosphorescence.

10.3.2 Hospital measurements

A detection window 10 μs wide was applied using the TTL gate. By varying the delay between the linac synchronization pulse and the opening of the gate for each measurement, luminescence decay curves were achieved in 10

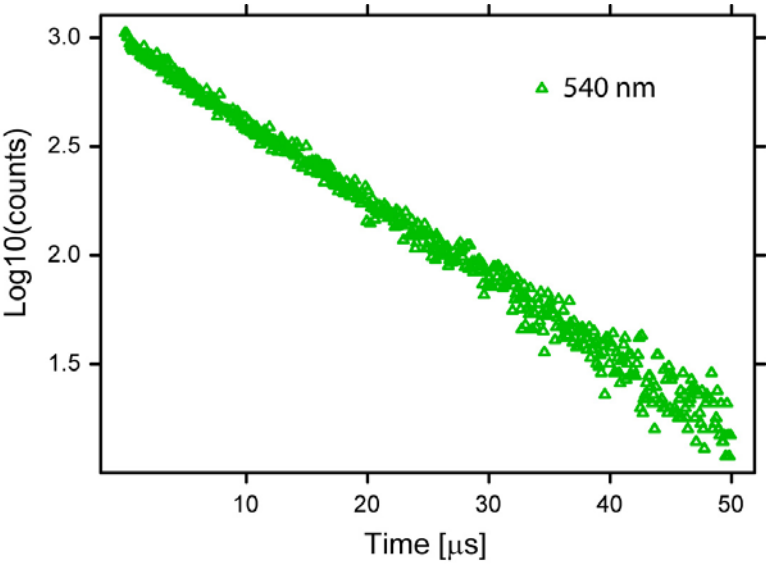

Figure 10.2: Optical excitation lifetime measurements for BCF-60 (semi-logarithmic scale). Detected signal versus time at 540 nm wavelength. The luminescence decay curve is believed to be caused by delayed fluorescence.

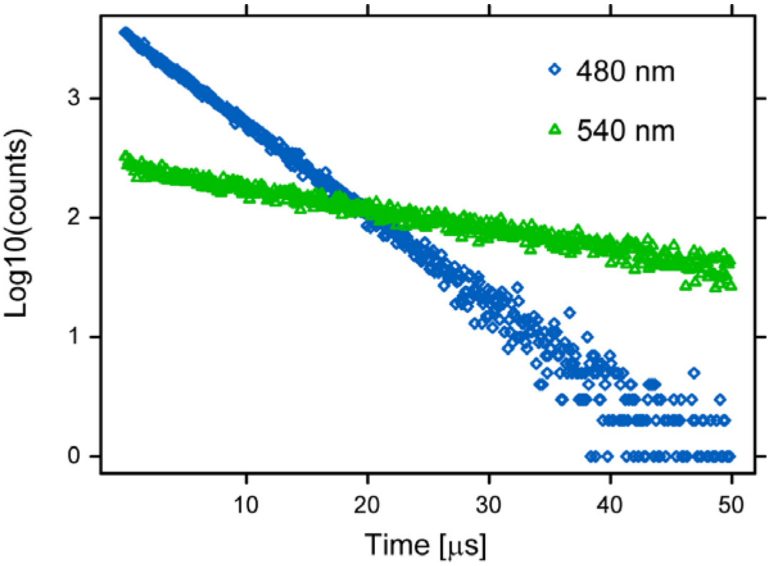

Figure 10.3: Optical excitation lifetime measurements for BCF-60 (semi-logarithmic scale). Detected signal versus time at 540 nm wavelength. The luminescence decay curve is believed to be caused by delayed fluorescence.

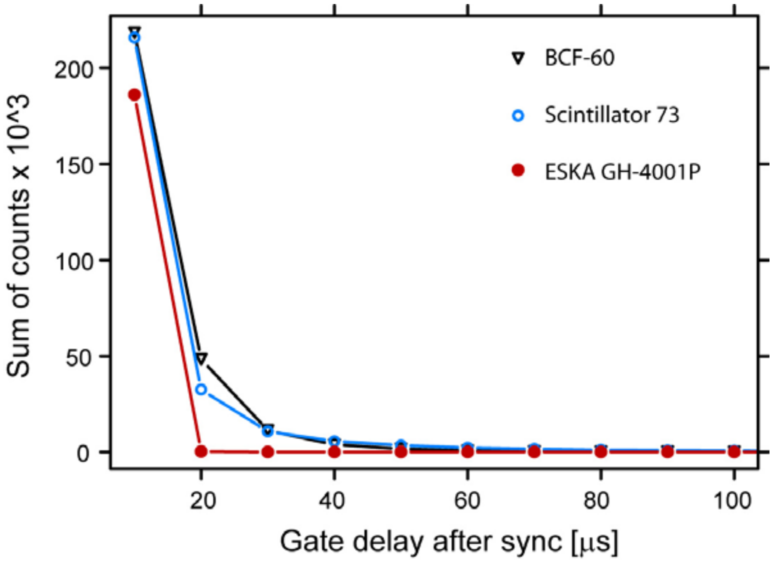

Figure 10.4: Linac irradiation lifetime measurements (absolute scale). Detected signal versus gate delay for Scintillator 73, BCF-60 and ESKA GH-4001P optical fibre. The gating window was 10 μs long for all measurements.

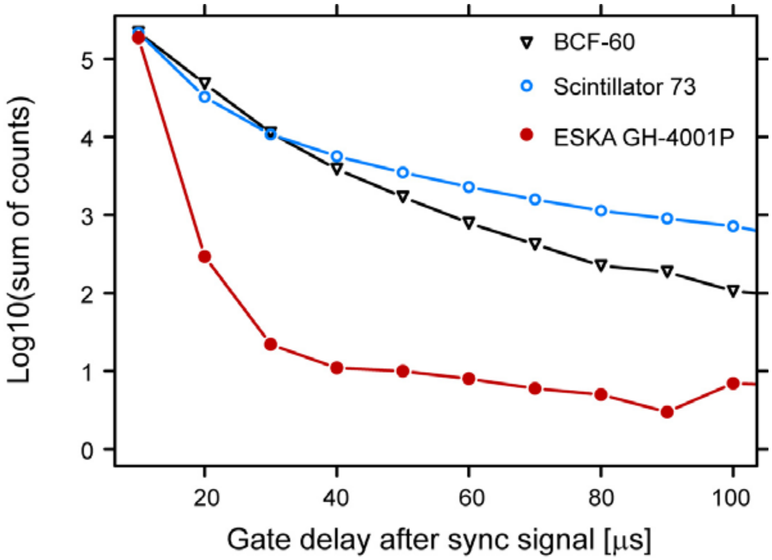

Figure 10.5: Linac irradiation lifetime measurements (semi-logarithmic scale). Detected signal versus gate delay for Scintillator 73, BCF-60 and ESKA GH-4001P optical fibre. The gating window was 10 μs long for all measurements.

μs increments for Scintillator 73, BCF- 60, and a blank ESKA GH-4001P fibre. Examples of such measurements, performed using the Varian 2300iX, are shown in Figs. 10.4 and 10.5 on absolute and semi-logarithmic scales, respectively. The 1/e luminescence lifetimes obtained were 10.3 ± 2.6 μs for BCF-60 and 20.2 ± 4.4 μs for Scintillator 73. For the GH-4001P optical fibre, a 1/e lifetime on the order of 2-5 ms was estimated. An attempt at performing actual dose measurements with Scintillator 73 was made by choosing a gating window of 60 μs and a delay of 40 μs. This yielded depth-dose measurements with precision and accuracy within 3 % compared to expected, tabulated values (BJR, 1996). However, the signal-to-noise ratio was impaired by the gating due to the insufficient lifetime of Scintillator 73. Furthermore, incomplete suppression of the stem signal was evident, yielding a 5 % dose error when the size of the field was varied between 5 cm x 5 cm and 25 cm x 25 cm.

10.4 Conclusion

This study shows that although the application of temporal stem signal removal for fibre-coupled organic scintillators seems theoretically achievable, the signal-to-noise ratio and accuracy of the dose measurements is insufficient if the scintillator luminescent lifetime is not significantly different from the stem signal lifetime as well as from the linac pulse duration. For a lifetime of 10-20 μs, a large amount of the total scintillation signal will have decayed within the 5 μs linac radiation pulse, meaning that information of true dose delivery within the pulse is lost. Furthermore, a short luminescent lifetime makes data acquisition vulnerable to timing variations, since e.g. a small jitter in the linac synchronization signal frequency moves the gating window along a steep signal decay curve, meaning that seemingly negligible timing variations intrinsic to the accelerator will result in non-negligible variations in the detected scintillator signals. The measured luminescent lifetimes were found to agree for both the BCF-60 and Scintillator 73 when excited by 370 nm light and high-energy X-rays. However, the X-ray irradiation measurements were subject to great uncertainties, and the apparent 2-5 μs lifetime of the optical fibre could not be verified by optical excitation.

Acknowledgements

The linacs used for irradiation measurements were provided by Copenhagen University Hospital Herlev. We would like to thank Claus F. Behrens, Thyge H. Sørensen and Brian Kristensen of the Division of Radiophysics, Department of Oncology, for helping us to conduct our measurements. The spectrofluorimeter used for optical excitation measurements was provided by the Solar Energy Program, Risoe DTU.

Appendix A

Optical fiber transmission spectra

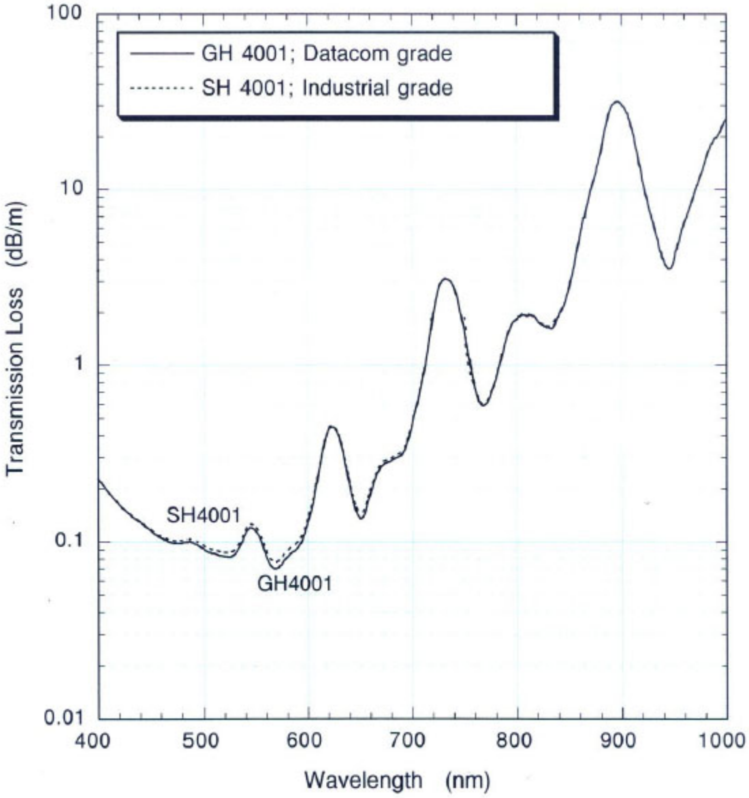

Figure A.1: Transmission loss versus wavelength for the ESKA^{TM} Premier GH4001-P PMMA-based optical fiber. Supplied by manufacturer. Source: www.fiberoptic-plastic.com

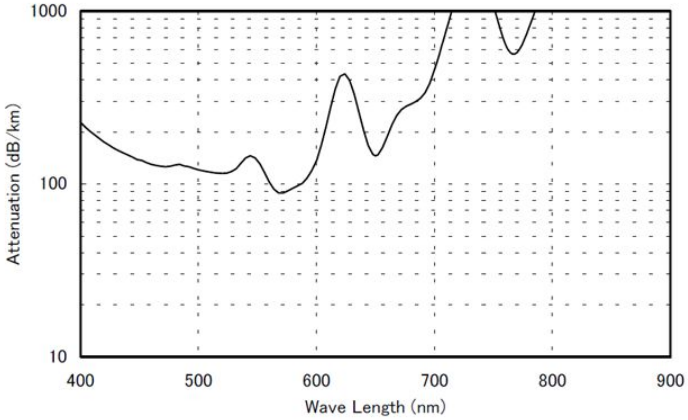

Figure A.2: Transmission loss versus wavelength for the PJS-CD1001-22E PMMA-based optical fiber. Supplied by manufacturer. Source: www.lasercomponents.com

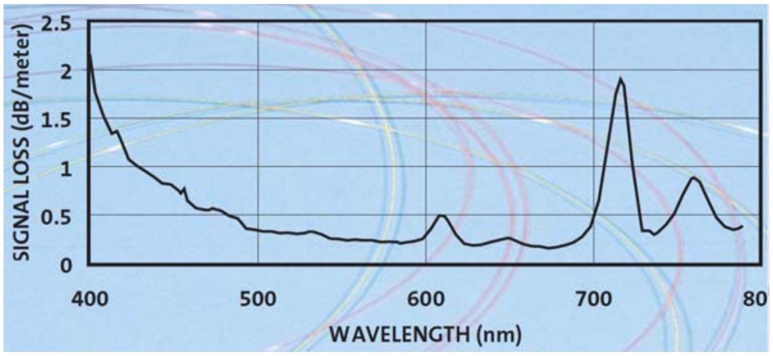

Figure A.3: Transmission loss versus wavelength for the BCF-98 polystyrene-based optical fiber. Supplied by manufacturer. Source: Saint-Gobain (2005)

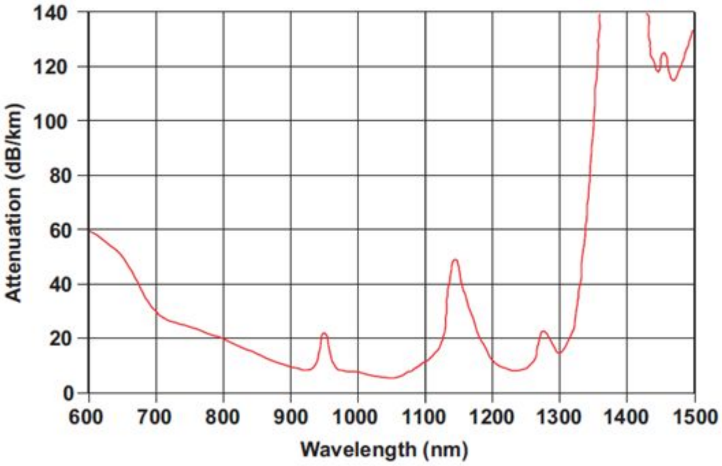

Figure A.4: Transmission loss versus wavelength for the GIPOF120-P perfluorinated graded-index polymer optical fiber. Supplied by manufacturer. Source: www.thorlabs.com

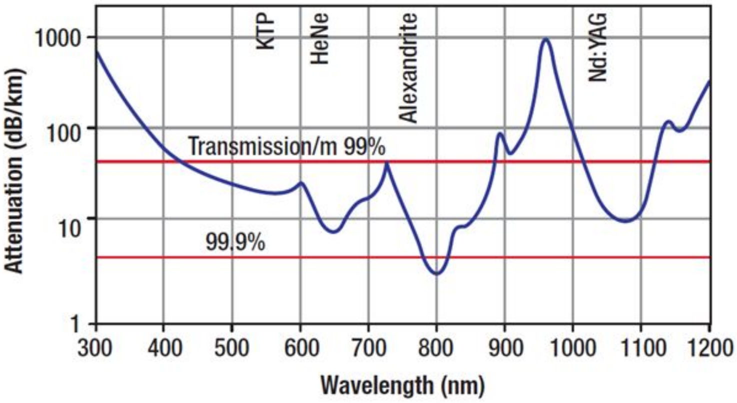

Figure A.5: Transmission loss versus wavelength for the BFH48-600 high-OH silica optical fiber. Supplied by manufacturer. Source: www.thorlabs.com

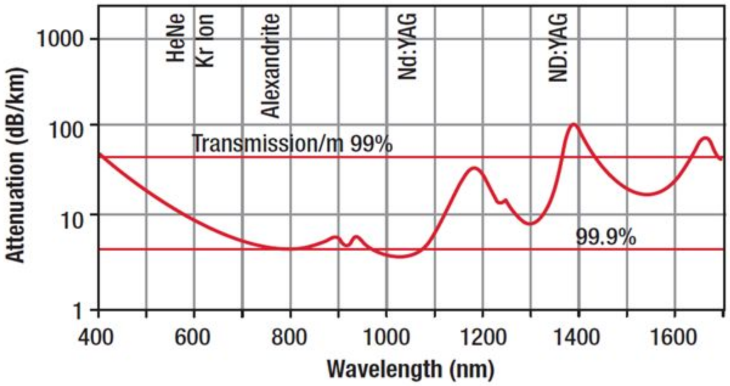

Figure A.6: Transmission loss versus wavelength for the BFL48-600 low-OH silica optical fiber. Supplied by manufacturer. Source: www.thorlabs.com

Symbols and abbreviations

β	Speed of particle v relative to speed of light in vacuum c
μ	Linear attenuation coefficient
μ/ρ	Mass attenuation coefficient
μ_{en}/ρ	Mass-energy absorption coefficient
ϕ_A	Acceptance angle
ρ	Density of absorbing medium
d_{max}	Depth of maximum dose deposition
n	Refractive index
$S(E)$	Stopping power at particle energy E
Z_{eff}	Effective atomic number
3DCRT	3-dimensional conformal radiotherapy
AKH	Allgemeines Krankenhaus (Vienna)
Al_2O_3:C	Carbon-doped aluminium oxide
aSi-EPID	Amorphous silicon electronic portal imaging device
CPE	Charged particle equilibrium
cps	Counts per second
CSDA	Continuous slowing down approach
CT	Computed tomography
CTV	Clinical target volume
DPP	Dose per pulse
EPID	Electronic portal imaging device

EPR	Electron paramagnetic spin resonance
FS	Field size
FWHM	Full width half maximum
Gy	gray
IAEA	The International Atomic Energy Agency
IC	Ionization chamber
ICRP	The International Commission on Radiation Protection
ICRU	The International Commission on Radiation Units and measurements
IMRT	Intensity modulated radiotherapy
KBr:Eu	Europium-doped potassium bromide
kV	Kilovolt/kilovoltage; the unit used to quantify the energy of e.g. diagnostic x-ray devices
LED	Light emitting diode
LiF	Lithium fluoride
Linac	Linear accelerator
MC	Monte Carlo
MeV	Megaelectron volt. The unit used to quantify the energy of radiotherapy electron beams
MLC	Multi-leaf collimator
MOSFET	Metal oxide semiconductor field-effect transistor
MU	Monitor unit
MV	Megavolt/megavoltage; the unit used to quantify the energy of radiotherapy x-ray beams
NA	Numerical aperture
NI	National Instruments Co.
NTCP	Normal tissue complication probability
OF	Output factor

OSL	Optically stimulated luminescence
OSLD	Optically stimulated luminescence dosimeter
PCF	Photonic crystal fiber
PDD	Percentage depth dose
PMMA	Polymethyl methacrylate
PMT	Photomultiplier tube
PTV	Planning target volume
QA	Quality assurance
RC	Recombination center
RL	Radioluminescence
SBRT	Stereotactic body radiotherapy
SD	Standard deviation
SiO_2:Cu	Copper-doped silica
SMA	SubMiniature version A
SRS	Stereotactic radiosurgery
SrS:Ce,Sm	Cerium- and samarium-doped strontium sulfate
SSD	Source to surface distance
TCP	Tissue control probability
TiO_2	Titanium Oxide
TL	Thermoluminescence
TLD	Thermoluminescence dosimeter
TPS	Treatment planning system
TTi	Thurlby Thandar Instruments Ltd.

Bibliography

AAPM (1999). AAPM's TG-51 protocol for clinical reference dosimetry of high-energy photon and electron beams. *Medical Physics*, 26(9):1847–1870.

Adamovics, J. and Maryanski, M. J. (2006). Characterisation of PRESAGE^{TM}: a new 3-D radiochromic solid polymer dosemeter for ionising radiation. *Radiation Protection Dosimetry*, 120(1-4):107–112.

Alfonso, R., Andreo, P., Capote, R., Huq, M. S., Kilby, W., Kjäll, P., Mackie, T. R., Palmans, H., Rosser, K., Seuntjens, J., Ullrich, W., and Vatnisky, S. (2008). A new formalism for reference dosimetry of small and nonstandard fields. *Medical Physics*, 35(11):5179–5186.

Andersen, C. E. (2011). Fiber-coupled luminescence dosimetry in therapeutic and diagnostic radiology. In *AIP Conference Proceedings*, volume 1345, pages 100–119.

Andersen, C. E., Edmund, J. M., Medin, J., Grusell, E., Jain, M., and Mattsson, S. (2007). Medical proton dosimetry using radioluminescence from aluminium oxide crystals attached to optical fiber cables. *Nuclear Instruments and Methods in Physics Research A*, 580(1):466–468.

Andersen, C. E., Marckmann, C. J., Aznar, M. C., Bøtter-Jensen, L., Kjær-Kristoffersen, F., and Medin, J. (2006). An algorithm for real-time dosimetry in intensity-modulated radiation therapy using the radioluminescence signal from Al_2O_3:C. *Radiation Protection Dosimetry*, 120(1-4):1–7.

Andersen, C. E., Nielsen, S. K., Lindegaard, J. C., and Tanderup, K. (2009). Time-resolved *in vivo* luminescence dosimetry for online error detection in pulsed dose-rate brachytherapy. *Medical Physics*, 36(11):5033–5043.

Arakia, F., Morive, N., Shimonobou, T., and Yamashita, Y. (2004). Dosimetric properties of radiophotoluminescent glass rod detector in high-energy photon beams from a linear accelerator and cyber-knife. *Medical Physics*, 31(7):1980–1986.

Archambault, L., Arsenault, J., Gingras, L., Beddar, A. S., Roy, R., and Beaulieu, L. (2005). Plastic scintillation dosimetry: Optimal selection of scintillating fibers and scintillators. *Medical Physics*, 32(7):2271–2278.

Archambault, L., Beddar, A. S., Gingras, L., Lacroix, F., Roy, R., and Beaulieu, L. (2007). Water-equivalent dosimeter array for small-field external beam radiotherapy. *Medical Physics*, 34(5):1583–1592.

Archambault, L., Beddar, A. S., Gingras, L., Roy, R., and Beaulieu, L. (2006a). Measurement accuracy and Cerenkov removal for high performance, high spatial resolution scintillation dosimetry. *Medical Physics*, 33(1):128–135.

Archambault, L., Briere, T. M., Pönisch, F., Beaulieu, L., Kuban, D. A., Lee, A., and Beddar, A. S. (2010). Toward a real-time in vivo dosimetry system using plastic scintillation detectors. *International Journal of Radiation Oncology, Biology, Physics*, 78(1):280–287.

Archambault, L., Leclerc, G., Beaulieu, L., and Lepage, M. (2006b). Absolute calibration of polymer gel dosimeters using scintillating fibers. *Journal of Physics: Conference Series*, 56:242–244.

Arnfield, M. R., Gaballa, H. E., Zwicker, R. D., Islam, Q., and Schmidt-Ullrich, R. (1996). Radiation-induced light in optical fibers and plastic scintillators: Application to brachytherapy dosimetry. *IEEE Transactions on Nuclear Science*, 43(3):2077–2084.

Attix, F. H. (1986). *Introduction to radiological physics and radiation dosimetry*. Wiley-VCH, first edition.

Aznar, M. C. (2005). *Real-time in vivo luminescence dosimetry in radiotherapy and mammography using* Al_2O_3*:C*. PhD thesis, Risø National Laboratory, Roskilde, Denmark.

Aznar, M. C., Andersen, C. E., Bøtter-jensen, L., Bäck, S. Å. J., Mattsson, S., Kjær-Kristoffersen, F., and Medin, J. (2004). Real-time optical-fibre luminescence dosimetry for radiotherapy: Physical characteristics and applications in photon beams. *Physics in Medicine and Biology*, 49(9):1655–1669.

Aznar, M. C., Hemdal, B., Medin, J., Marckmann, C. J., Andersen, C. E., Bøtter-Jensen, L., Andersson, I., and Mattsson, S. (2005). In vivo absorbed dose measurements in mammography using a new real-time luminescence technique. *British Journal of Radiology*, 78(928):328–334.

Baldock, C., Deene, Y. D., Doran, S., Ibbott, G., Jirasek, A., Lepage, M., McAuley, K. B., Oldham, M., and Schreiner, L. J. (2010). Polymer gel dosimetry. *Physics in Medicine and Biology*, 55(5):R1–R63.

Beddar, A. S., Briere, T. M., Mourtada, F. A., Vassiliev, O. N., Liu, H. H., and Mohan, R. (2005). Monte Carlo calculations of the absorbed dose and energy dependence of plastic scintillators. *Medical Physics*, 32(5):1265–1269.

Beddar, A. S., Kinsella, T. J., Ikhlef, A., and Sibata, C. H. (2001). A miniature "scintillator-fiberoptic-pmt" detector system for the dosimetry of small fields in stereotactic radiosurgery. *IEEE Transactions on Nuclear Science*, 48(3):924–928.

Beddar, A. S., Mackie, T. R., and Attix, F. H. (1992a). Cerenkov light generated in optical fibres and other light pipes irradiated by electron beams. *Physics in Medicine and Biology*, 37(4):925–935.

Beddar, A. S., Mackie, T. R., and Attix, F. H. (1992b). Water-equivalent plastic scintillation detectors for high-energy beam dosimetry: I. Physical characteristics and theoretical considerations. *Physics in Medicine and Biology*, 37(10):1883–1900.

Beddar, A. S., Mackie, T. R., and Attix, F. H. (1992c). Water-equivalent plastic scintillation detectors for high-energy beam dosimetry: II. Properties and measurements. *Physics in Medicine and Biology*, 37(10):1901–1913.

Beddar, A. S., Suchowerska, N., and Law, S. H. (2004). Plastic scintillation dosimetry for radiation therapy: minimizing capture of Cerenkov radiation noise. *Physics in Medicine and Biology*, 49(5):783–790.

Beierholm, A. R. (2007). Medical dosimetry using fiber-coupled organic scintillators. Master's thesis, University of Copenhagen, Denmark.

Beierholm, A. R., Andersen, C. E., Lindvold, L. R., and Aznar, M. C. (2010). Investigation of linear accelerator pulse delivery using fast organic scintillator measurements. *Radiation Measurements*, 45(3-6):668–670.

Beierholm, A. R., Andersen, C. E., Lindvold, L. R., Kjær-Kristoffersen, F., and Medin, J. (2008). A comparison of BCF-12 organic scintillators and Al_2O_3:C crystals for real-time medical dosimetry. *Radiation Measurements*, 43(2-6):898–903.

Benoit, D., Garcia, P., Matias-Vaillé, S., Ravotti, F., Vaillé, J.-R., Glaser, M., Brichard, B., Fernandez, A. F., Chatry, C., and Dusseau, L. (2008a). Real-time fibered optically stimulated luminescence dosimeter based on SrS:Ce,Sm phosphor. *IEEE Transactions On Nuclear Science*, 55(4):2154–2160.

Benoit, D., Vaillé, J. R., Lautissier, J., Matias-Vaillé, S., Isturiz, J., Garcia, P., Brîchard, B., and Dusseau, L. (2008b). Feasibility of fibered monitoring system for pulsed dose-rate facilities based on radioluminescence of SrS:Ce,Sm phosphor. *IEEE Transactions On Nuclear Science*, 55(6):3421–3427.

BJR (1996). BJR Supplement 25: Central axis depth dose data for use in radiotherapy. *British Institute of Radiology.*

Boon, S. N., van Lujik, P., Schippers, J. M., Meertens, H., Denis, J. M., Vynckier, S., Medin, J., and Grusell, E. (1998). Fast 2D phantom dosimetry for scanning proton beams. *Medical Physics*, 25(4):464–475.

Bucciolini, M., Buonamici, F. B., Mazzocchi, S., Angelis, C. D., Onori, S., and Cirrone, G. A. P. (2003). Diamond detector versus silicon diode and ion chamber in photon beams of different energy and field size. *Medical Physics*, 30(8):2140–2154.

Busjan, W., Wick, K., and Zoufal, T. (1998). Radiation induced absorption due to shortlived absorption centers in plastic scintillators. *Nuclear Physics B - Proceedings Supplements)*, 61(3):504–508.

Butson, M. J., Cheung, T., and Yu, P. K. N. (2005). Weak energy dependence of EBT gafchromic film dose response in the 50 kVp-10 MVp X-ray range. *Applied Radiation and Isotopes*, 64(1):60–62.

Buttar, C. M., Airey, R., Conway, J., Hill, G., Ramkumar, S., Scarsbrook, G., Sussmann, R., Walker, S., and Whitehead, A. (2000). A study of radiotherapy dosimeters based on diamond grown by chemical vapour deposition. *Diamond & Related Materials*, 9(3):965–969.

Cartwright, L. E., Lambert, J., McKenzie, D. R., and Suchowerska, N. (2009). The angular dependence and effective point of measurement of a cylindrical scintillation dosimeter with and without a radio-opaque marker for brachytherapy. *Physics in Medicine and Biology*, 54(7):2217–2227.

Chen, F., Graeff, C. F. O., and Baffa, O. (2005). K-band EPR dosimetry: small-field beam profile determination with miniature alanine dosimeter. *Applied Radiation and Isotopes*, 62(2):267–271.

Cheng, C.-W., Cho, S. H., Taylor, M., and Das, I. J. (2007). Determination of zero-field size percent depth doses and tissue maximum ratios for stereotactic radiosurgery and IMRT dosimetry: comparison between experimental measurements and Monte Carlo simulation. *Medical Physics*, 34(8):3149–3157.

Chow, J. C. L., Seguin, M., and Alexander, A. (2005). Dosimetric effect of collimating jaws for small multileaf collimated fields. *Medical Physics*, 32(3):759–765.

Clift, M. A., Johnston, P. N., and Webb, D. V. (2002). A temporal method of avoiding the Cerenkov radiation generated in organic scintillator dosimeters by pulsed mega-voltage electron and photon beams. *Physics in Medicine and Biology*, 47(8):1421–1433.

Clift, M. A., Sutton, R. A., and Webb, D. V. (2000a). Dealing with Cerenkov radiation generated in organic scintillator dosimeters by bremsstrahlung beams. *Physics in Medicine and Biology*, 45(5):1165–1182.

Clift, M. A., Sutton, R. A., and Webb, D. V. (2000b). Water equivalence of plastic organic scintillators in megavoltage radiotherapy bremsstrahlung beams. *Physics in Medicine and Biology*, 45(7):1885–1895.

Damkjær, S. M. S. and Andersen, C. E. (2010). Memory effects and systematic errors in the rl signal from fiber coupled Al_2O_3:C for medical dosimetry. *Radiation Measurements*, 45(3-6):671–673.

Damkjær, S. M. S., Andersen, C. E., and Aznar, M. C. (2008). Improved real-time dosimetry using the radioluminescence signal from Al_2O_3:C. *Radiation Measurements*, 43(2-6):893–897.

Das, I. J., Ding, G. X., and Ahnesjö, A. (2008). Small fields: nonequilibrium radiation dosimetry. *Medical Physics*, 35(1):206–215.

Dawson, C. J. (2008). Integrator circuitry used to determine the radial profile of a non-neutral plasma. Senior thesis written at the Department of Physics and Astronomy, Brigham Young University.

de Boer, S. F., Beddar, A. S., and Rawlinson, J. A. (1993). Optical filtering and spectral measurements of radiation-induced light in plastic scintillation dosimetry. *Physics in Medicine and Biology*, 38(7):945–958.

Dutreix, A., Bjärngard, B. E., Bridier, A., Mijnheer, B., Shaw, J. E., and Svensson, H. (1997). *Monitor unit calculation for high energy photon beams*. European Society for Therapeutic Radiology and Oncology (ESTRO). Physics for clinical radiotherapy - Booklet No. 3.

Edmund, J. M. and Andersen, C. E. (2007). Temperature dependence of the Al_2O_3:C response in medical luminescence dosimetry. *Radiation Measurements*, 42(2):177–189.

Flühs, D., Heintz, M., Indenkämpen, F., Wieczorek, C., Kolanoski, H., and Quast, U. (1996). Direct reading measurement of absorbed dose with plastic scintillators - The general concept and applications to opthalmic plaque dosimetry. *Medical Physics*, 23(3):427–434.

Fog, L. S., Rasmussen, J. F. B., Aznar, M., Kjær-Kristoffersen, F., Vogelius, I. R., Engelholm, S. A., and Bangsgaard, J. P. (2011). A closer look at RapidArc® radiosurgery plans using very small fields. *Physics in Medicine and Biology*, 56(6):1853–1863.

Fontbonne, J. M., Iltis, G., Ban, G., Battala, A., Vernhes, J. C., Tillier, J., Bellaize, N., Brun, C. L., Tamain, B., Mercier, K., and Motin, J. C. (2002). Scintillating fiber dosimeter for radiation therapy accelerator. *IEEE Transactions On Nuclea Science*, 49(5):2223–2227.

Francescon, P., Cora, S., Cavedon, C., Scalchi, P., Reccanello, S., and Colombo, F. (1998). Use of a new type of radiochromic film, a new parallel-plate micro-chamber, MOSFETs, and TLD 800 microcubes in the dosimetry of small beams. *Medical Physics*, 25(4):503–511.

Frelin, A.-M., Fontbonne, J.-M., Ban, G., Colin, J., and Labalme, M. (2008a). Comparative study of plastic scintillators for dosimetric applications. *IEEE Transactions On Nuclear Science*, 55(5):2749–2756.

Frelin, A.-M., Fontbonne, J.-M., Ban, G., Colin, J., Labalme, M., Batalla, A., Vela, A., Boher, P., Braud, M., and Leroux, T. (2008b). The dosimap, a new 2d scintillating dosimeter for imrt quality assurance: Characterization of two Cerenkov discrimination methods. *Medical Physics*, 35(5):1651–1662.

Frelin, A.-M., Fontbonne, J.-M., Ban, G., Labalme, M., Batalla, A., Isambert, A., Vela, A., and Leroux, T. (2005). Spectral discrimination of Cerenkov radiation in scintillating dosimeters. *Medical Physics*, 32(9):3000–3006.

Gaza, R. and McKeever, S. W. S. (2006). A real-time, high-resolution optical fibre dosemeter based on optically stimulated luminescence (OSL) of KBr:Eu, for potential use during the radiotherapy of cancer. *Radiation Protection Dosimetry*, 120(1-4):14–19.

Guillot, M., Gingras, L., Archambault, L., Beddar, S., and Beaulieu, L. (2011). Spectral method for the correction of the Cerenkov light effect in plastic scintillation detectors: A comparison study of calibration procedures and validation in Cerenkov light-dominated situations. *Medical Physics*, 38(4):2140–2150.

Gustafsson, H., Lund, E., and Olsson, S. (2008). Lithium formate EPR dosimetry for verifications of planned dose distributions prior to intensity-modulated radiation therapy. *Physics in Medicine and Biology*, 53(17):4667–4682.

Gustafsson, H., Vial, P., Kuncic, Z., Baldock, C., and Greer, P. B. (2009). Epid dosimetry: Effect of different layers of materials on absorbed dose response. *Medical Physics*, 36(12):5665–5674.

Hartmann, B., Martisiková, M., and Jäkel, O. (2010). Technical note: Homogeneity of Gafchromic® EBT2 film. *Medical Physics*, 37(4):1753–1756.

Helt-Hansen, J. and Miller, A. (2004). Risøscan - a new dosimetry software. *Radiation Physics and Chemistry*, 71(1-2):361–364.

Heydarian, M., Hoban, P. W., and Beddoe, A. H. (1996). A comparison of dosimetry techniques in stereotactic radiosurgery. *Physics in Medicine and Biology*, 41(1):93–110.

IAEA (2000). IAEA Technical Report Series No. 398: Absorbed dose determination in external beam radiotherapy: An international code of practice for dosimetry based on standards of absorbed dose to water. *International Atomic Energy Agency.*

IAEA (2003). *Standards and codes of practice in medical radiation dosimetry: Proceedings Series volume 2*. International Atomic Energy Agency.

IAEA (2005). *Radiation oncology physics: A handbook for teachers and students*. International Atomic Energy Agency.

ICRP (2000). ICRP Publication 86: Prevention of accidental exposures to patients undergoing radiation therapy. *Annuals of the ICRP*, 30(3).

ICRU (1976). ICRU Report 24: Determination of absorbed dose in a patient irradiated by beams of x or gamma rays in radiotherapy. *International Commission on Radiation Units and Measurements.*

ICRU (1984). ICRU Report 37: Radiation dosimetry: electron beams with energies between 1 and 50 MeV. *International Commission on Radiation Units and Measurements.*

ICRU (1999). ICRU Report 62: Prescribing, recording and reporting photon beam therapy (supplement to Report 50). *International Commission on Radiation Units and Measurements.*

IEC (1998). Particular requirements for the safety of medical electron accelerators in the range 1 MeV to 50 MeV, IEC 60601-2-1. *International Electrotechnical Commission.*

Illemann, J. (2009). Single-pulse-resolved dosimetry with miniaturized detectors in teletherapy. *IFMBE Proceedings*, 25(1):932–935.

IPEM (2010). *IPEM Report 103: Small field MV photon dosimetry.* Institute of Physics and Engineering in Medicine.

Izewska, J., Bera, P., and Vatnitsky, S. (2002). IAEA/WHO TLD postal dose audit service and high precision measurements for radiotherapy level dosimetry. *Radiation Protection Dosimetry*, 101(1-4):387–392.

Jelly, J. V. (1958). *Cerenkov radiation and its applications*. Pergamon Press, first edition.

Johns, H. E. and Cunningham, J. R. (1983). *The physics of radiology*. Thomas Books, fourth edition.

Jornet, N., Ribas, M., and Eudaldo, T. (2000). In vivo dosimetry: Intercomparison between p-type based and n-type based diodes for the 16-25 MV energy range. *Medical Physics*, 27(6):1287–1293.

Justus, B. L., Falkenstein, P., Huston, A. L., Plazas, M. C., Ning, H., and Miller, R. W. (2004). Gated fiber-optic-coupled detector for *in vivo* real-time radiation dosimetry. *Applied Optics*, 43(8):1663–1668.

Khan, F. M. (2003). *The physics of radiation therapy*. Lippincott Williams & Wilkins, third edition.

Klein, D. M. and McKeever, S. W. S. (2008). Optically stimulated luminescence from KBr:Eu as a near-real-time dosimetry system. *Radiation Measurements*, 43(2-6):883–887.

Klein, D. M., Tailor, R. C., Archambault, L., Wang, L., Therriault-Proulx, F., and Beddar, A. S. (2010). Measuring output factors of small fields formed by collimator jaws and multileaf collimator using plastic scintillation detectors. *Medical Physics*, 37(10):5541–5549.

Konnoff, D. C., Plant, T. K., and Shiner, E. (2011). SSPM based radiation sensing: preliminary laboratory and clinical results. *Radiation Measurements*, 46(1):76–87.

Kroutilíková, D. and Zácková, H. (1999). Tld audit in radiotherapy in the czech republic. *Radiation Protection Dosimetry*, 85(1-4):393–396.

Lacroix, F., Archambault, L., Gingras, L., Guillot, M., Beddar, A. S., and Beaulieu, L. (2008). Clinical prototype of a plastic water-equivalent scintillating fiber dosimeter array for qa applications. *Medical Physics*, 35(8):3682–3690.

Lacroix, F., Beaulieu, L., Archambault, L., and Beddar, A. S. (2010a). Simulation of the precision limits of plastic scintillation detectors using optimal component selection. *Medical Physics*, 37(2):412–418.

Lacroix, F., Guillot, M., McEwen, M., Cojocaru, C., Gingras, L., Beddar, A., and Beaulieu, L. (2010b). Extraction of depth-dependent perturbation factors for parallel-plate chambers in electron beams using a plastic scintillation detector. *Medical Physics*, 37:4331–4342.

Lam, K. L., Muthuswamy, M. S., and Haken, R. K. T. (1998). Measurement of backscatter to themonitor chamber of medical accelerators using target charge. *Medical Physics*, 25(3):334–338.

Lambert, J., McKenzie, D. R., Law, S., Elsey, J., and Suchowerska, N. (2006). A plastic scintillation dosimeter for high dose rate brachytherapy. *Physics in Medicine and Biology*, 51(21):5505–5516.

Lambert, J., Nakano, T., Law, S., Elsey, J., McKenzie, D. R., and Suchowerska, N. (2007). In vivo dosimeters for HDR brachytherapy: A comparison of a diamond detector, MOSFET, TLD, and scintillation detector. *Medical Physics*, 34(5):1759–1765.

Lambert, J., Yin, Y., McKenzie, D. R., Law, S., and Suchowerska, N. (2008). Cerenkov-free scintillation dosimetry in external beam radiotherapy with an air core light guide. *Physics in Medicine and Biology*, 53(11):3071–3080.

Lambert, J., Yin, Y., McKenzie, D. R., Law, S., and Suchowerska, N. (2009). Cerenkov light spectrum in an optical fiber exposed to a photon or electron radiation therapy beam. *Applied Optics*, 48(18):3362–3367.

Lambert, J., Yin, Y., McKenzie, D. R., Law, S. H., Ralston, A., and Suchowerska, N. (2010). A prototype scintillation dosimeter customized for small and dynamic megavoltage radiation fields. *Physics in Medicine and Biology*, 55(4):1115–1126.

Laub, W. U. and Wong, T. (2003). The volume effect of detectors in the dosimetry of small fields used in IMRT. *Medical Physics*, 30(3):341–347.

Lee, K. Y., Fung, K. K. L., and Kwok, C. S. (2006). Application of high-resolution radiochromic film dosimetry in verifying a small-field stereotactic radiosurgery plan. *Applied Radiation and Isotopes*, 64(8):934–939.

Li, X. A., Soubra, M., Szanto, J., and Gerig, L. H. (1995). Lateral electronic equilibrium and electron contamination in measurements of head-scatter factors using miniphantoms and brass caps. *Medical Physics*, 22(7):1167–1170.

Lindsay, P., Rink, A., Ruschin, M., and Jaffray, D. (2010). Investigation of energy dependence of EBT and EBT-2 gafchromic film. *Medical Physics*, 37(2):571–576.

Lindvold, L. R., Andersen, C. E., and Beierholm, A. R. (2010). An organic dye in a polymer matrix - a search for a scintillator with long luminescent lifetime. *Radiation Measurements*, 45(3-6):615–617.

Létourneau, D., Pouliot, J., and Roy, R. (1999). Miniature scintillating detector for small field radiation therapy. *Medical Physics*, 26(12):2555–2561.

Marckmann, C. J., Aznar, M. C., Andersen, C. E., and Bøtter-Jensen, L. (2006). Influence of the stem effect on radioluminescence signals from optical fibre Al_2O_3:C dosimeters. *Radiation Protection Dosimetry*, 119(1-4):363–367.

Mayles, P., Nahum, A., and Rosenwald, J. C. (2007). *Handbook of radiotherapy physics - theory and practice*. Taylor & Francis, first edition.

McDermott, L. N., Nijsten, S. M. J. J. G., Sonke, J.-J., Partridge, M., van Herk, M., and Mijnheer, B. J. (2006). Comparison of ghosting effects for three commercial a-Si EPIDs. *Medical Physics*, 33(7):2448–2451.

McLaughlin, W. L., Soares, C. G., Sayeg, J. A., McCullough, E. C., Kline, R. W., Wu, A., and Maitz, A. H. (1994). The use of a radiochromic detector for the determination of stereotactic radiosurgery dose characteristics. *Medical Physics*, 21(3):379–388.

Mountford, J., Porrovecchio, G., Smid, M., and Smid, R. (2008). Development of a switched integrator amplifier for high-accuracy optical measurements. *Applied Optics*, 47(31):5821–5828.

New York Times (2010a). A lifesaving tool turned deadly - radiation offers powerful new cures, and ways to do harm. *The New York Times*. January 24.

New York Times (2010b). A pinpoint beam strays invisibly, harming instead of healing. *The New York Times*. December 29.

Nowotny, R. (2004). LiF:W as a scintillator for dosimetry in diagnostic radiology. *Physics in Medicine and Biology*, 49(12):2599–2611.

Nowotny, R. (2007). Radioluminescence of some optical fibres. *Physics in Medicine and Biology*, 52:N67–N73.

Otto, K. (2008). Volumetric modulated arc therapy: IMRT in a single gantry arc. *Medical Physics*, 35(1):310–317.

Ottosson, R. O., Karlsson, A., and Behrens, C. F. (2010). Pareto front analysis of 6 and 15 MV dynamic IMRT for lung cancer using pencil beam, AAA and Monte Carlo. *Physics in Medicine and Biology*, 55(16):4521–4533.

Petric, M. P., Robar, J. L., and Clark, B. G. (2006). Development and characterisation of a tissue equivalent plastic scintillator based dosimetry system. *Medical Physics*, 33(1):96–105.

Podgorsak, E. B. (2010). *Radiation physics for medical physicists*. Springer, second edition.

Ramasehan, R., Kohli, K., Zhang, T., Lam, T., Norlinger, B., Hallil, A., and Islam, M. (2004). Performance characteristics of a microMOSFET as an in vivo dosimeter in radiation therapy. *Physics in Medicine and Biology*, 49(17):4031–4048.

Rogers, D. W. O., Faddegon, B. A., Ding, G. X., Ma, C.-M., J, J. W., and Mackie, T. R. (1995). BEAM: a Monte Carlo code to simulate radiotherapy treatment units. *Medical Physics*, 22(5):504–524.

Rogers, D. W. O., Walters, B., and Kawrakow, I. (2009). *BEAMnrc users manual*. National Research Council Canada. NRCC Report PIRS-0509(A)revK.

Russell, P. S. (2006). Photonic-crystal fibers. *Journal of Lightwave Technology*, 24(12):4729–4749.

Sadagopan, R., Bencomo, J. A., Martin, R. L., Nilsson, G., Matzen, T., and Balter, P. A. (2009). Characterization and clinical evaluation of a novel IMRT quality assurance system. *Journal of Applied Clinical Medical Physics*, 10(2):104–119.

Saint-Gobain (2005). *Scintillation products - plastic scintillating fibers brochure*. Saint-Gobain Ceramics & Plastics, Inc.

Sauer, O. A. and Wilbert, J. (2007). Measurement of output factors for small photon beams. *Medical Physics*, 34(6):1983–1988.

Scott, A. J. D., Nahum, A. E., and Fenwick, J. D. (2008). Using a Monte Carlo model to predict dosimetric properties of small radiotherapy photon fields. *Medical Physics*, 35(10):4671–4684.

Seuntjens, J., Olivares, M., Evans, M., and Podgorsak, E. (2005). Absorbed dose to water reference dosimetry using solid phantoms in the context of absorbed-dose protocols. *Medical Physics*, 32(9):2945–2953.

Sjöström, D., Bjelkengren, U., Ottosson, W., and Behrens, C. (2009). A beam-matching concept for medical linear accelerators. *Acta Oncologica*, 48(2):192–200.

Tanyi, J. A., Krafft, S. P., Ushino, T., Huston, A. L., and Justus, B. L. (2010). Performance characteristics of a gated fiber-optic-coupled dosimeter in high-energy pulsed photon radiation dosimetry. *Applied Radiation and Isotopes*, 68:364–369.

van Elmpt, W., McDermott, L., Nijstena, S., Wendling, M., Lambina, P., and Mijnheer, B. (2008). A literature review of electronic portal imaging for radiotherapy dosimetry. *Radiotherapy and Oncology*, 88(3):289–309.

Vassiliev, N. O., Titt, U., Pönisch, F., Kry, S. F., Mohan, R., and Gillin, M. T. (2006). Dosimetric properties of photon beams from a flattening filter free clinical accelerator. *Physics in Medicine and Biology*, 51(7):1907–1917.

Vestad, T. A., Malinen, E., Olsen, D. R., Hole, E. O., and Sagstuen, E. (2004). Electron paramagnetic resonance (EPR) dosimetry using lithium formate in radiotherapy: comparison with thermoluminescence (TL) dosimetry using lithium fluoride rods. *Physics in Medicine and Biology*, 49(20):4701–4715.

Walters, B., Kawrakow, I., and Rogers, D. W. O. (2009). *DOSXYZnrc users manual*. National Research Council Canada. NRCC Report PIRS-794revB.

Wick, K. and Zoufal, T. (2001). Unexpected behavior of polystyrene-based scintillating fibers during irradiation at low doses and low dose rates. *Nuclear Instruments and Methods in Physics Research B*, 185(1-4):341–345.

Williamson, J. F., Dempsey, J. F., Kirov, A. S., Monroe, J. I., Binns, W. R., and Hedtjärn, H. (1999). Plastic scintillator response to low-energy photons. *Physics in Medicine and Biology*, 44(4):857–871.

Yukihara, E. G. and McKeever, S. W. S. (2008). Optically stimulated luminescence (OSL) dosimetry in medicine. *Physics in Medicine and Biology*, 53:R351–R379.

Risø DTU is the National Laboratory for Sustainable Energy. Our research focuses on development of energy technologies and systems with minimal effect on climate, and contributes to innovation, education and policy. Risø has large experimental facilities and interdisciplinary research environments, and includes the national centre for nuclear technologies.

Risø DTU
National Laboratory for Sustainable Energy
Technical University of Denmark

Frederiksborgvej 399
PO Box 49
DK-4000 Roskilde
Denmark
Phone +45 4677 4677
Fax +45 4677 5688

www.risoe.dtu.dk